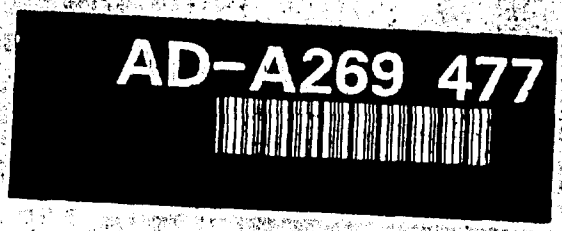

Prepared with partial support of the Department of the Air Force under Contract F19628-90-C-0002.

The ESC Public Affairs Office has reviewed this report, and it is releasable to the National Technical Information Service, where it will be available to the general public, including foreign nationals.

This technical report has been reviewed and is approved for publication.

FOR THE COMMANDER

Gary Tatungian
Administrative Contracting Officer
Directorate of Contracted Support Management

MASSACHUSETTS INSTITUTE OF TECHNOLOGY
LINCOLN LABORATORY

PROCEEDINGS OF THE 1993 SPACE SURVEILLANCE WORKSHOP

PROJECT REPORT STK-206
VOLUME II

30 MARCH–1 APRIL 1993

The eleventh Annual Space Surveillance Workshop held on 30–31 March and 1 April 1993 was hosted by MIT Lincoln Laboratory and provided a forum for space surveillance issues. Volume II documents most of the remaining presentations, with minor changes where necessary.

LEXINGTON MASSACHUSETTS

PREFACE

The eleventh Annual Space Surveillance Workshop sponsored by MIT Lincoln Laboratory was held 30-31 March and 1 April 1993. The purpose of this series of workshops is to provide a forum for the presentation and discussion of space surveillance issues.

This *Proceedings, Volume II,* documents most of the remaining presentations from this workshop. The papers contained were reproduced directly from copies supplied by their authors (with minor mechanical changes where necessary).

Dr. R. Sridharan
1992 Workshop Chairman

Dr. R. W. Miller
Co-chair

TABLE OF CONTENTS

Calibration and Characterization of the SBV Sensor

T. P. Opar (Lincoln Laboratory, Massachusetts Institute of Technology)

This paper discusses some of the techniques and results of the calibration of the Space-Based Visible (SBV) sensor on the Midcourse Space Experiment (MSX) satellite. The sensor consists of a set of four 420 by 420 pixel imagers in a f/3 off-axis reimaging telescope with a 6.6° by 1.4° field of view [1]. The sensor has been designed to perform a wide variety of space surveillance missions, including; precise metric and radiometric measurements of resident space objects, the demonstration of a high degree of Out - of - Field of View Radiance Rejection (OFVR) , and measurements of background radiance levels from sources relevant to space surveillance missions. This broad range of applications impose stringent requirements on the sensor calibration and characterization.

Optimal utility of this sensor requires that it be calibrated and characterized in three specific areas: extended and point source radiometry, spatial structure characterization, and optical distortion. In addition, the calibration must be performed on the flight system in an environment similar to that expected on orbit. The ground based test sequences included cover closed dark frames, extended source measurements with an integrating sphere, and point source measurements with a off-axis parabola collimating system. Over 2000 individual measurements were performed in support of the sensor characterization and calibration.

The calibration and characterization effort is guided by the requirements imposed by the specific measurements and technology demonstrations planned for the sensor. The measurement requirements are the primary drivers on the nature and the quality of the calibration tests. The SBV requirements fall into three categories: Radiometry, Optical Distortion, and Sensor Characterization. The radiometric calibration of the sensor provides the means to convert detected point source and extended source images from sensor counts to precise engineering units. The optical distortion calibration is used to transfer point source images from focal plane or image space out to physical (or object) space. Finally, the sensor characterization requires that a detailed knowledge of all aspects which affect the radiometric and goniometric performance of the sensor are known. Some of the SBV characterization measurements include creation of multiplicative and subtractive flat field maps for data processing, long term monitoring of the OFVR performance of the sensor, determining the noise level of the sensor, and mapping the optical Point Spread Function (PSF) across the focal plane.

Three periods were available for testing the SBV sensor. The first testing opportunity arose during the Telescope Acceptance Tests. During this period, the focus of the SBV telescope was firmly established, the initial OFVR testing took place, and the effects of environmental stresses on the optics were assessed. The flight optics and focal were employed with a brassboard version of the camera. These tests occurred at both room temperature and in a Thermal/Vacuum tank at flightlike conditions. A total of 341 measurements were made during this period. The second testing opportunity was a sixteen week campaign during which the bulk of the calibration was performed. The flight optics, focal plane, and flight electronics were tested as an integrated unit. This unit is called the Instrument Side Assembly (ISA.) The entire suite of SBV calibration and characterization measurements was performed. A total of 1645 tests were performed. These tests were performed both in at room temperature and the Thermal/Vacuum tank at anticipated flight temperatures. The final test sequences occurred after the flight Electronics Side Assembly (ESA) was integrated with the ISA. The primary purpose of this series of tests was to verify that the calibration did not change as a results of the integration.

The total suite of test sequences included five measurement types with numerous subtasks . Table 1 is a summary of the test performed during the entire measurement campaign.

Table 1
Number of SBV Calibration and Charactertization Measurments Performed

Test Type	Test Mode	Acceptance Phase	ISA Phase	ESA Phase
Focus Tests		394	107	---
Cover Closed	Noise Survey	41	288	38
	Flat Field Map	61	80	8
OFVR	in situ Lamp	26	28	8
	external	5	3	---
Extended Source	Flat Field	24	60	8
	Radiometric Calibration	73	348	10
Point Source	Radiometric Calibration		558	---
	Optical Distortion Mapping	49	28	---
	PSF Mapping	67	178	---
	Non Linearity	--	26	---

Due to the total number of tests and the amount of data collected this paper will not provide detailed information on the entire set of the tests. A discussion of the results from the focus, cover closed, OFVR, Extended Source, and Optical Distortion mapping follow.

Focus:

The initial purpose of the focus tests was to establish the best focus of the telescope. Subsequent test verified that the focus did not change as a result of environmental tests. The fundamental focusing procedure is to utilize the computer controlled collimator system with an Laser Unequal Path Interferometer (LUPI) to illuminate the focal plane with a point source image with a $\lambda/10$ wavefront accuracy beam. Figure 1 is one view of the SBV collimator system. Visible in the picture is the twelve inch, f/4, $\lambda/16$ surface Off-Axis Parabola (OAP), with the LUPI in the foreground. Figure 2 is another view with the SBV telescope clearly visible and the $\lambda/20$ surface twelve inch flat mirror placed in front of the SBV aperture. Realtime calculations of the straddle factor using a piece of Ground Support Equipment was performed. (Straddle factor is the fraction of the total point source signal in the pixel in which the PSF is centered. If the PSF is located at the center of the pixel, then straddle factor can be identified with the ensquared energy.) Focus is achieved by maximizing the Ensquared Energy across the focal plane with the realtime algorithm. Table 2 lists the Ensquared Energy across the four CCDs. The peak Ensquared Energy is located at the center of CCD #3 which is the near the optical boresight of the sensor.

Table 2
Measured Ensquared Energy and Straddle Factor at the Center of the SBV CCD

CCD #	Ensquared Energy (%)	Straddle Factor (%)
1	50	38
2	67	50
3	69	51
4	66	49

It is important to note that the focus procedure utilizing the LUPI as the focus source is critical to establishing the focus. The LUPI allows the OAP and the flat to be aligned interferometrically without using the SBV telescope. The Collimator system was aligned to better than one quarter wave of error. This insures that a collimated beam in incident on the detector and that a true focus measurement is made.

Cover Closed Measurements:

The Cover Closed Measurements supported three of the characterization requirements. First, they provided data to establish the noise level of the system in the absence of optical input. Second, the dark current level of the system is measured wing cover closed imagery Third, they are the source of data from which the subtractive flat field maps used in the data processing are generated.

The noise of the system is determined by spatially averaging the temporal variance of the cover closed signal with the dark current noise removed. The dark current level of the system is determined by performing a linear fit to spatial average signals across the focal plane as a function of exposure time. The slope of the curve of average signal level versus exposure time is the dark current in dark current counts per second. The system transfer function (gain, the number of photo-electrons / count) is used to convert to photo-electrons / pixel per second. Table 3 lists the noise and dark current values for the SBV sensor at two focal temperatures.

Table 3
Noise Performance of the SBV Focal Plane as a Function of Temperature

Focal Plane Temperature (°K)	rms Noise (electrons)	Dark Current (electrons / pixel / s)
-47.1	4.7	5.0
-42.6	5.3	8.4

OFVR Measurements:

The demonstration of the high degree of Out - of - Field - of - View Radiance (OFVR) rejection of the SBV telescope is one of primary surveillance experiments of the sensor. To monitor the OFVR performance of the sensor during the ground calibration frequent direct and indirect measurements of the OVFR performance were taken. There are two manners in which these tests are performed, the first is a direct measure of the mirror cleanliness and the second is an indirect measure which utilizes an internal lamp.

A figure of merit for mirror surface cleanliness, which directly affect the OFVR performance, is the Bidirectional Reflectance Distribution Function (BRDF). [2] A portable BRDF measuring system s used throughout the past 14 months to periodically measure the BRDF of the primary SBV mirror. The BRDF can be characterized by a power law which can be expressed as:

$$BRDF = \frac{BRDF\ @\ 1^\circ}{\theta^n} \qquad 1.$$

where

BRDF = BRDF per sr of the mirror
BRDF @ 1° = BRDF per sr at one degree off-axis

θ = off - axis angle
n = rolloff exponent

The design goal is that the SBV sensor be delivered with a BRDF @ 1° = 3.0 10^{-3} / sr with a rolloff of 2. OFVR performance improves with a smaller value of the BRDF @ 1 ° and larger rolloff. Table 4 is a summary of the OFVR history. The first column lists the date of the measurement. The second and third columns list the BRDF @ 1° and the rolloff derived from the external measurements. The apparent change of the BRDF parameters on 6/5/92 is due to the fact that the telescope was moved to the thermal vacuum chamber at this time and that a different portion of the mirror surface was sampled. The effect of the BRDF in terms of surveillance is determined by integrating the effect over the illuminated portion of the earth. A measure of the effect of the BRDF is obtained by calculating the Non-Rejected Earth Radiance (NRER.) NRER is obtained by integrating the BRDF over the illuminated portion of the earth including additional effects of diffraction at the aperture, diffraction suppression, and mirror baffling. The fourth column in Table 2 is the NRER (in magnitudes/arcsec^2) derived from the BRDF data above a fully illuminated earth at 100 tangent altitude. The derived NRER is seen to vary from a minimum brightness of 15.4 magnitudes to a maximum of 15.05. A 0.4 magnitude increase in background at 100 km. is evident which results is a 0.2 magnitude loss in sensitivity The equivalent data at the 350 km. tangent altitude shows little loss of performance. The NRER for 350 km. tangent altitude remains effectively constant at 17.3 vm / ascsec^2 . This is due to the high value of the rolloff parameter.

Table 4
OFVR Performance From External BRDF Measurements

Date	BRDF @ 1° (/ sr)	Rolloff	Derived NRER 100 km (mag / arcsec^2)
11/17/91	2.1e-03	2.5	15.5
11/21/91	2.1e-03	2.5	15.5
11/22/91	3.2e-03	2.7	15.4
12/06/91	1.5e-03	2.3	15.5
01/29/92	1.3e-02	3.4	15.2
03/02/92	2.0e-03	2.4	15.4
03/23/92	3.4e-03	2.7	15.4
04/03/92	1.1e-03	2.2	15.5
05/29/92	1.5e-03	3.4	15.1
08/12/92	5.4e-03	2.9	15.3
09/21/92	2.0e-02	3.6	15.1
11/25/92	2.8e-02	3.7	15.1

The indirect measurement utilizes an in situ BRDF lamp monitor which provides a collimated off-axis source which illuminated the primary mirror. The scattered radiation from this lamp is collected at the focal plane. Due to non-specular scatter of the mirrors there is a gradient of the signal across CCD #3. The slope of this gradient is a measure of the cleanliness of the mirrors. The slope of the signal varied by about 38% over the calibration period which corresponds to 0.35 magnitudes. (Note, due to the pristine quality of the SBV mirrors, the in situ BRDF monitor signal is detectable only when the focal plane is cooled, therefore no useful in situ data is available from the non-calibration periods.)

The external and in situ BRDF measurements indicate that the cleanliness of the sensor has been

maintained over a period exceeding ten months during which extensive testing and handling has occurred. The BRDF of the sensor at the present time is best characterized by a BRDF @ 1° equal to 2.3e-02 with a rolloff of 3.7. This corresponds to a worst case NRER at 100 km. tangent altitude of 15.05 visual magnitudes.

Extended Source Measurements:

The Extended Source measurements provided a valuable tool to assess a number of features of the SBV sensor. The measurements provided the data to create the multiplicative flat field maps for the sensor, provide a means to establish the radiometric calibration of the across the entire focal plane, to verify that the sensor performance did not vary as a result of environmental testing, and to optically measure the system transfer function (gain) of the system. In addition, these measurements provided a measure of the long term repeatability of the system.

Extended Source Measurements are performed using a Large Integrating Sphere. An Integrating Sphere provides a spatially uniform, radiometrically calibrated source incident at the sensor aperture. Figure 3 is a view of the Large Integrating Sphere placed directly at the SBV aperture.

Images of all four CCDs have been collected with the sphere as a source. The spectral distribution of the sphere radiance is chosen to match the spectral content of the sun in the 0.4 to 1.0 micron region. Figure 4 is a composite false color image of the entire SBV field of view with a the sphere input. Three aspects of the are clearly evident. The first is the "rainbow-like" appearance of the image. Since SBV is an off-axis design both the apparent aperture diameter and the f number of the telescope varies with focal plane location. The aperture area is maximum near the boundary of CCD #2 and CCD #3 and varies essentially radially from the on-axis point which is out of the field of view. Secondly, the f number varies in the vertical direction so that pixels at the bottom of the image have larger angular extent then the pixels at the top, hence they collect more background radiation and appear brighter. The third feature is the vertical stripping across the focal plane. It is due to an effect of the mask used to create these imagers. The pixels which appear to have collected less signal are physically smaller than their neighbors, thus collect less signal.

This large scale structure can be quantified more precisely. The non-uniformity across the set of four images is roughly 12%. The non-uniformity across each of the individual images is roughly 6%. After the large scale structure has been removed via a low order polynomial fit to the data, a residual pixel - to - pixel non-uniformity of roughly 2% remains. This 2% nonuniformity is due to the quantum efficiency variations in the focal plane. The information contained in the images of Figure 4 is used to generate the SBV multiplicative fixed pattern map.

The Extended Source Measurements are also used to establish the extended source radiometric calibration of the sensor. Since a spectrally calibrated input can be injected onto each pixel and its output measured, a radiometric calibration can performed. The calibration constant derived in this manner ha units of counts per Watt cm^2 sr. The precision of the measurements is estimated to be better than 0.5% .

The repeatability of the measurement is addressed Table 5. The Extended Source Calibration Parameter is presented for five different conditions. Three correspond to measurements taken with the brassboard camera during the Acceptance Tests. The calibration constants agree to about 1%. The last two measurements correspond to the measurements with the Flight Camera under identical conditions. Results from the two redundant camera halves are presented. The total one sigma variation of these calibration constants is 2.4%. This implies that not only the measurement be reliably repeated, but different version of the SBV camera provide highly repeatable performance.

Table 5

Extended Source Calibration Parameter
Long Term Repeatability

Test Condition	Average Calibration Parameter (dn / W cm^2 sr)
Pre Shake †	2.91 E 10
Post Shake †	2.831 E 10
Post Thermal †	2.835 E 10
ISA @ 22°C (A*)	3.017 E 10
ISA @ 22°C (B*)	2.917 E 10
Repeatability (%)	2.4

† Brassboard Camera * Flight Camera Half

Optical Distortion:

Many of the SBV experiments provide accurate metric information on detected targets. In order to achieve a high degree of accuracy the optical distortion of the SBV telescope must be mapped. The requirement imposed on SBV by the surveillance community is that the optical distortion of the telescope be mapped to better than 0.2 pixels. The use of the high precision, computer controlled, scan mirror in concert with the SBV Collimator provides the necessary tools to perform this accurate mapping.

The distortion map is generated by creating a 16 X 16 grid of point source inputs on the focal plane. The position of the input beam is recorded, the point source image is processed to extract the location of the image centroid. Four point source images were collected at each mirror position. A single distortion map data collection event consists of 1024 individual frames of data. The centroid position is fit by a low order polynomial to the location of input beam. The analytical expression for the distortion map is:

$$xc = \sum_{k,l=0}^{3} a_{kl}\, \theta^k \phi^l \qquad 2.a$$

$$yc = \sum_{k,l=0}^{3} b_{kl}\, \theta^k \phi^l \qquad 2.b$$

where

xc = extracted point source centroid in column direction
yc = extracted point source centroid in row direction
θ = angular position of the input beam in elevation
ϕ = angular position of the input beam in azimuth

The residual of the fit is computed. Table 6 is summary of the data taken during the Telescope Acceptance Tests. The telescope was in thermal equilibrium during these tests in the Thermal / Vacuum Chamber.

The first column of the table lists the rms error in pixels in the row and column directions for each

CCD with the telescope at room temperature. The second column provides the same information with the telescope at -65 °C. In each case the rssed pixel error is better than the 0.2 pixel requirement. The last column is a measure of the temperature effects on the optical distortion mapability. This column lists the pixel error when the room temperature map is applied to the -65°C data. The map error does in fact increase, but does not grossly exceed the requirement. This indicates that the temperature effects of the optics may not seriously affect the metric performance of the sensor. (Note, time constraints did not allow for the comparison on CCD #4 to be performed.)

Table 6
Optical Distortion Mappability
rms Map Error

CCD	22°C Test	-65 °C Test	22 °C- - 65 °C Comparison
1	0.050 / 0.074	0.054 / 0.074	0.127 / 0.095
2	0.071 / 0.073	0.070 / 0.073	0.144 / 0.083
3	0.063 / 0.064	0.118 / 0.100	0.317 / 0.140
4	0.120 / 0.080	0.179 / 0.084	-----

Summary:

SBV remained in focus throughout the entire measurement range. The cover closed measurements indicate that the sensor operates at low noise with a very low dark current. The BRDF of the sensor did not vary appreciably during the past year. The changes in BRDF imply a small loss of performance at low tangent altitudes (≈ 100 km.) , but no loss of performance moderate tangent altitudes (≥ 350 km.) Extended source measurements provide the means to generate the multiplicative flat field maps for present and future data processing. The precision and repeatability of the extended source calibration are 1% and 2% respectively. The optical distortion mappability requirement of 0.2 pixels across the focal plane has been demonstrated.

This paper does not present the totality of the information gained on the SBV sensor during the testing period. Over 2000 individual measurement sequences were performed with over 5 GBytes of data collected and archived. About 65% of the testing data was processed in parallel to the data collection. Processing this data is continuing.

References:

1. Harrison, D.C. MIT Lincoln Laboratory, Private Communication

2. Dowling, J. M., "Estimating the Non-Rejected Earth Radiance, NRER< Backgrounds for Infrared Sources," in Proceeedings of the Tri-Services Infrared Backgrounds Symposium, Eds. R. E. Conley and T. D. Murphy, 16 MArch 1984, AFGL-TR-84-0094 S. R. No. 238

Cylindrical Satellite Specular Season Photometry

W.I. Beavers (MIT Lincoln Lab.), R. Angione, V Alten, K. Yanow, and M. Lane (San Diego St. U.)

Introduction

The 61cm reflecting telescope of the San Diego State University Mount Laguna Observatory has been employed to monitor the seasonal brightness variations of several satellites. Primary among these are two Hughes cylinder type satellites 20872, and 20873. Filter photometric measurements during the Fall 1992 "specular season" provide high quality monitoring of the brightness, constancy, and color of these two objects as they went into and out of their specular configuration. These measurements are employed here to determine a "specular function" for use in the photometric modelling of these objects, and for algorithmic prediction of cylindrical satellite brightnesses. These functions should be especially useful for predictive applications for the extended[1] multiple "specular seasons" for the cylindrical satellites when viewed by space-based sensors.

Measurements

The photometric measurements were obtained using a standard astronomical U(ultraviolet), B(blue), V(visual or green) filter photometer and blue sensitive photomultiplier tube with each observation consisting of several ten second integrations on the satellite for each filter, followed by similar sky measurements. A nightly set of star observations was used to determine the atmospheric extinction and instrument magnitude zero point for each of the three filters. Typical measurement errors are a few hundredths of a magnitude in the V band, with comparable errors in B, and slightly larger errors in U.

The primary objects of this study are two Hughes cylindrical satellites 20872(SBS6) and 20873(Galaxy VI), which were launched together on October 12, 1990. Both are now in GEO orbits placing them in such angular proximity to each other that the telescope operators at times have had considerable difficulty in ascertaining which one is being observed at any instant. (On the other hand, the photometry clearly reveals which is which.) These objects were selected for this intensive study to be representative of the several dozen other similarly constructed satellites which are in GEO orbits. Physically, they each consist of a main body of cylindrical shape, which is nearly covered by solar cells, and topped by an antenna. Table 1 compares the physical dimensions of these two Hughes satellite types. Both cylinders are maintained with their rotation axes nearly parallel to the earth's axis. (See Fig.1). Thus, their "specular season" for the Mount Laguna site latitude was centered on day 280 of 1992. The San Diego State observers were successful in obtaining high quality multi-color photometry for both objects on days 277, 279, 280, and 281. A very complete "pre-specular" phase curve for 20873 on day 240 is used as a baseline for comparison.

Fig. 2 contains plots of the measured counts (10s integration) for both satellites for the days near the specular event. For comparison, the maximum measured counts away from the specular geometry such as on day 240 for satellite 20873 were: U = 670 , B = 1800 V = 5000. Thus, the specular brightening is more than a factor of 100 (= 5 magnitudes!) from the maxima for each filter outside specular on day 240. In Fig.2 and several subsequent plots the abscissa is Satellite Declination - Solar Declination. This quantity is a useful angular measure relative to the specular event. It increases with time, becoming zero at the mid-specular configuration. One notes in the plots in Fig. 2 that there are two brightness variation time scales involved; the strong slower overall modulation by the specular event, and a more rapid nightly "phase function" with a much weaker modulation, which in all but one case is less than about ten percent of the maximum. Fig.3 shows the V magnitude phase curves for these two objects with the Day 240 phase curve of object 20873 for comparison. Note that the vertical scales for the two plots are the same, but displaced, so that

the Day 240 plot can be included. On day 280 satellite 20872 is just over one magnitude brighter than satellite 20873. This is precisely what Table I implies with the ratio of the cylindrical areas being 2.64, which corresponds to a magnitude difference of 1.1 magnitude. The weaker nightly phase function modulation mentioned above is hardly noticeable in the magnitude plots , suggesting it is much weaker than the typical phase function behavior for the cylinders at any other season, for example, on day 240 . Also, these plots show the gradual transition into and out of the specular configuration. We may thus conclude that during the typical ground-based sensor specular observing period that the cylinders remain fairly constant in brightness, with discrete brightness steps occurring between succeeding evenings. The only exception to this is the nearly one magnitude change for 20872 on night 281, where it appears to have been observed when the steepness of the transition out of specular and the nightly phase function, perhaps enhanced for some reason, conspired to produce a total loss of about one magnitude during the night.

Normalized counts for the filters are used for plots in Figs.4-7. In each case the count total has been divided by the maximum count rate for the object. For example, Fig.4 contains a plot of the normalized U filter measurements with the overall behavior virtually the same for both. Thus a single representation is sought. Searches for the best analytical representation for the brightness variation , and the physical nature of the problem suggest that the region near the maximum may be relatively flat. For this reason we force it to be flat, and seek a simple symmetrical representation for the brightness drop off on both sides of the peak. Since we are aware of a nightly phase function behavior, the specular function is found by fitting only the nightly peak count in each case. The specular function is thus assumed to be of the form:

$|X| \leq 0.15 \qquad S = 1$

$|X| > 0.15 \qquad S = EXP[-(|X|-0.15)/C_1]$

where X = (SATELLITE DEC.) - (SOLAR DEC.) as in the figures, and 0.15 appears to give the most consistent results for both satellites. Fig. 5 shows a similar result for both the V and B filters for satellite 20872, with a somewhat better fit for V and B filters for satellite 20873 in Fig. 6. The resulting best values for C_1 are given in the following table.

	20872	20873
U	0.9	0.9
B	0.35	0.5
V	0.35	0.5

TABLE II C_1 VALUES FOR SPECULAR FUNCTIONS

Fig.7 contains a plot of these specular functions for the values C_1 = 0.9, 0.5, 0.3. These specular functions are then a starting point for the development of algorithms for planning and interpreting photometric measurements made near the specular seasons for these cylindrical satellites. It is interesting to note that these values imply that the U (ultraviolet) specular function describes an angular spread that is significantly greater than for light passed by the longer wavelength filters, and

that the U behavior is virtually identical for the two satellites. For both satellites the B and V filter behaviors agree but, for unknown reasons, differ between the two satellites. Based upon these results it is clear that the specular seasons extend substantially for several days before and after the instant of the optimum specular geometry. In fact, the U results suggest that significant brightening should be present up to perhaps a week or so before and after the specular maxima. This is of considerable consequence for U measurements by space-based sensors.

An alternative viewpoint is in terms of the measured satellite "colors" B - V, and U - B as shown in Fig.8 . In this case +14.0 has been added to the actual abscissae values for Day 240 measurements so that they can be included to show a typical non-specular measurement. For reference, the values for the Sun are: $(B - V)_{SUN} = 0.64$, and $(U - B)_{SUN} = 0.13$. The figure shows that for a typical day (Day 240) the measured B-V values for satellite 20873 move within a small range approximately .15 magnitudes redder (i.e, more positive) than the solar value, while the measured U - B values perform a similarly shaped curve which passes through the solar value twice. On the other hand, by the time of the first set of observations on night 277 both the satellites have B - V values considerably "bluer" (i.e., less positive), while the U - B measurements of both are dominated by an ultraviolet brightening of about 1.6 magnitudes ! As the mid-specular geometry is approached, the B - V measurements for both approach very nearly the solar value. U - B becomes closer to the solar, but never quite reaches it at mid-specular due to a lingering excess of ultraviolet light. Apparently the solar panel UV coatings are doing their job.

The source of the angular spread in the reflection represented by these measured specular functions is likely due to several causes. The actual distribution of the alignments of the individual pieces of the solar panels would create some breadth in the beam. That would be expected to be the same for U, B, and V , however. The roughness of the surfaces themselves would produce some additional scattering of the nearly collimated incident solar radiation, and it seems reasonable to expect surface roughness effects to have a $1/\lambda$ dependence, thus producing a greater angular spread for U. That these solar panel elements are coated so as to have high reflectivity for ultraviolet undoubtedly plays some role in the process.

This work has been supported by the Department of the Air Force under Contract #F19628-90-C-0002.

1. R.J. Bergemann, Private Communication, 1992.

HUGHES CYLINDRICAL SATELLITES

COMPARISON

SSC #	20872	20873
NAME	SBS6	GAL VI
TYPE	HS-393	HS-376
TOTAL HT.	10.0 m	6.6 m
ANTENNA		
D	2.4 m	1.83 m
CYLINDER		
H	7.6 m	4.77
D	3.64 m	2.2 m
AREA	27.7 m^2	10.5 m^2

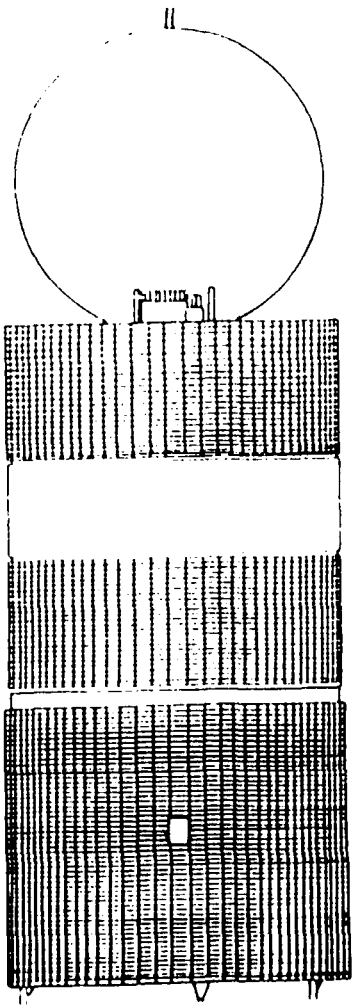

TABLE I. A COMPARISON OF HUGHES CYLINDER TYPES 376 AND 393.

FIG.1

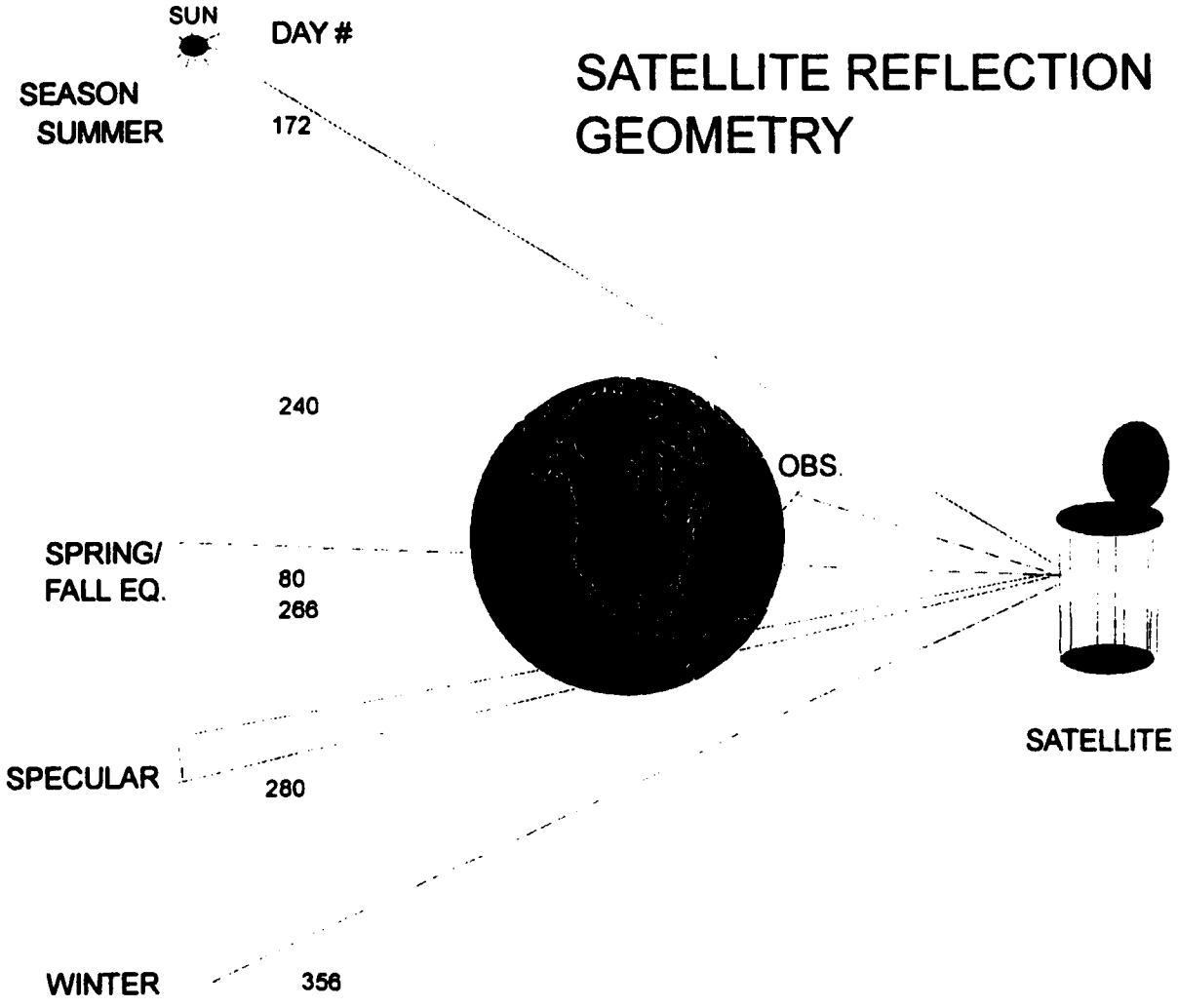
SUN
DAY #
SEASON
SUMMER
172
SATELLITE REFLECTION
GEOMETRY
240
OBS.
SPRING/
FALL EQ.
80
266
SATELLITE
SPECULAR
280
WINTER
356

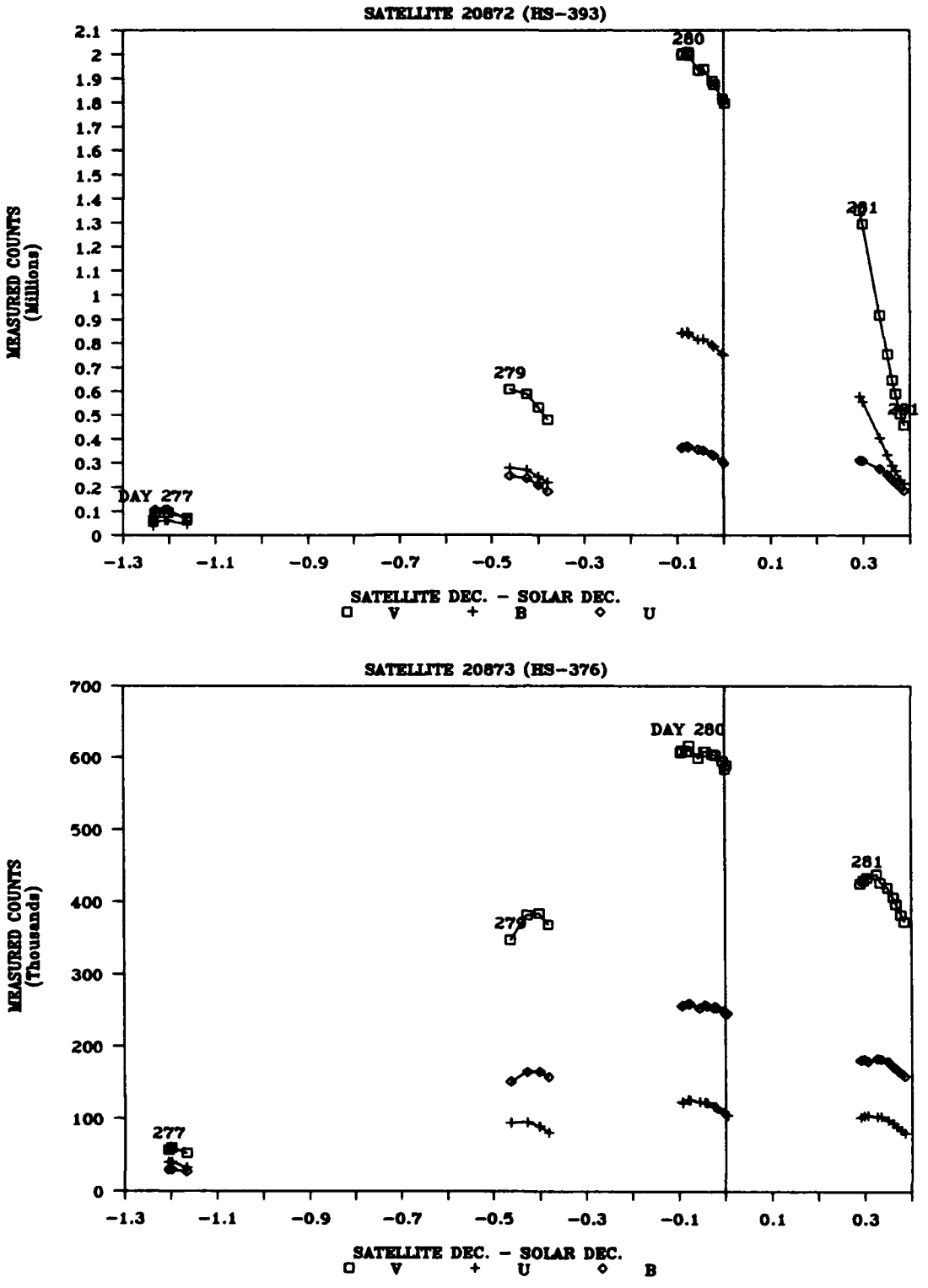

FIG.2 U B V FILTER MEASUREMENTS

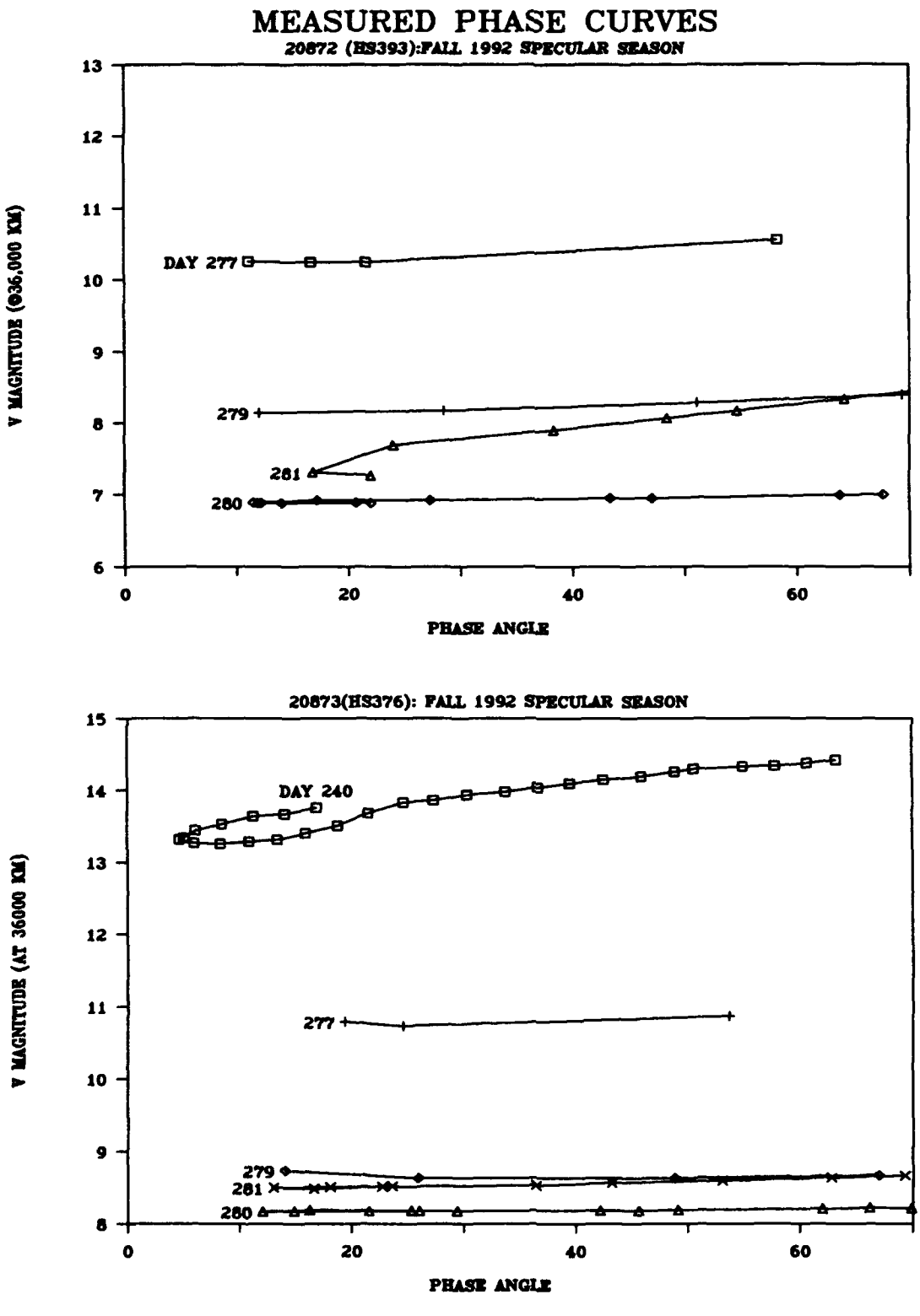

FIG.3 V FILTER PHASE CURVES

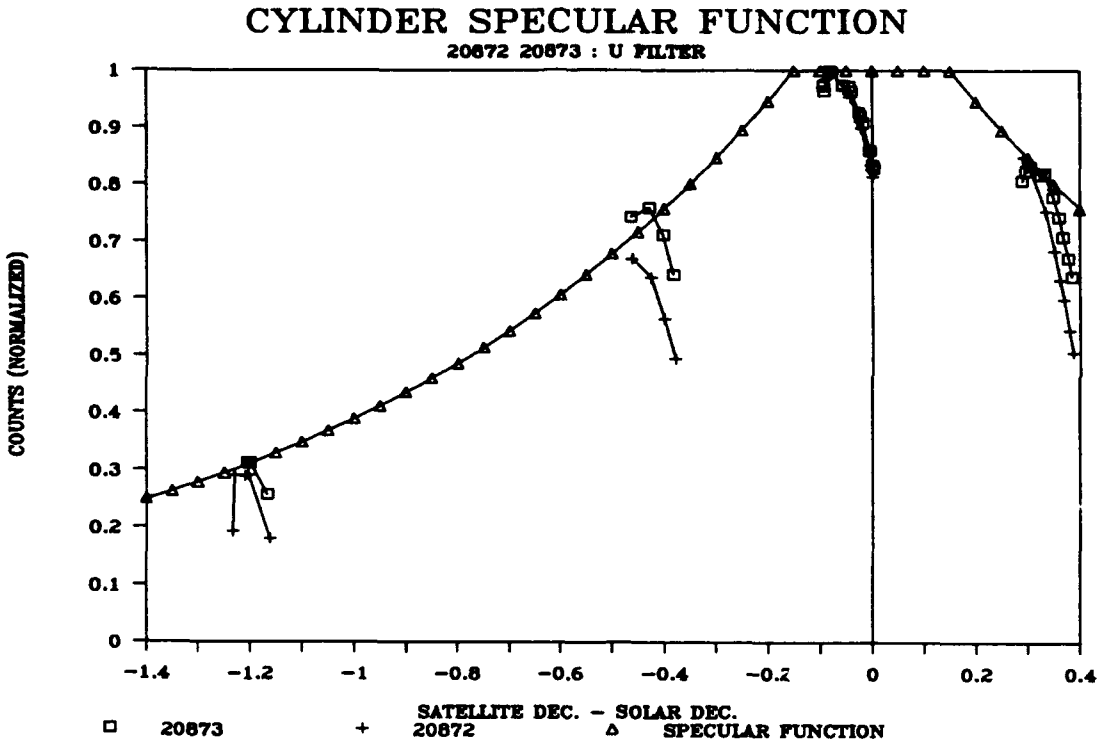

FIG.4 U BAND SPECULAR FUNCTION

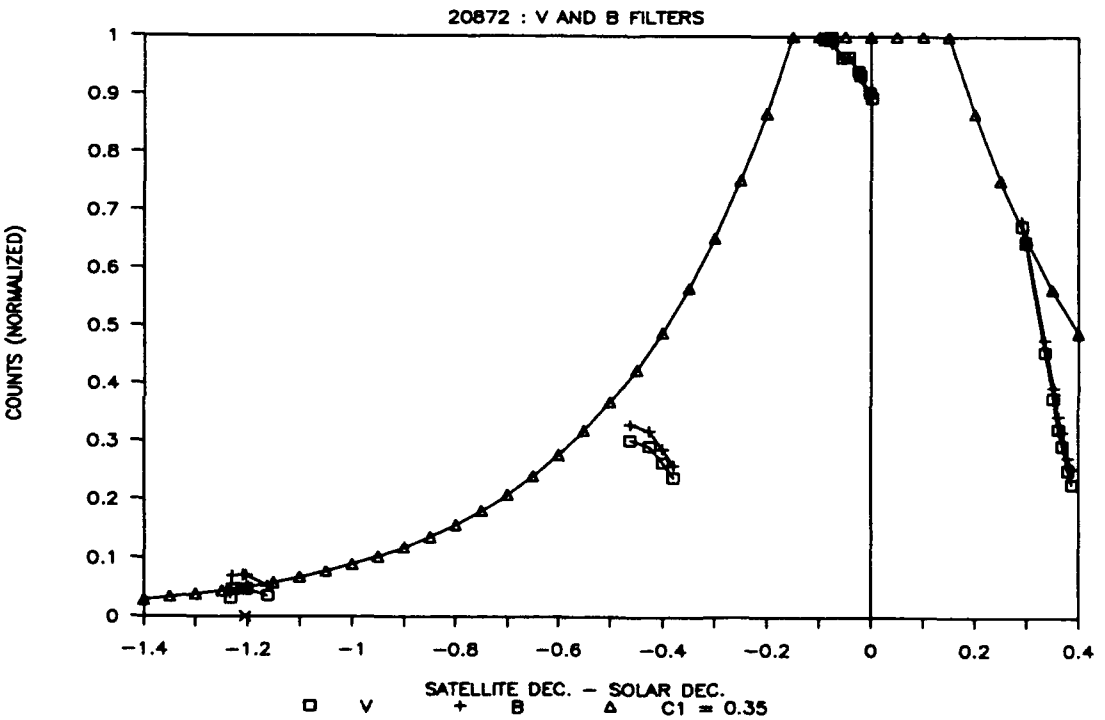

FIG.5 SPECULAR FUNCTION FOR 20872 (V AND B)

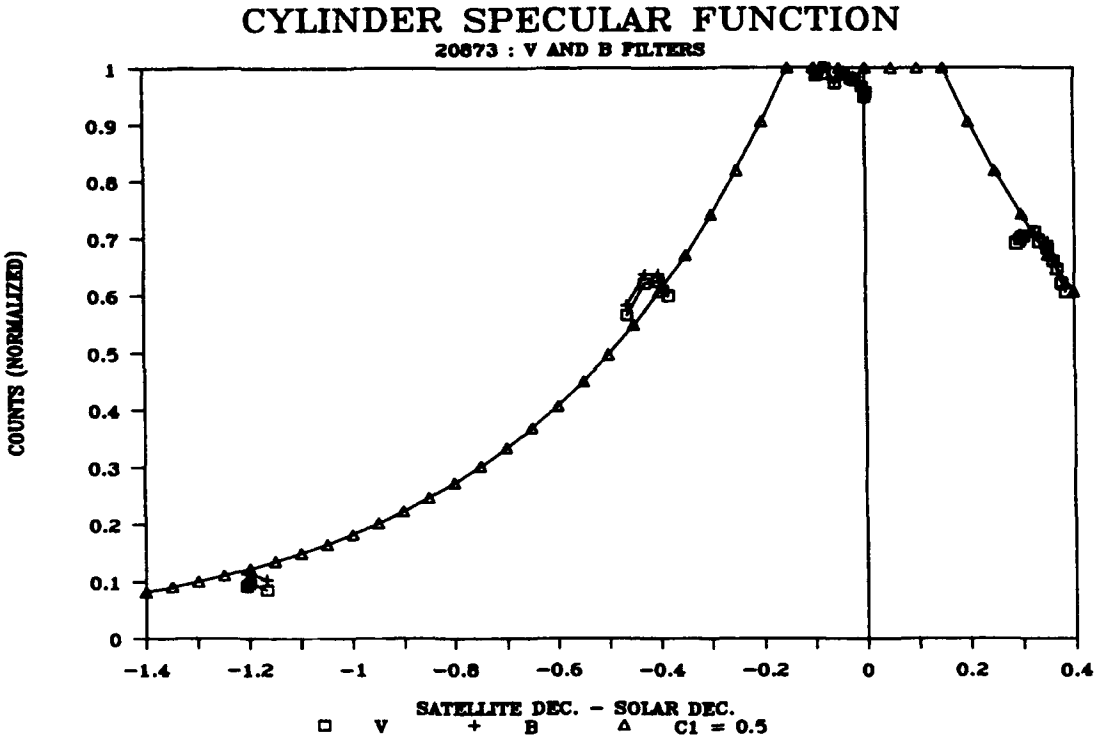

FIG.6 SPECULAR FUNCTION FOR 20873 (V AND B)

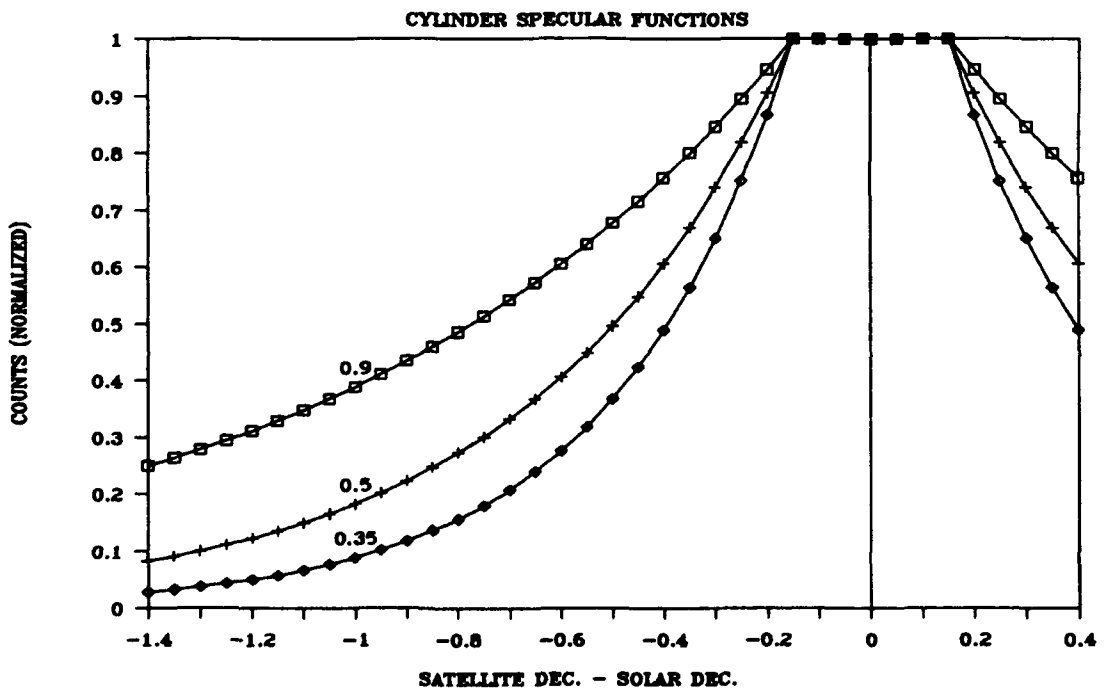

FIG.7 COMPARISON OF SPECULAR FUNCTIONS

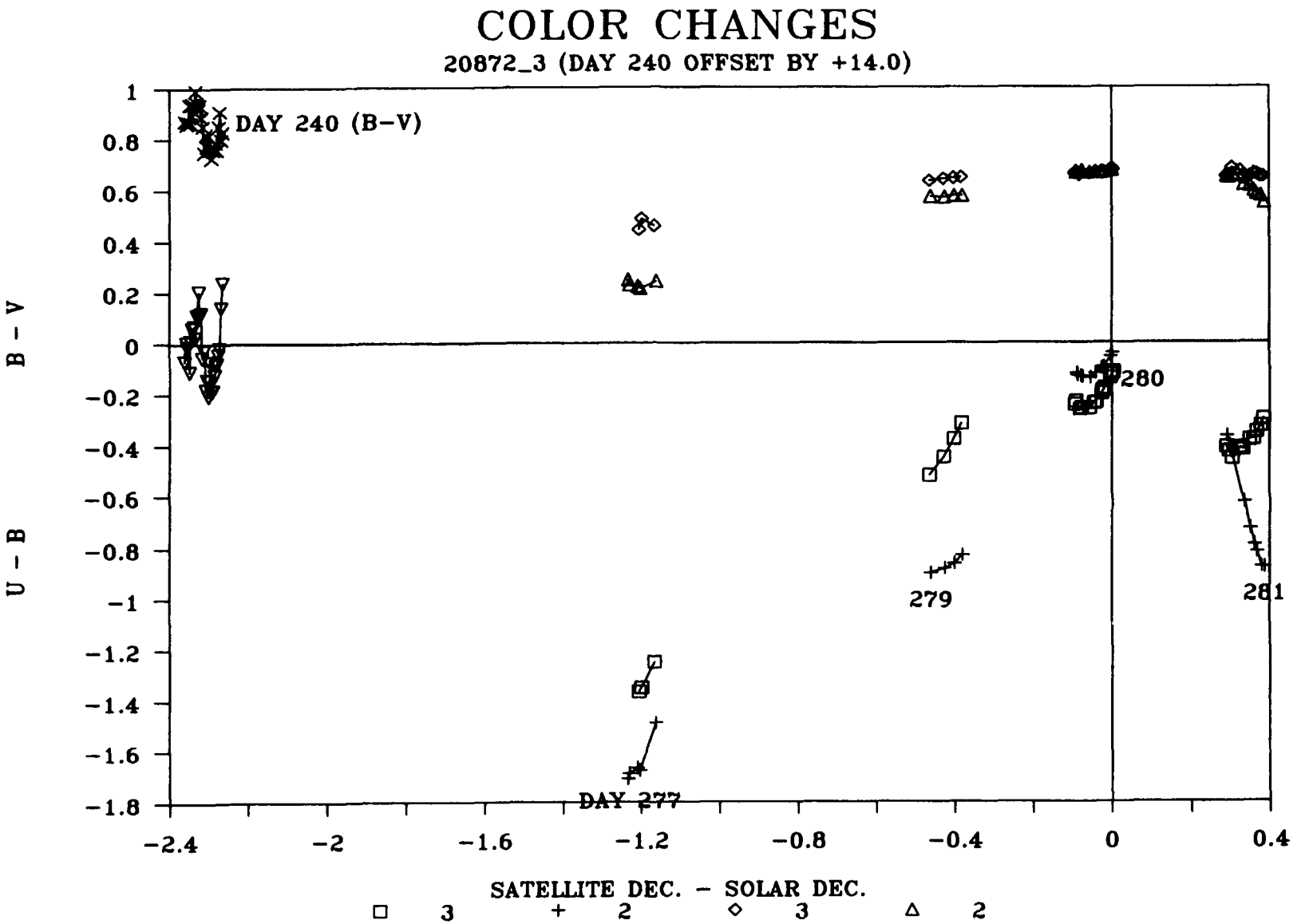

FIG.8 SATELLITE COLORS IN AND OUT OF SPECULAR SEASON

Space-Based Visible Sensor Scheduler (SBVSS) Advanced Algorithm Development

A. R. Newman, E. S. Rozier, S. E. Andrews
(Surveillance Techniques Group, MIT Lincoln Laboratory)

1. Introduction

The Space Based Visible Sensor Scheduler (SBVSS) design team at MIT Lincoln Laboratory is investigating two new techniques that will be used to schedule space object observations for the Space Based Visible (SBV) sensor: global scheduling and N-step look ahead scheduling.

The current standard, known as local scheduling, is used at ground-based sensors such as Millstone. Local scheduling considers the current status of the sensor and its targets and determines the single "best" object to observe next. The implication of the current observation choice on later observations is ignored. On the other hand, global scheduling algorithms predict the scheduling environment for the entire time allocated for the task, a computationally expensive operation. N-step look ahead algorithms bridge the gap between local and global scheduling by considering the current position of the sensor and possible positions for the next several *(N)* looks. This is an attempt to gain some of the benefits of global scheduling at a greatly reduced computational expense. For space-based space surveillance, the scheduling environment to be determined includes the locations of the sensor, of all targets of interest and of all regions constrained by the operational limitations of the sensor and its platform.

This presentation focuses on two algorithms: a global algorithm in the concept stage, and an N-step look ahead algorithm which is currently being implemented for use by the SBVSS.

2. Motivation

The primary motivation for a global scheduler is to take advantage of the ability to predict the content of the viewing space for the entire time allocated to a schedule and plan ahead so that viewing opportunities of special interest are not missed. The N-step ahead algorithm is designed to limit the computational burden that global algorithms impose by reducing the amount of lead time considered for scheduling, while considering enough to gain an advantage over a local algorithm.

3. Current Technology: Local Scheduling

The current local ground-based scheduler, Millstone Dynamic Scheduler (MIDYS), has been used at Millstone for over 15 years. It runs in real-time, selecting the ten best objects to track next, and relies on an operator to choose which of those objects to schedule. MIDYS uses historical element set information, target cross-section, SSC priority, and tasking status to compute a "figure of merit" which is maximized for objects that are best to track next.

The baseline local space-based scheduler, called the Space-Based Dynamic Scheduler (SPADYS), is based on MIDYS. However, SPADYS assumes no real-time communication with the sensor or an operator, so it simply selects the object with the highest merit value to track next.

This introduces a complication shared by all the SBV schedulers: there is no way of actually knowing whether or not the tasking requirements have been achieved until the schedule is completed and observation results are received. MIDYS, on the other hand, has the capability to adjust mid-stream and re-acquire targets which have not been tracked as predicted.

4. SCHEMER

The global scheduling technique under evaluation is called "Scheduling by Merit". This section discusses a particular Scheduling by Merit algorithm called SCHEMER.

SCHEMER considers the potential sensor viewing space as a full sphere, with the sensor at the center. The sphere can be pictured as a soccer ball, where each polygon on the surface of the ball represents the position of a possible sensor look. The black spots represent constrained areas and the white spots represent feasible sensor looks. These black and white spots change position as target objects, the earth, the sun, and the moon move relative to the sensor.

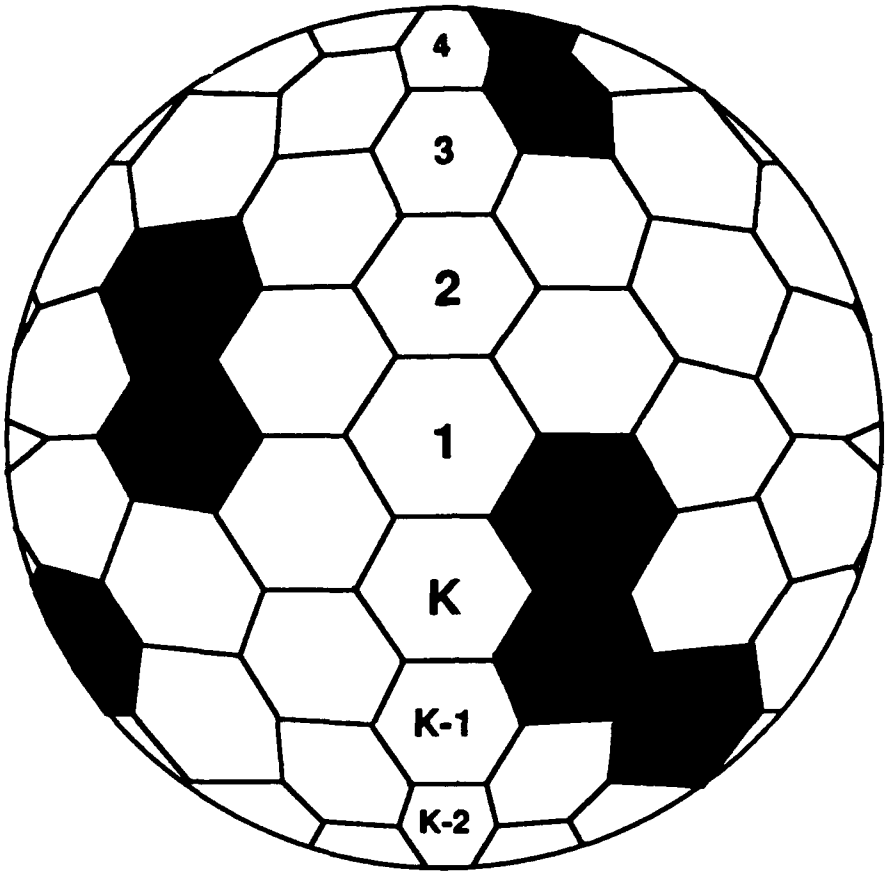

Figure 1: SCHEMER Viewing Space

Rather than using soccer ball-style polygons, SCHEMER divides the sphere into distinct equal-area cells, which mimic the field of view of the sensor. As shown in Figure 1, these cells are numbered from 1 to K in a sensor-centered inertial system. Note that this system is really two dimensional. Range to the potential target is not directly considered because the SBV is an angles-only sensor.

Rules exist which allow for the determination of constrained areas over time. With the user-inputted list of targets and initial element sets for each target, SCHEMER can generate a "movie" showing the relationship of all the targets and all the constraints to the sensor over the entire time allocated for the schedule. This movie (see Figure 2) is broken down into $f*t_{dc}$ snapshots, where t_{dc} represents the data collection time for a look and f represents a fixed number of intervals into which t_{dc} is subdivided. The snapshots are integrated in such a way that the benefit of staring at a cell over an extended data collection period is highlighted.

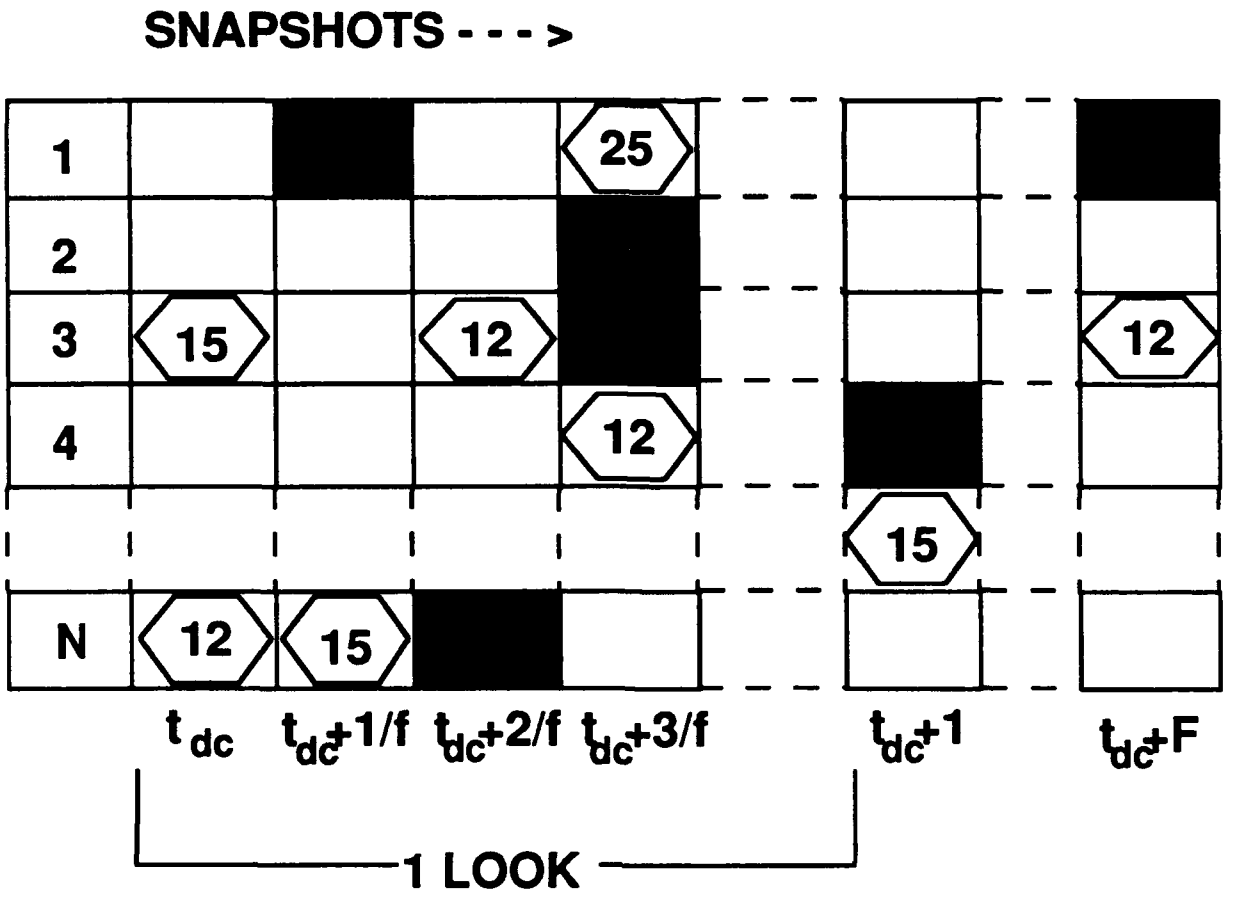

Figure 2: SCHEMER "Movie"

A figure of merit is used to guide SCHEMER in choosing which cells to look at in what order. The user is allowed to weight the importance of various factors which go into this figure of merit and therefore into SCHEMER's decision-making process. For example, it may be more important to gather data on one particular target over another, it may be important to acquire a certain target regardless of the cost, or it may be important to minimize the cost while collecting data. For SBVSS, specific factors which will be considered include cryogen use, thermal conditions, and SSC priorities. SCHEMER's decision-making process combines these and other components into a single figure of merit in such a way that this value is maximized for the most important looks.

The next phase of the SCHEMER algorithm involves building a set of merit-ordered trees to keep track of the scheduling possibilities. Conceptually, SCHEMER begins by constructing many partial schedules simultaneously. Throughout its execution, the algorithm discards partial schedules as they become infeasible or ineffective. At the end, SCHEMER may produce one or several complete schedules. A Schedule Evaluator, also under development

by the SBVSS design team, can be used to determine which complete schedule is most desirable with respect to the objective function.

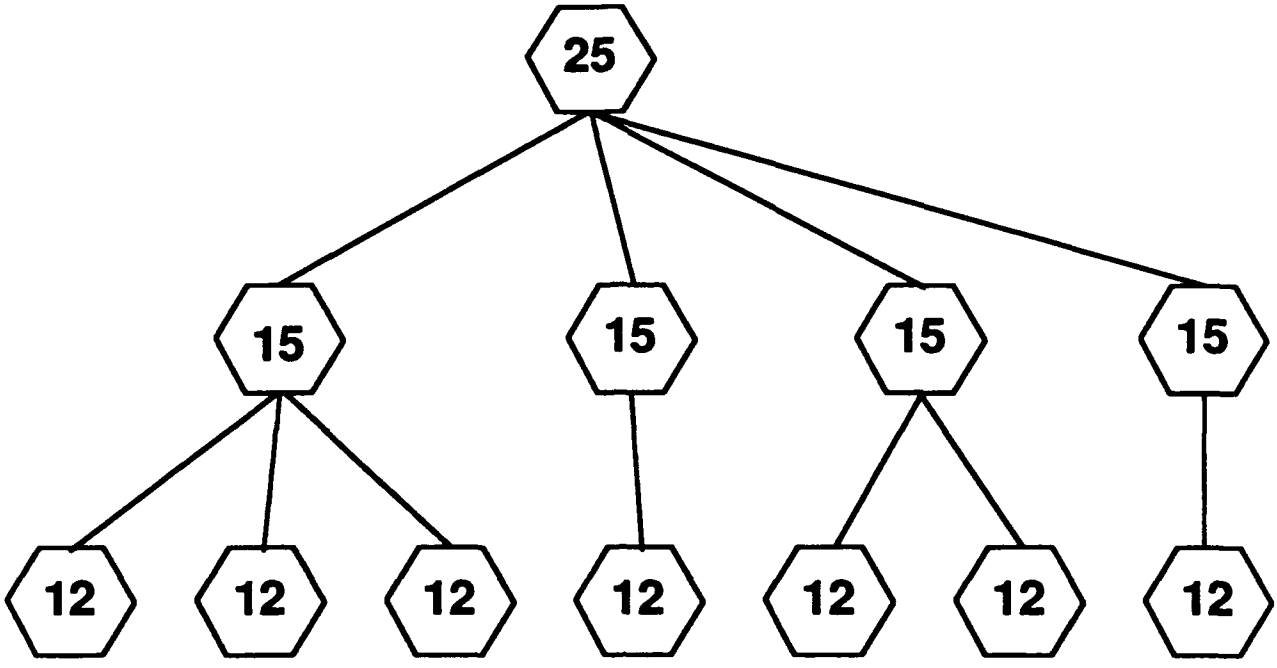

Figure 3: SCHEMER Sample Ordered Tree

To begin building the ordered trees, SCHEMER selects the looks or cells with the highest merit in the entire time allocated for the schedule. One tree is initiated for each highest-merit look and multiple trees may be constructed simultaneously. Note that the trees are maintained in order of merit only, and not necessarily in chronological order. Figure 3 shows an example of such an ordered tree.

Once the top-level looks are chosen, the merit of each remaining set of looks is recomputed to account for the top-level choice. For example, this could mean that the merit will be decreased in cells containing the targets already viewed in a top-level look. It could also mean that cells will be eliminated from consideration if they occur before or after a top-level look and cannot realistically be reached given the sensor's dynamics.

The cells with the highest merit after this recalculation are added to the ordered tree as nodes below the root. The tree expansion process continues until a predefined threshold merit or node level is reached, or until no more feasible cells remain. In this way, a set of trees is built that lays out paths through the "hottest" spots on the spheres in the snapshots.

Finally, SCHEMER schedules the intervals between those snapshots that contain hot spots. The tree building algorithm is repeated

recursively, using the times between snapshot intervals as the endpoints for the sub-schedules.

5. The N-Step Ahead Single Object Scheduler

The N-step ahead technique being pursued is called the "N-Step Ahead Single Object Scheduler" (N-STASOS). N-STASOS takes as input a nominal element set for the object being sought and the uncertainty for each orbital element. This uncertainty is given as a standard deviation on a Gaussian (normal) probability distribution. A discrete probability distribution (with granularity at least one order of magnitude finer than the sensor field of view) is generated in orbital element space using these standard deviations.

To create a first-cut schedule, N-STASOS assumes an average complete look time, t_{avg} (which includes maneuver time, settle time, data collection, and signal processing), and assumes that each look begins t_{avg} seconds after the previous look. The algorithm converts the distribution in orbital element space to Right Ascension/Declination space for N snapshots, each t_{avg} seconds apart.

A value function is evaluated for every RA/DEC cell available for a sensor look. The parameters considered by the value function include: probability of appearance, likelihood of detection (visibility), maneuver time to the desired position, violation of pointing constraints, and the use of sensor resources (cryogen, memory, power). Each of these parameters can be weighted based on user choice, and on a standard objective function, similarly to SCHEMER. N-STASOS will choose a first-cut schedule which maximizes the sum of the value function over N steps.

Figure 4 shows the generation of several frames of distribution data containing the RA, DEC, and probability of appearance for all possible looks at intervals of t_{avg} seconds. This information is used to calculate the value of each look and generate schedules, working to find the schedule with the maximum overall value.

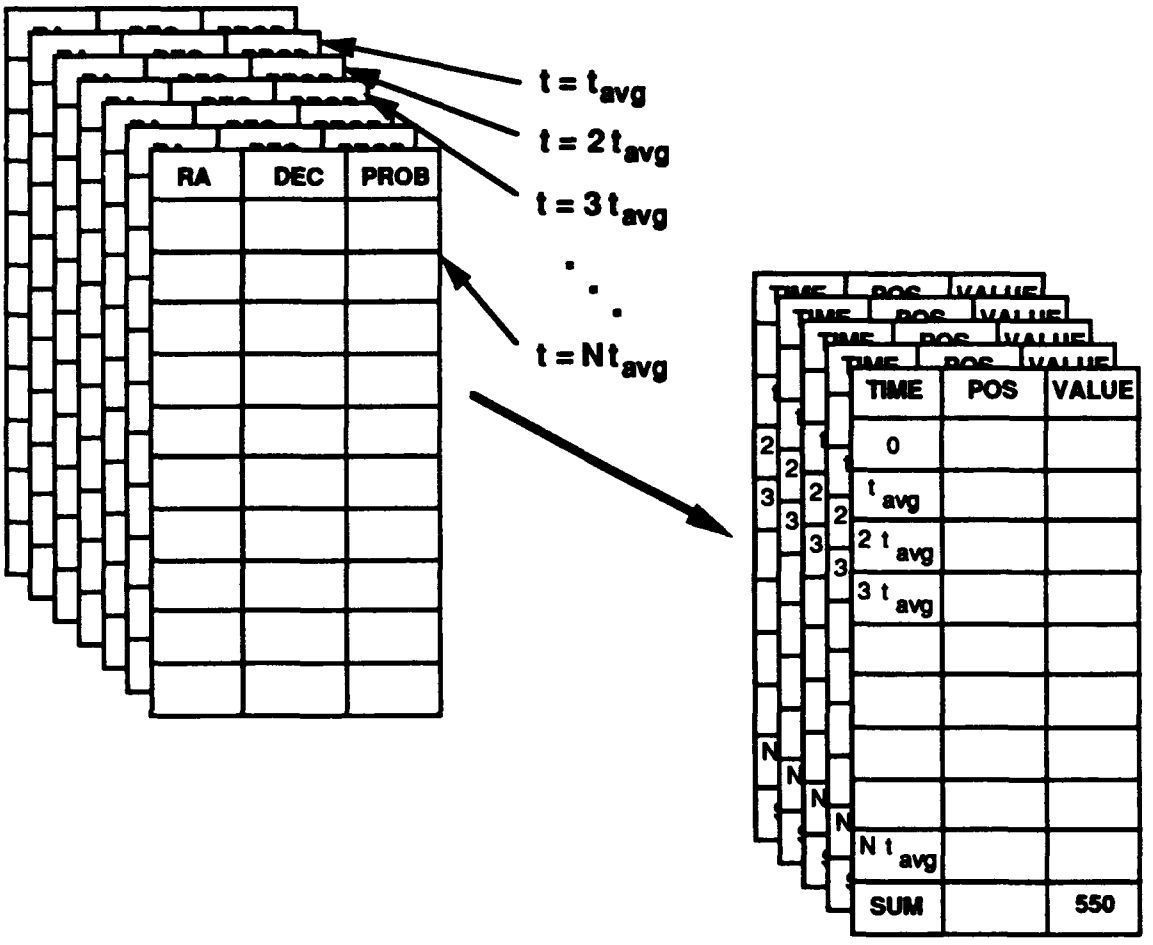

Figure 4: N-STASOS Initial Pass

Each step of the first-cut schedule is then examined to determine how much time should be spent at each calculated position. For example, it may be advantageous to stay at Position 1 longer than originally planned to allow more of the probability distribution to drift through the sensor field of view. N-STASOS considers this possibility for each of the N steps and updates the looks accordingly.

When the N-step schedule is completed, the first step is considered fixed, and the area of consideration moves to steps 2 through N+1. This is shown in Figure 5. The N+1st snapshot (t_{avg} seconds after the Nth snapshot) is calculated and appended to the first-cut N-step schedule, which in turn is recalculated to account for the new information. This process is repeated until a complete schedule is generated for the time allowed.

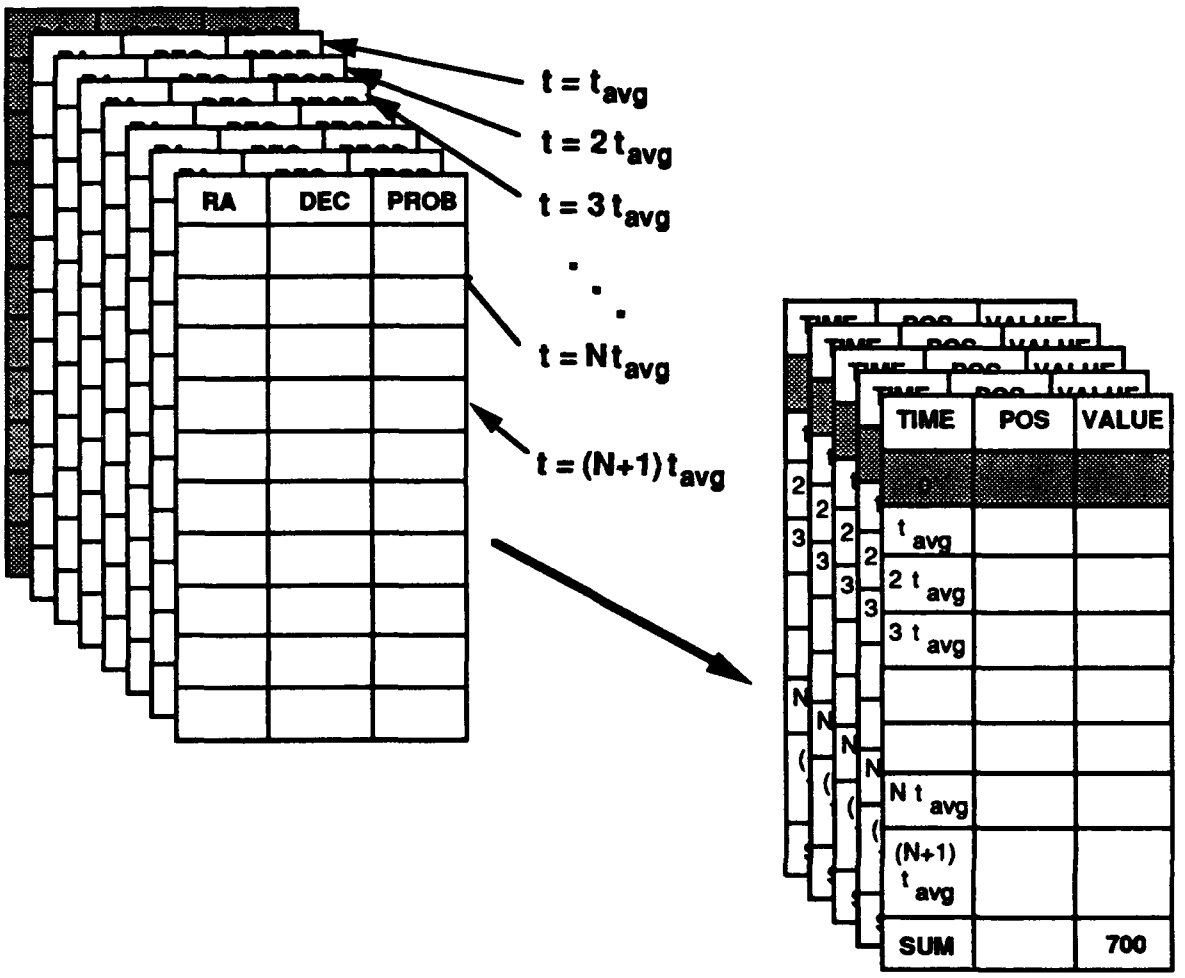

Figure 5: N-STASOS Second Pass

This particular algorithm for N-STASOS is a brute force method. Other methods will be evaluated in hopes of increasing computational efficiency. These methods include:

- A nearest neighbor algorithm, in which each step places the sensor at a position adjacent to its previous position (a particularly good choice for slow sensors like the SBV).

- A semi-local algorithm, where the boresite pointing of the sensor is calculated locally (i.e. using only the sensor's current position to determine the next step), but a 4-step ahead calculation is performed to determine the order of use of the SBV's 4 CCDs.

6. Practical Applications

Two common types of tasking to be considered when planning for the scheduling of a sensor are routine catalog maintenance tasking and new launch tasking. In the first case, there are a large number of objects to search for and a fairly good group of initial element sets with which to acquire the targets. In the second case, there is only one target, and a small group of predictive element sets that can be used to acquire the new launch in its parking, transfer, or final orbit.

SPADYS, SCHEMER, and N-STASOS all have the ability to schedule for either type of tasking. However, SCHEMER will probably be better suited for catalog maintenance tasking, where a large number of opportunities over a long period of time need to be considered. On the other hand, N-STASOS will probably perform better for launch tasking because it can look far enough ahead to take advantage of optimal viewing opportunities while remaining a dynamic scheduler that can re-plan as likely target orbits are identified. N-STASOS may also be particularly useful for debris searches, expired element set searches, and uncorrelated target (UCT) re-acquisitions.

The MSX Surveillance Principal Investigator Team Data Analysis Center

M.T. Lane (MIT Lincoln Laboratory, Surveillance Techniques Group)

1 INTRODUCTION

The primary objectives for the MSX Surveillance Principal Investigator Team are the following:

1) Obtain critical observations with MSX sensors to address SDI Midcourse Surveillance Issues, and
2) Demonstrate the functional capability of the MSX sensors for Space-Based Surveillance.

Critical observations to satisfy (1) will involve "Above-the-Horizon" surveillance and will focus on RSO signatures in both stressing and non-stressing backgrounds. The functional demonstration of the MSX for space-based surveillance (2) will focus on the ability of the MSX to inform, protect space-based assets, and negate threats to these assets. In order to demonstrate these components, the following are critical:

a) Search, acquisition, track, and handover,
b) RSO discrimination and identification using metric and radiometric data,
c) Integrate data from the MSX with ground-based data on RSOs, and
d) Provide a technology legacy for future systems.

Specific experiment plans have been written for the MSX sensors so that data can be collected to satisfy the objectives mentioned above. Several of these have been described for the community during the 1992 Space Surveillance Workshop and involve a "walk-before you run" prioritization which allows investigators to understand the MSX sensors before they are used for special surveillance functions. The experiment plans involve data collection to understand the Non-Rejected Earth Radiance (NRER) and backgrounds, metric and radiometric calibration, the ability to search, acquire, and track new launches from both the ground or space-based shuttles, RSO routine tasking, geosynchronous belt search, debris, and Signature Object Identification (SOI).

The analysis task for the Surveillance Principal Investigator team is enormous, as the data are expected to flow generously from the spacecraft once it is in orbit. Data from each of the three prime science sensors on the MSX must be analyzed carefully from a surveillance point of view. These optical sensors range in wavelength from the .3 micron band Ultraviolet (UVISI), through the visible band (SBV), to the long-wave (24 micron band) infrared (SPIRIT III). In order to prepare for this analysis task, a Data Analysis Center (DAC) is being designed to process all of the space surveillance data collected by these science sensors on board the MSX. The prime functions of the Surveillance Data Analysis Center (SDAC) are the following:

1) Analyze all data from the MSX Space Surveillance Experiments,
2) Understand the utility of SBV, SPIRIT III, and UVISI for space surveillance,
3) Prepare a catalogue for accessing MSX space surveillance data,
4) House "CONVERT" and other data reduction algorithms for each of the science sensors, so that raw data can be converted into calibrated data products (CONVERT is a special name in the MSX program parlance, and it refers to an algorithm developed by the instrument team which is designed to convert raw telemetry of a downlink science data stream into image data translated into well-known engineering units. SBV, UVISI, and SPIRIT III will each have their own CONVERT programs, which will bring users to a standard starting place for further analysis),
5) Provide analysis tools which are state-of-the-art for analyzing space-based metric and radiometric data, and
6) Aid in mission planning for all MSX space surveillance experiments.

2 DATA ANALYSIS CENTER ARCHITECTURE

The architecture and supporting data flow for the SDAC is presented in Figure 1. The telemetry from the spacecraft (containing the raw science data from the MSX sensors) first goes to the Mission Processing Center (MPC) at the Applied Physics Laboratory (APL). After data from the individual sensors on the spacecraft have been separated out, data from each of the prime science sensors will be distributed by the MPC to a Backgrounds Data Center (BDC) at the Naval Research Laboratory (NRL) for archival and distribution to the analysis and processing centers. For quick reaction events (such as a new launch search), special data products from the SBV only can be sent via electronic link directly to the SBV Processing Operations and Control Center (SPOCC) at MIT/Lincoln Laboratory (MITLL). The SDAC will also be located at MITLL, and data from SPOCC will be easily retrieved via a local area ethernet and optical disk and tape storage media. In addition, corollary sensor data for particular experiments from ground-based sites will be available at the Millstone Hill Radar Facility, and access to these data are also in place. Archival of data in the SDAC will occur on an optical disk and using an Oracle Relation Data Base Management (RDBM) system. All analysis programs will be available in the SDAC, and preprocessing programs such as SPIRIT III CONVERT, UVISI CONVERT, and SBV Data Reduction will be on-line for immediate access.

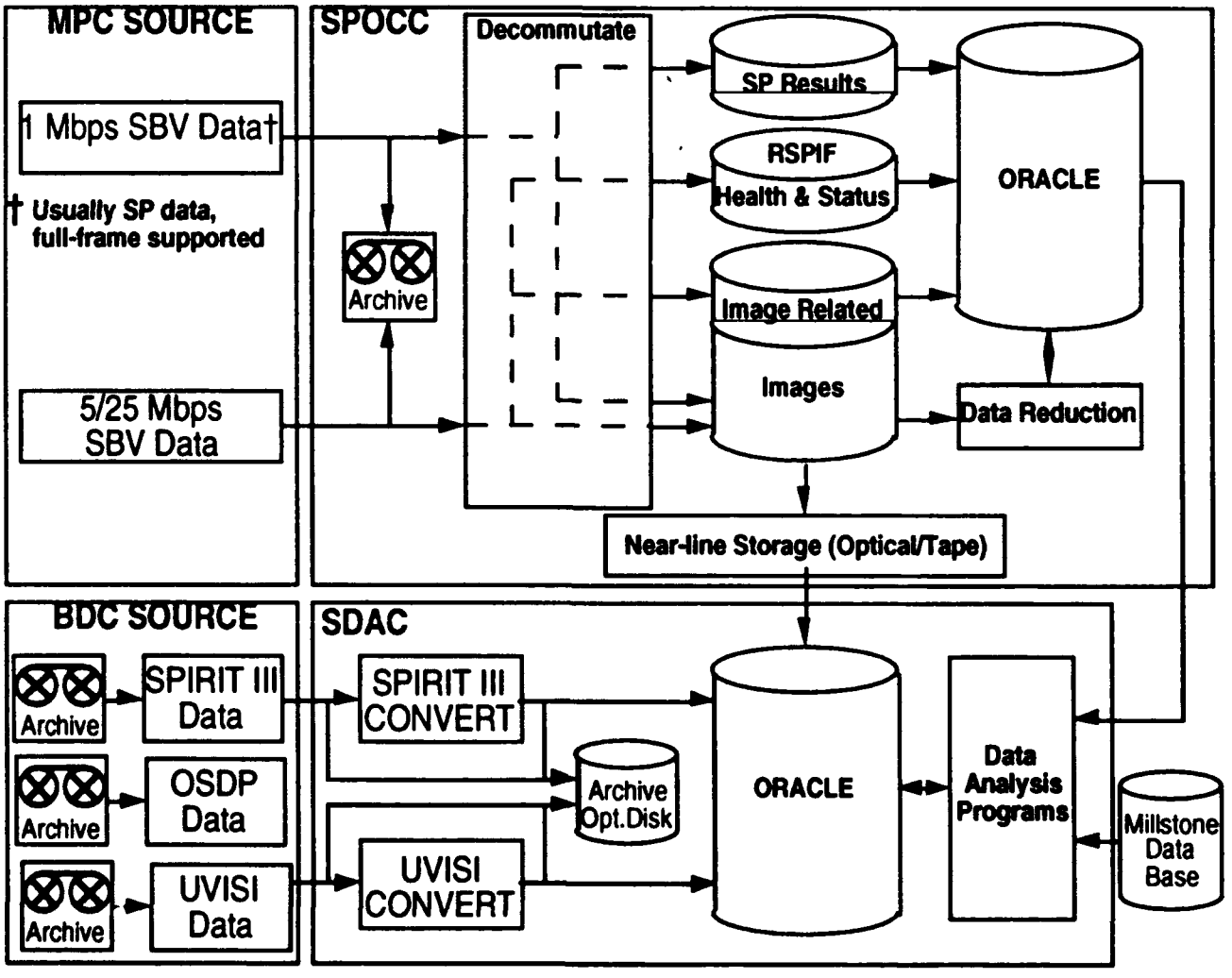

Figure 1: SDAC Architecture and Supporting Data Flow

The Surveillance Catalogue will be necessary for the user to search and select a data set based on information on experiment type, time, and sensors used. In addition, the catalogue can indicate corollary and ancillary data related to the specific data collection and other useful information required for analysis. The data flow for the catalogue data base is provided below in Figure 2. Inputs to the catalogue come from the following sources:

1) Mission Operations Center (MOC). This center coordinates all uplink commands to the spacecraft for experiment execution. Information is required which relate data collection events to the planned sequences. Tracking data are also required for an accurate post-fit MSX ephemeris (from the CSTC S-band tracking sites). These data will be provided, in addition to definitive spacecraft attitude data.
2) The BDC will provide SPIRIT III and UVISI CONVERT algorithms, all SPIRIT III, UVISI, OSDP (an On-board Signal Processor for the SPIRIT III data), and SBV raw data, and any Data Quality, Data Measurement, and Data Summary Indices (DQI, DMI, and DSI).
3) The SDAC will input to the catalogue names and locations of converted data sets, simulated science data, corollary sensor data, and auxiliary data.
4) SPOCC will provide SBV CONVERT, SBV Data Reduction, and any SBV data and related products.

Finally, a catalogue user interface will be constructed for easy access to the catalogue products. The interface will involve a user-friendly windows environment, with point and click menus available.

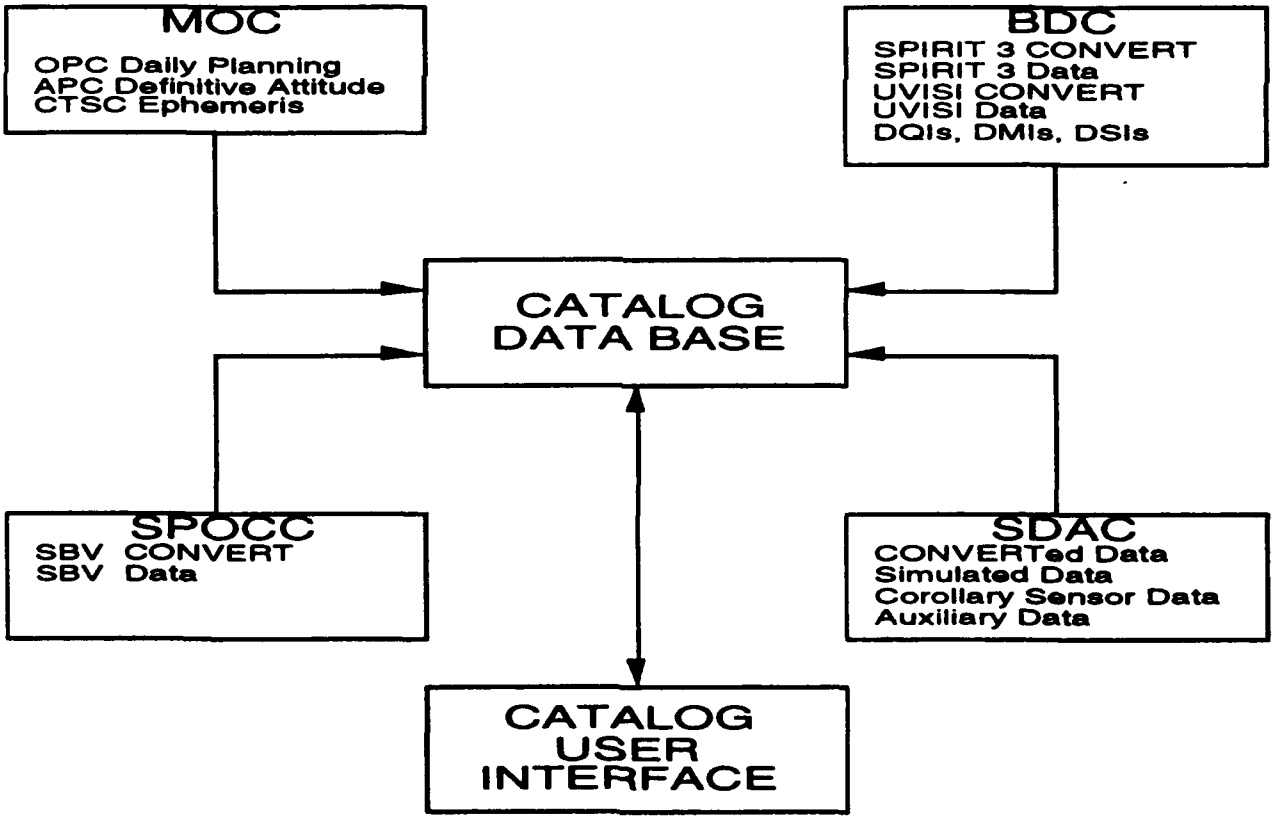

Figure 2: The SDAC Catalogue Data Base

3 DATA ANALYSIS TOOLS

Analysis tools in the SDAC fall into two categories: metric and radiometric processing. The SBV and SPIRIT III are expected to be accurate metric sensors, for collection of "angles-only" data on RSOs. The UVISI sensors are not expected to provide accurate metric observations, but all science instruments will have the capability to collect photometric and radiometric data which should be well-calibrated and useful.

3.1 Metric Processing

Many of the MSX surveillance experiments require a full understanding of the metric quality of the observations. Essential functions of the SDAC are to be able to assess the metric quality of every data set and to be able to analyze specific data sets in more detail. An Orbit Determination and Analysis Workstation is being developed for the SDAC. A projection of the functionality and capabilities for this workstation is presented in Figure 3. This is intended to be an interactive workstation using a windows environment, with point and click interface.

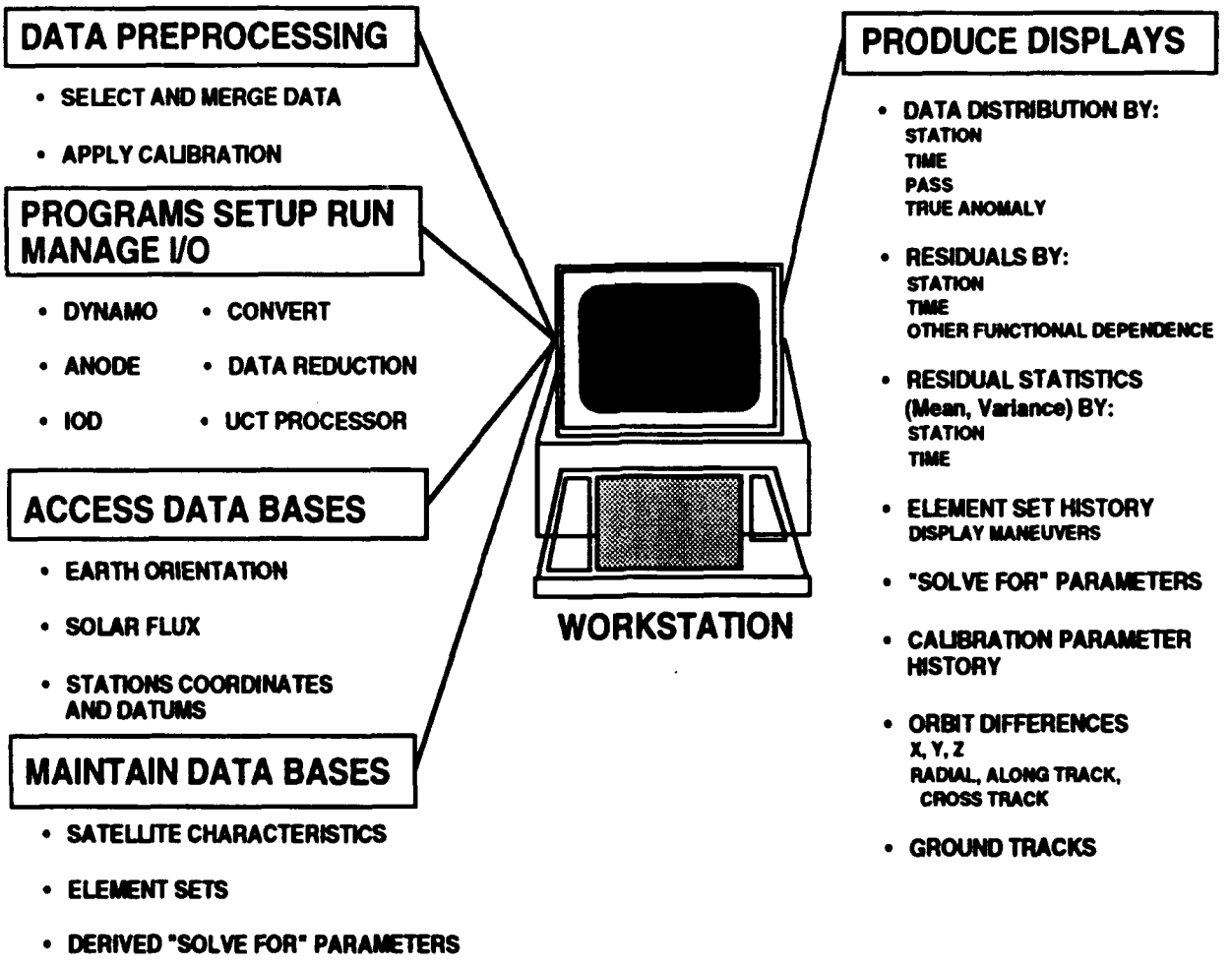

Figure 3: Orbit Determination and Analysis Workstation

Reduced metric data to be analyzed can be selected and merged with corollary data from the Space Surveillance Network (SSN). Before processing, calibration can be applied to the data at the discretion of the user. Metric analysis programs can be run on the selected data. These include precision

orbit determination (DYNAMO), analytic orbit determination (ANODE), Initial Orbit Determination (IOD), CONVERT, SBV Data Reduction, and UCT Processing. The ANODE program will have several well-known propagator (perturbation model) options, including SGP4, ANODE, and revised ANODE.

In order for data to be processed effectively, key data bases must be accessed for force and sensor model descriptions. Earth orientation, solar flux values, and sensor coordinates (including known biases or other datum) are essential to properly model the dynamics of the satellite. On the part of modeling the motion of particular RSOs accurately, satellite characteristics, element sets, and derived "solve for" parameters (for input to a force model) are all critical.

Finally, the workstation will be able to display to the user results from processing. These are listed in Figure 3 and include data distribution, residuals (with statistics), element sets, and "solve for" parameter histories. The workstation will also be able to calculate and display selected orbit differences and RSO ground tracks.

Given the amount of SBV and SPIRIT III data expected to flow through the SDAC, routine automatic metric processing can be designed using the analysis tools from the workstation. A diagram of the data flow for this processing is shown in Figure 4. This chart shows the data coming into the SDAC from the MSX (via ground relay centers). First CONVERT (or SBV Data Reduction) must be applied to the raw data to isolate RSO detections and produce metric observations in terms of right ascension and declination coordinates. These must be sent directly into a UCT processor to separate those observations

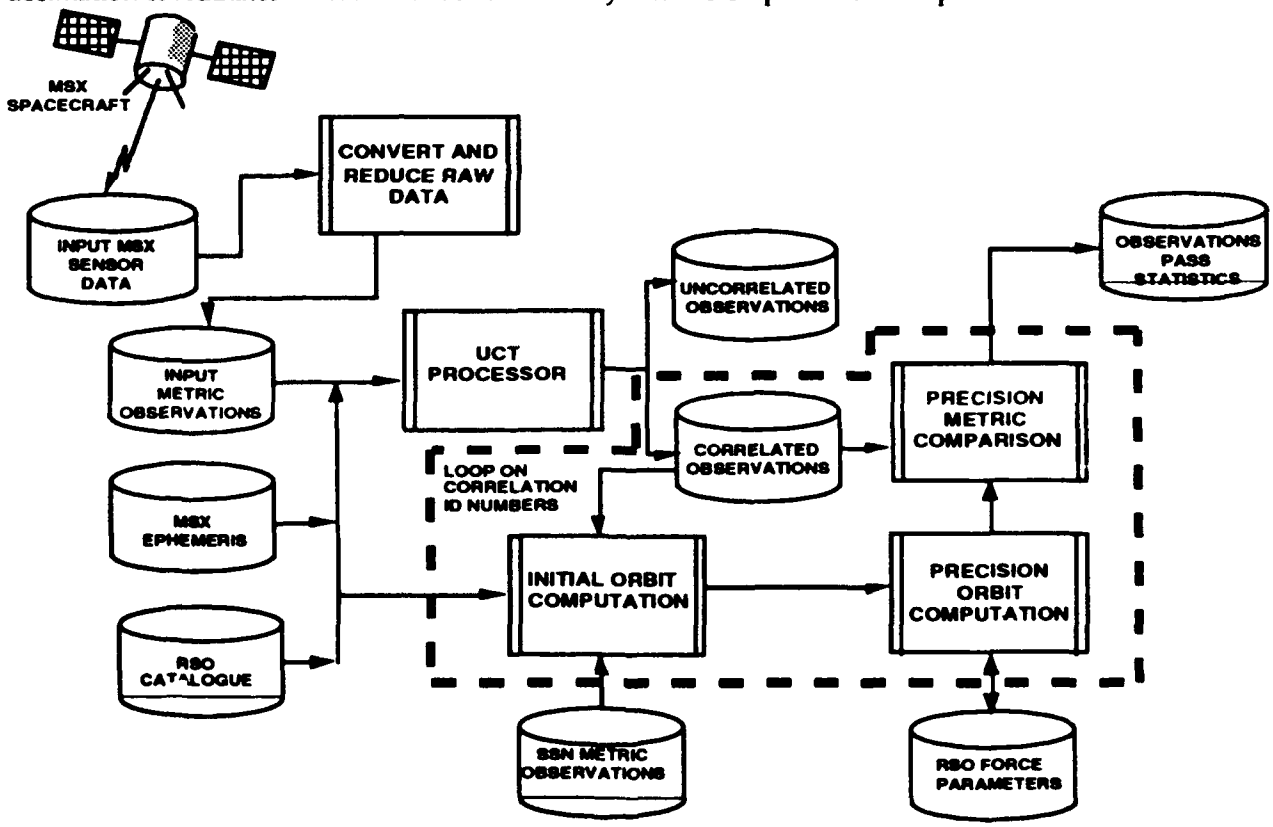

Figure 4: Automatic Metric Processing in the SDAC

which correlate to known RSOs from those which do not. Important corollary data required for all metric processing are shown in Figure 4, and these include the ephemeris of the MSX spacecraft, the RSO catalogue, and other Space Surveillance Network (SSN) metric observations. Now, for every set of

metric observations which correlates to a known RSO, the following procedure is able to deduce observation pass statistics which, in turn, indicate the metric quality of the data:

1) An independent set of SSN metric data on the RSO which correlated to the set of metric observations is collected near the epoch of the data to be analyzed.
2) A good initial orbit is calculated using the SSN data. The initial orbit acts as a starter for a precision orbit computation. ANODE is well-suited for this part of the processing.
3) A DYNAMO precision orbit is computed using only the SSN data. If the RSO has associated with it known force model parameters, then these are used. Updates to parameters such as area-to-mass ratio and atmospheric scale factors can be estimated as part of the orbit fit for robust data sets. If the RSO does not fall into this category, then a default model must be used.
4) The new precision orbit (computed around the time of interest) is to be used as a new starter for DYNAMO for one pass over the MSX data to be analyzed. Residuals and pass statistics are to be stored in the data base for quick access.

3.2 Radiometric Processing

The primary objectives for radiometric processing in the SDAC are as follows:

1) Augment RSO data bases in the UV, Visible, and IR,
2) Develop satellite specific models for satellite signature in the UV, Visible, and IR,
3) Develop regression tools for RSO signature models,
4) Understand the utility of radiometric data for surveillance, discrimination, status monitoring, and mission assessment.

Existing signature and environment modeling tools will be applied in the SDAC. These include: SIMAN (using the ELIAS workstation for stick-figure modeling of satellite body types), OSC, and SSGM. Atmospheric and environment modeling tools to be used include SHARC and LOWTRAN. In addition, IR and Visible signature data from ground-based sensors will be included in the data bases in the SDAC and used in RSO signature model development.

4 EXAMPLES

Several real-data examples of SDAC processing and analysis are provided in this section. The examples include ground- and space-based data. The first example involves data from the ETS site using an "SBV-like" visible configuration to demonstrate beginning-to-end processing of raw data in the SDAC. The output product in this case are calibrated metric data compared against a precision ephemeris from SSN metric data. The second example involves processing IRAS data. The IRAS orbit and viewing geometries are similar to those expected by the MSX (although the MSX will have the capability to observe low Earth orbits as well as deep space). The correlation problem is challenging, and if these data are any indication of the amount of RSO detections that will be seen by MSX sensors in less than 1 year's time, then the purpose of the SDAC becomes even more evident. The third example involves satellite-to-satellite tracking by medium-wave infrared sensors in geosynchronous orbit using "above-the-horizon" scans. These data are assessed for their metric quality. The last example compares radiometric data from a ground-based sensor to a model produced by SIMAN.

4.1 SBV Ground-Test Data from ETS

During SBV development at MIT Lincoln Laboratory, data on RSOs and backgrounds have been collected at the Experimental Test Site (ETS) in Socorro, New Mexico. These data were collected using "SBV-like" characteristics, including 6" aperture optics, a 420X420 CCD focal plane array, and similar sensitivity. Hundreds of data sets are available to be processed as a test of processing and other aspects of the SDAC. In order for metric observations to be reduced from the data, stars in the image data must be located, matched to an on-line catalogue, and used to refine the sensor pointing and attitude model.

This model must be inverted for each RSO detection, yielding right ascension and declination measurements at known times.

For the case of the MSX, an accurate ephemeris must be available at times associated with all data to be analyzed. The MSX spacecraft will not have a GPS receiver on board, but an S-band transponder is available to allow tracking data to be collected for this computation. Satellites with similar orbital characteristics to the MSX and a similar S-band transponder have been used to verify that this type of tracking data (collected by the CSTC S-band Ground-Link Stations) is adequate to produce a post-fit ephemeris for the spacecraft which is accurate to 15 meters or better. Of course, for the case of the ground-based ETS site, an accurate inertial ephemeris of the sensor is available for any time. Nevertheless, ephemeris data of this type can be used to demonstrate metric processing in the SDAC.

The chart in Figure 5 shows an SDAC end-to-end test (raw data to metric data quality assessment) for the ETS data. Shown in Figure 5 are the raw data, the attitude and pointing refinement, and the metric quality assessment. The detections are merged with the ephemeris data (shown is the RMS range error in meters, for a fit of a sample spacecraft orbit fit to S-band tracking data over a time interval) for the metric analysis. It is expected for SBV metric angle data to have an accuracy of 4 arcseconds or better, and this is displayed in the pass residuals "bulls-eye" chart in the bottom of Figure 5. This is an improvement over the SSN GEODSS sensors, which have a stated accuracy of 10 arcseconds (1 sigma).

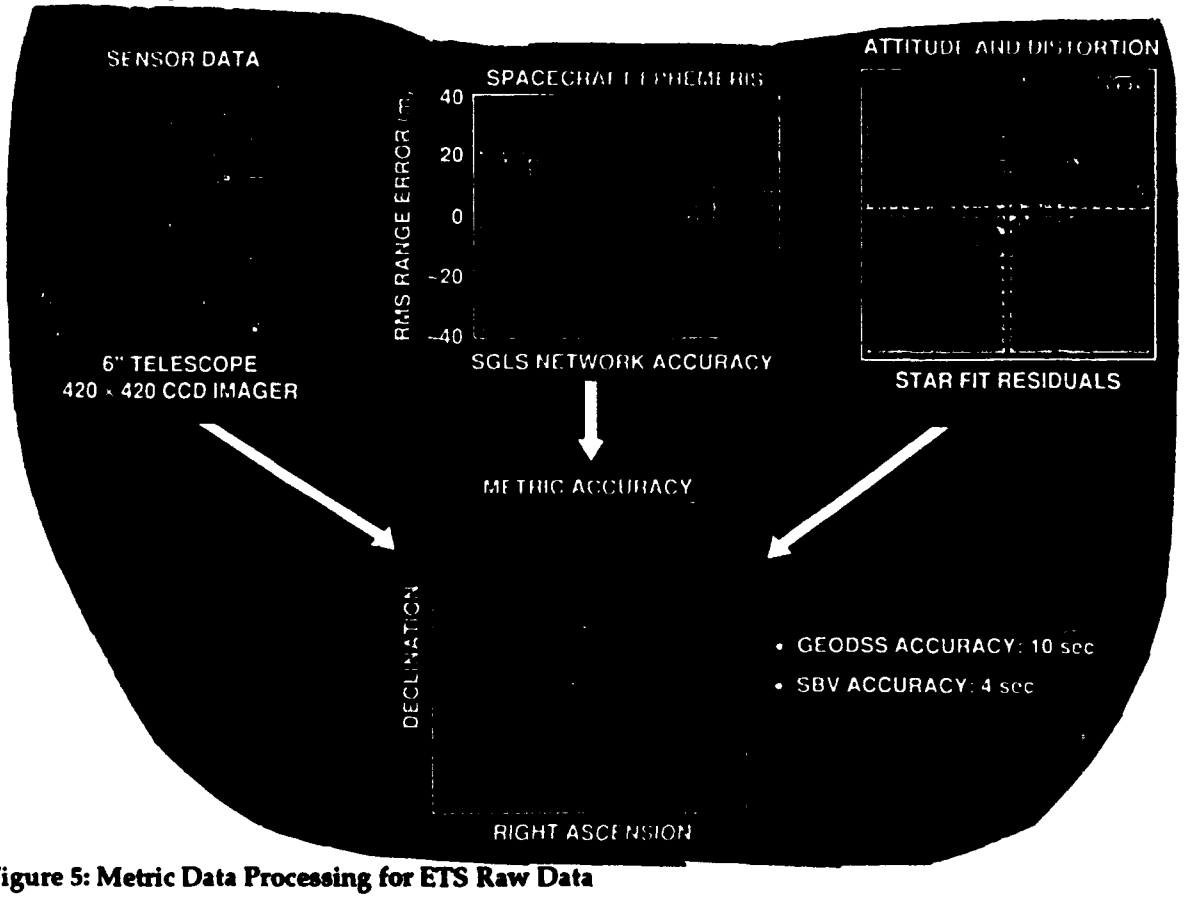

Figure 5: Metric Data Processing for ETS Raw Data

4.2 IRAS

The Infrared Astronomical Satellite (IRAS) had a 10-month lifetime in 1983, and data were collected from a focal plane which contained four long-wavelength infrared detectors: 12, 25, 60, and 100 microns. The sensitivity of SPIRIT III is expected to be similar to IRAS, and therefore the

radiometric data offers a good opportunity to prepare the SDAC for SPIRIT III data analysis. IRAS could detect a 1.5 meter object at a distance of 36000 km from the spacecraft. While the angle accuracy of IRAS is not tight ($\sigma \geq 30$ arcseconds), a large number of RSOs were detected, and these comprise a data base of detections of RSOs from a space-based sensor.

A picture of the IRAS focal plane and its orbital geometry is shown in Figure 6. Note that IRAS always pointed away from the Earth. Routine processing intentionally discards detections which only fell on one of the detectors in the focal plane. The number of detections left over with a signal-to-noise ratio of greater than 3.5 exceeded 200000.

It has been stated above that IRAS data provide a good opportunity for advancing the learning curve for understanding the utility of space-based infrared RSO data for signature analysis. In order to do this, known RSOs need to be separated out of the large number of detections in the IRAS data base. In order to perform this task, a first pass of "reasonable" detections were processed through the front end of the SDAC automatic metric processing (as shown in Figure 4). The processing involved the following steps:

1) Raw detections were transformed into right ascension and declination measurements by inverting the known pointing against the location of the focal plane detectors.
2) The ephemeris of the IRAS satellite for the entire 10 month period in 1983 was estimated. Positions of the spacecraft were merged with the observations data base produced in Step 1.
3) The deep space RSO catalogue for 1983 was gathered for automatic UCT processing.
4) The UCT processing was asked to correlate 136304 "reasonable" detections (those which were recorded in each of the 12, 25, and 60 micron detectors) against the 1000 object 1983 deep-space RSO catalogue. Results were tabulated for further processing.
5) High confidence correlations were tabulated with flux calculations for more detailed signature data modeling. This analysis is still not complete.

Results from Step 4 are provided in Table 1. Because of the loose metric error budget (components of this budget include errors in the IRAS ephemeris, 1983 RSO catalogue element sets, and IRAS detections), even correlations with residuals greater than 1 degree are of interest. Table 1 shows that out of the 136304 detections, nearly 10000 correlated to some RSO with residuals less than 4 degrees, and nearly 1/4 of those had residuals less than 1 degree.

Table 1: IRAS Detections UCT Processing Results (Against 1983 Deep Space Catalogue)

Number of IRAS Sightings used	----	136304
Number of Correlations with Residuals less than 4 degrees	----	9955
Number of Correlations with Residuals less than 1 degree	----	2469

4.3 Other Space-Based Data

IRAS is not the only satellite in orbit about the Earth capable of observing other RSOs. There are several satellites in geosynchronous orbit which contain medium-wave infrared sensors that can detect low altitude RSOs while employing an "above-the-horizon" scan. The geometry of such a scan is shown in Figure 7. Focal plane coordinates are referenced to the boresite line (which connects the center of mass of the sensor to the center of the Earth). Multiple detections of each observed RSO comprise a track as the low altitude RSO passes through the field of view. These can be easily correlated with the known RSO catalogue, and about 100 such tracks collected during 1991 were made available to the SDAC for testing and analysis. In this case, the metric error budget is somewhat better than for IRAS, and the data appear as an "inverted " SBV type. The tracks were used to test the SDAC metric processing for assessment of the quality of the data. Further radiometric processing of these detections has not been performed at this time.

Processing of the metric observations proceeded as follows:

1) A track of data is translated into right ascension and declination coordinates by rotating the focal plane detections with the boresite angles.
2) The ephemeris of the sensor is estimated using either provided quantities or else fit to skin tracking of the spacecraft. The latter method will be referred to as the "revised ephemeris".
3) Independent tracking data on the detected RSO are collected for metric processing as described in Section 3.1.
4) An initial orbit is calculated and a refined precision orbit is fit to the tracking data.
5) A pass of the refined orbit against the track of observations is performed and pass statistics from the residuals are calculated.

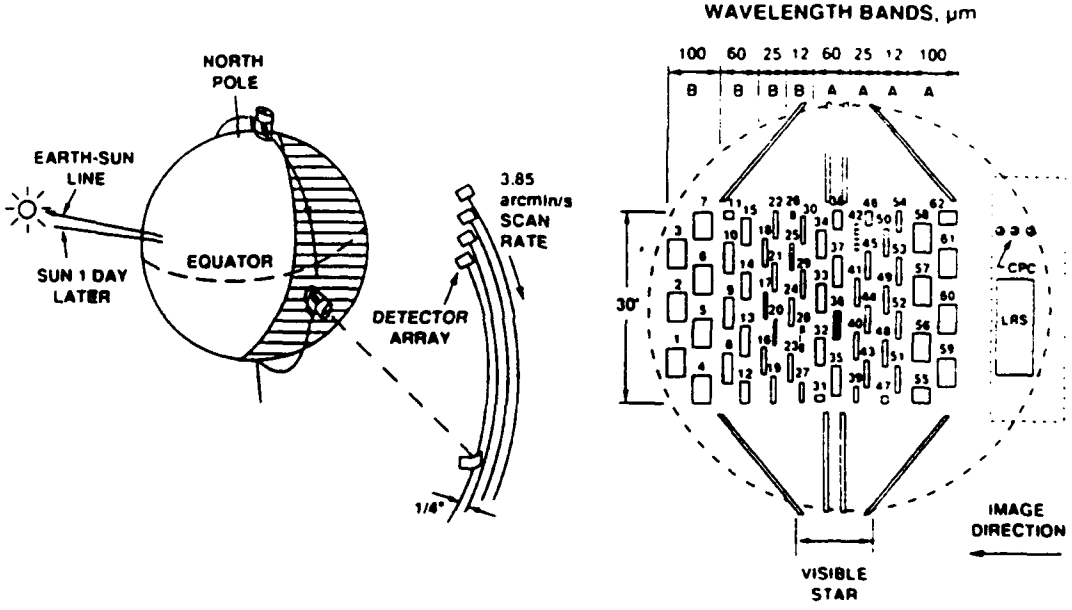

Figure 6: IRAS Orbit Geometry and Focal Plane Setup

Results from performing this processing on three distinct RSOs are presented in Table 2. The RSOs are MIR (16609), a Japanese payload (17480), and the European payload ERS-1 (21574). ERS-1 is of particular interest because this payload is equipped with laser cube corner reflectors and is heavily observed by the laser tracking network. This means that an orbit can be calculated for ERS-1 which is accurate to 1 meter or better. The difference in the results for the provided or revised ephemeris indicates that this part of the metric error budget is the least understood. This issue is still being investigated, but Table 2 shows that the metric accuracy of these space-based sensors is between 1 and 4 mdeg.

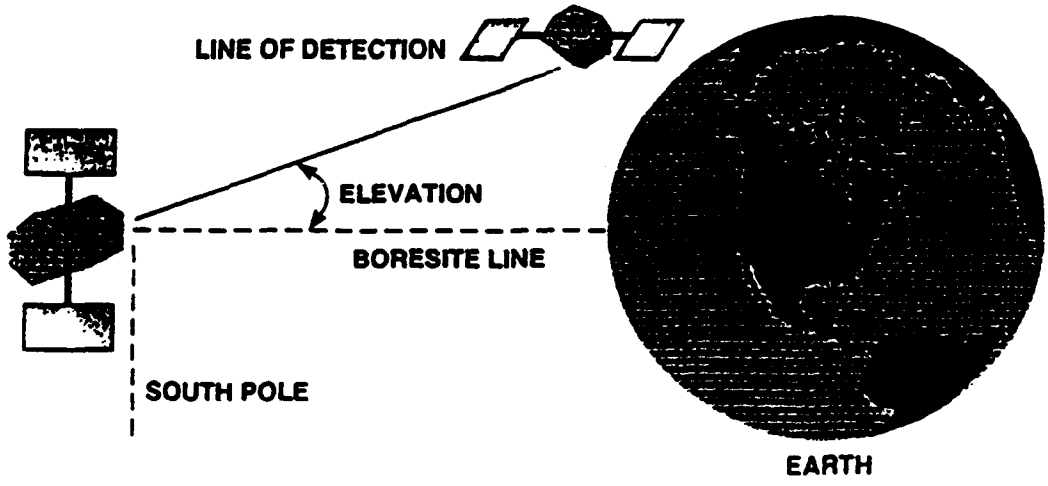

Figure 7: Geometry of a Sensor in Geosynchronous Orbit Performing an Above-the-Horizon Scan

Table 2: Satellite-to-Satellite Tracking Pass Statistics for Select RSOs

OBJECT	DATE	RIGHT ASCENSION		DECLINATION		#OBS	EPHEMERIS
		<>(mdeg)	σ(mdeg)	<>(mdeg)	σ(mdeg)		
16609	91036	0.63	1.71	-1.59	1.33	16	Revised
17480	91301	2.58	1.68	-2.23	1.77	14	Provided
21574	91284	-4.76	1.46	3.19	2.67	29	Provided
21574	91287	-4.58	2.57	6.58	2.26	16	Provided
21574	91292	-3.24	2.60	7.43	3.37	20	Provided
21574	91287	-4.64	2.56	2.61	2.29	16	Revised
21574	91292	-2.77	2.60	2.79	3.34	20	Revised

4.4 SIMAN Model Example

In late December of 1990 and early January of 1991, a team of Lincoln Laboratory scientists went to the ETS site to collect 3.5 - 5 micron data on specific RSOs for analyzing the signature modeling capability of SIMAN and other tools. The details of this work are provided in internal Lincoln Laboratory memoranda. The modeled signal of a ROSAT (SSC #20638) compared to the measured values from that work provides a good example of the type of radiometric analysis to be available in the SDAC.

The ELIAS [illegible]station modeled the body shape, sun angles, and shadowing for the ROSAT and SIMAN provided simulated temperature values for various parts of the spacecraft body over the tracking time interval. For this interval, the expected signal (in electrons) of the IR sensor was calculated (normalized to a range of 1000 km). The measurements were also normalized to this range value and the predicted signal plotted against the measured values are shown in Figure 8. One can see from this chart the quality of SIMAN's predictions (the error in the predicted signal versus the field data is 15% or less), but important ingredients to the model are critical for success. These ingredients include: physical model of the spacecraft body, thermal and optical properties, orbital elements or

THE U.S. SPACE SURVEILLANCE NETWORK'S TRACKING OF ARTIFICIAL SATELLITES ORBITING WITH HYPERBOLIC TRAJECTORIES

Scott W. Wacker, S.M. Hunt, M.J. Lewis
MIT Lincoln Laboratory

D.L. Harris
TRW, Inc.

ABSTRACT

During the last four years, the Space Surveillance Network (SSN) successfully tracked and determined orbital elements for five missions involving spacecraft orbiting with hyperbolic (earth-escape) trajectories: the Space Shuttle launches of Magellan (May 1989) and Galileo (October 1989), both Galileo earth flybys (December 1990 and 1992), and the Titan launch of Mars observer (September 1992). Since the propagation models at the Space Surveillance Center (SSC) and the SSN sensors are not designed to accommodate hyperbolic orbital elements (semi-major axis, $a < 0$, eccentricity, $e > 1$, these missions presented considerable challenges with regard to pre-mission planning, target acquisition and tracking, real-time orbit determination, and post-mission analysis. At the request of Space Command, the staff of MIT Lincoln Laboratory's Millstone Radar developed the necessary software to address these issues, leading to the SSN's success for these missions.

For both launch coverage and maintaining current orbital elements, the SSN regularly tracks satellites populating the semi-synchronous and geosynchronous orbital regimes. The aforementioned NASA interplanetary probes provided the SSN with opportunities to track satellites at altitudes well beyond geosynchronous orbit. For example, Millstone tracked Galileo in October 1989 to a range of 67,000 km. ALTAIR tracked Mars Observer to a distance of 80,200 km, and Galileo during its second earth flyby to a range of 113,100 km. Acquiring with ephemerides computed by Millstone, the GEODSS Test System (White Sands, NM) tracked Galileo in October 1989 to a distance of 94,000 km, while Diego Garcia GEODSS tracked Mars Observer to a range of 111,000 km.

Although not orbiting with a hyperbolic trajectory, the ISAS/NASA spacecraft Geotail ($e = 0.83$; period, $P = 17.24$ days) presented similar challenges. Also acquiring with Millstone pointing predictions, Maui GEODSS tracked Geotail during October 1992 to a distance of 221,650 km. This is among the most, if not the most remote skin-tracking data of an artificial space object.

In all cases, Space Command and Millstone received either nominal or telemetry-derived orbital elements from the Jet Propulsion Laboratory.

state vector, and site coordinates. A detailed model of the satellite body for this example was provided by the NASA Goddard Flight Center and by the German Space Operations Center.

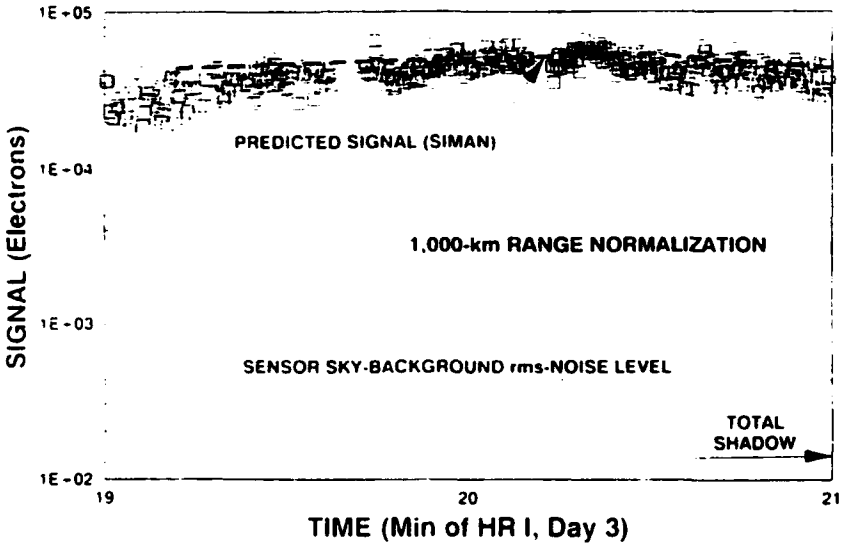

Figure 8: Range-Normalized Signal vs Time for ROSAT (Measured and Predicted)

5 SUMMARY

A data analysis center has been described in this report for support of the MSX Surveillance Principal Investigator Team. The SDAC is designed to analyze all metric and radiometric space surveillance data from the MSX spacecraft. In order to effectively perform this task, the SDAC must tap into data from the Space Surveillance Network and data merging and fusion techniques will be employed. Central to the SDAC development are metric and radiometric analysis tools. These will tie into data bases containing Earth, environmental, RSO, sensor, and spacecraft related data. In addition, the processing will augment the RSO data bases with information gathered from the UV, Visible, and IR sensor data collected on the MSX. Metric processing will be performed on a specially designed workstation for analyst interaction, and an automatic metric process has been described which will insure that at least one pass over all SBV and SPIRIT III data is performed. Radiometric analysis tools are also included in the SDAC design, and it is hoped that the MSX will provide a key opportunity to study the utility of space-based signature data for space surveillance. Finally, examples have been provided which demonstrate the type of processing to be performed and the ease with which large quantities of data can be analyzed.

LAGEOS-2 Launch Support Navigation at JPL

T.P. McElrath, G.D. Lewis (Jet Propulsion Laboratory/Caltech), K.E. Criddle (Sterling Software)

Introduction:

LAGEOS-2 (LAser GEOdynamics Satellite-2), deployed during the flight of STS-52 in October 1992, is the follow-on to the successful LAGEOS-1, which was launched by NASA in 1976. The Agenzia Spaziale Italiana (ASI) decided to build a second identical satellite in the mid-1980s and NASA agreed to launch it on a space shuttle mission and provide several other services as a cooperative mission.

LAGEOS-2 is a passive spacecraft whose sole purpose is to allow precise satellite geodesy though the use of accurate satellite laser ranging. The spacecraft is a sphere covered with 426 equally-spaced laser cube corner reflectors. The spacecraft mass is 405.38 kilograms, mainly due to a large brass core, and the diameter of the spacecraft is only 60 centimeters. The resulting high density of the spacecraft reduces the sensitivity of the orbit to non-gravitational accelerations. The combined tracking of LAGEOS-1 and LAGEOS-2 will allow much more accurate determination of geodetic quantities than would be obtainable from just LAGEOS-1.

The orbit of LAGEOS-2 is similar to that of LAGEOS-1 in that it is nearly circular at an altitude of 5900 kilometers. However, the inclination of LAGEOS-2 is 52 degrees, compared to 110 degrees for LAGEOS-1, to allow measurements of a different set of geodetic quantities to be made. To reach its final altitude and inclination after being released from the shuttle in a standard 28.5 degree inclination orbit, LAGEOS-2 was mated with two upper stages, both using solid rockets. The first stage was a completely new Italian design named the Italian Research Interim Stage (IRIS), which had not flown before, while the second, the LAGEOS Apogee Stage (LAS), employed a motor that had flown previously. The IRIS firing put LAS/LAGEOS-2 into a 300 x 5900 kilometer altitude orbit inclined 41 degrees. The LAS firing circularized the orbit at apogee and provided the final inclination change. Figure 1 shows a schematic of the various orbits as well as the magnitudes of each motor burn.

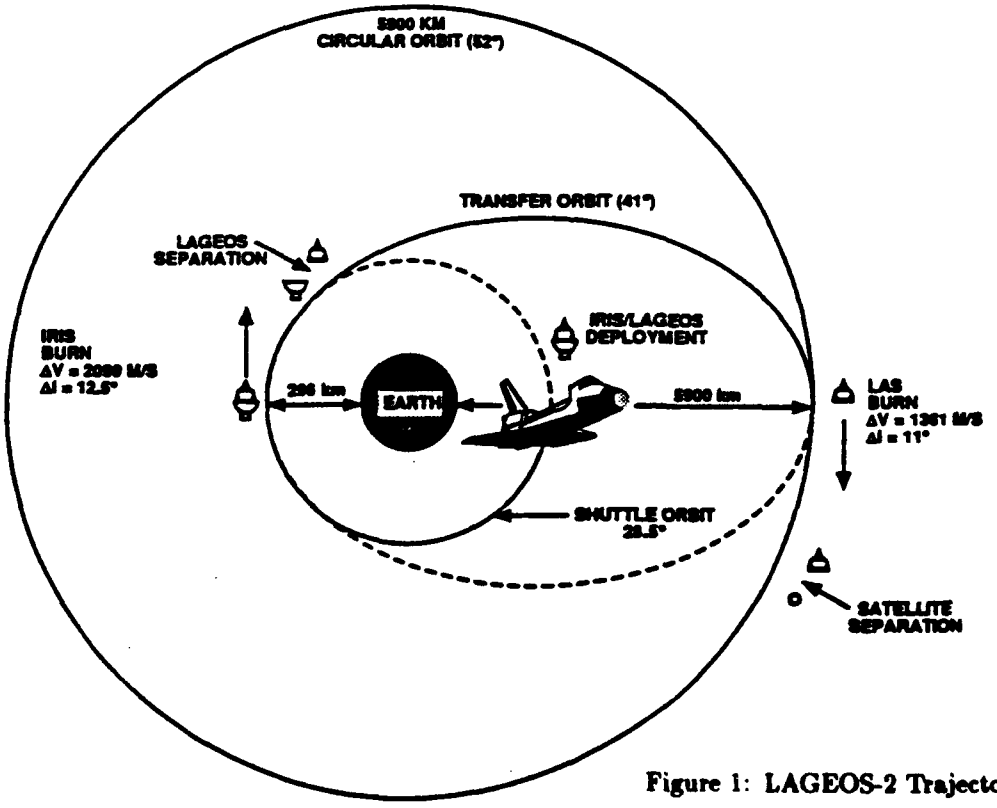

Figure 1: LAGEOS-2 Trajectory Overview

While LAGEOS-2 has no radio transmitter, both upper stages transmitted telemetry until well after their respective burns. ASI had a requirement to capture the telemetry from both stages to assess the motor performance, especially important for the new IRIS stage. In addition, the LAS transmitter changes to a beacon mode ten minutes after the LAS burn, and tracking of the LAS beacon was to be the initial information used to assist in LAGEOS-2 acquisition by the laser ranging network (before the two objects drifted too far apart), a fairly difficult task due to the small laser beamwidth and the need for a small *a priori* range error.

In the process of meeting this set of requirements, the operational plan developed into a cooperative effort by five organizations including JPL. The operational activities of each organization from the perspective of the Multimission Navigation Group (MMNAV) of the JPL Navigation Systems Section, are summarized in Figure 2, and described below. ASI was responsible for providing MMNAV the maneuver model parameters for both the IRIS and LAS burns, and for supporting MMNAV testing to make sure that the maneuver integration was being done correctly. The Johnson Spaceflight Center (JSC) Flight Dynamics Officer (FDO) console was responsible for sending shuttle state vectors and LAGEOS-2 post-deployment state vectors to MMNAV around the time of the deployment. The required STS target attitude at deployment was determined by the ASI operations team at JSC, and the predicted or actual shuttle attitudes were forwarded to MMNAV by JSC/FDO. The ASI team also received and processed all the telemetry from the two upper stages.

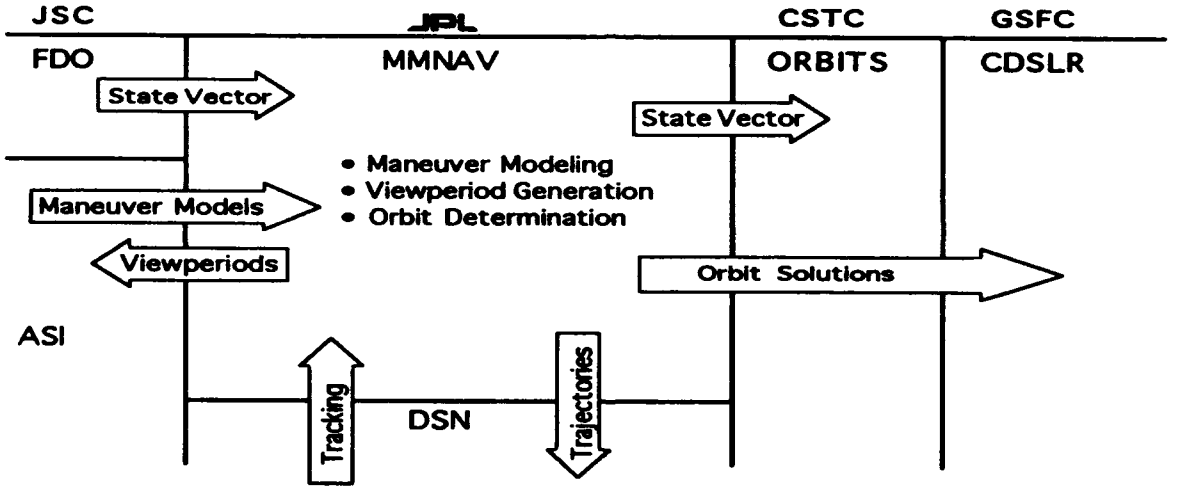

Figure 2: Overview of MMNAV Functions and Interfaces

The requirement to capture the telemetry and track the LAS beacon involved three different tracking networks. 1.) The European Space Agency tracking station at Malindi in East Africa was the first ground station to receive telemetry after deployment, and covered the IRIS burn. 2.) The Air Force Satellite Control Network (AFSCN) Indian Ocean and Diego Garcia Stations also covered the IRIS burn, and the AFSCN station in Hawaii covered the LAS burn. This activity was coordinated by the Consolidated Satellite Test Center (CSTC) at Onizuka Air Force Base. 3.) The NASA/JPL Deep Space Network (DSN) 26 meter station at Goldstone, California also covered the LAS burn, and the 26 meter stations at the other two DSN sites, at Madrid, Spain, and Canberra, Australia, covered the beacon phase of the LAS orbit and (for Canberra) the transfer orbit. MMNAV was required to provide CSTC with a nominal post-IRIS burn and post-LAS burn state vector based on either the JSC state vectors or DSN tracking and the ASI maneuver models. MMNAV sent station viewperiod information to ASI at JSC, and provided updated trajectories to the DSN for antenna pointing predictions. Once DSN radiometric tracking data was available, MMNAV determined the LAS orbit as quickly as possible (for reasons described later) and sent predicted LAGEOS-2 state vectors to the Goddard Space Flight Center (GSFC) Crustal Dynamics Satellite Laser Ranging (CDSLR) Network headquarters, located at GSFC, to assist in their stations' acquisition of LAGEOS-2.

In the months leading up to the launch of STS-52 with LAGEOS-2 aboard in October, 1992, a variety

of tests were performed to verify that this operations plan was ready. The verification of the IRIS and LAS maneuver models required a significant amount of interaction between MMNAV and ASI (fortunately mostly by electronic mail). The state vector transfers to and from JPL used three different electronic transmission interfaces, all of which required some effort to bring to a state of routine success. Most of the activities supporting the actual mission were brought together and tested in three Joint Integrated Simulations (JISs) organized and run by JSC. Internal tests at JPL were also organized to test the ability of MMNAV personnel and computer systems to process the DSN tracking data and determine the orbit of the LAS spacecraft, which involved several unusual aspects as compared to other MMNAV launch support activity.

Pre-launch covariance study:

While no specific accuracy requirements were ever levied on the LAGEOS-2 state vectors to be sent by MMNAV to CDSLR, an obvious implied requirement lies in their ability to give some reasonable probability that the satellite laser ranging (SLR) stations could acquire LAGEOS-2. Because LAS had no two-way transponder (unusual for DSN-supported missions), the data types available consisted of one-way Doppler and angle measurements. The one-way Doppler was regarded as useless due to the poor stability of the LAS oscillator, so only angle data was relied on in operational orbit determination. Previous experience had shown that DSN angle data from the 26 meter subnet could be used with an assumed 1σ accuracy of $0.02°$, along with a $0.05°$ angle bias per station per pass. LAGEOS-2 was of course completely invisible to the radio frequency systems of the DSN, so LAGEOS-2 state vectors had to be based on LAS tracking data.

Before launch a covariance study was performed to identify the expected errors in the LAGEOS-2 orbit solutions. To obtain this information, data was simulated along the nominal trajectory of the LAS spacecraft, starting at the Canberra pass during the transfer orbit. The data was then processed in a manner similar to actual operations using least-squares parameter estimation based on linearized perturbations around the nominal trajectory. The spacecraft state at epoch, apogee motor burn, and separation ΔV parameters were estimated, along with station angle biases for each pass. The early results were fairly dependent on the *a priori* uncertainty for each parameter, so a detailed model of each parameter, including the correlations with other parameters, was developed. While the IRIS burn and shuttle state uncertainty were included initially, earlier studies provided an approximate *a priori* diagonal state covariance at an epoch after the IRIS burn, which produced a significant simplification. The estimated parameters and their assumed *a priori* 1σ uncertainties are shown in Table 1.

Table 1: Estimated Parameters and *A Priori* Uncertainties (1σ)

Parameter	Uncertainty
Spacecraft position components	10 km
Spacecraft velocity components	20 m/sec
DSN angle measurement biases (1/station/pass)	.05 degrees
LAS apogee burn:	
pointing	1 degree
start time	0.75 seconds
thrust	2 % of nominal
duration	2 % of nominal
impulse (through thrust and duration correlation)	0.23 % of nominal
LAS separation maneuvers:	
LAS spin axis error	1 degree
LAGEOS-2 separation ΔV	10 % of nominal
Yo-Mass separation ΔV ($\perp$ to spin axis)	9 cm/sec

One complicating factor was the two separation maneuvers that occurred early in the data arc. The LAS/LAGEOS-2 separation had a well defined direction along the spacecraft spin axis, although the large

magnitude of the separation ΔV (1.2 m/sec) meant that even a 10 percent error could grow quickly. However, 4 seconds after LAGEOS-2 separation, a "Yo-Mass", described as a 2.85 kilogram mass on the end of a long wire wrapped around LAS, separated, in a direction perpendicular to the spin axis with an *a priori* magnitude of 9 cm/sec. In consideration of both these events, it seemed likely that the uncertainty of the MMNAV solutions for LAGEOS-2 would reach a minimum within a few hours after separation, and then grow linearly in position uncertainty as the unknown separation impulses overcame the improvement in the LAS state estimate based on continued tracking data.

The covariance for the LAS orbit also had to be mapped through the LAGEOS-2 separation and along the LAGEOS-2 trajectory to provide a useful covariance at the times that SLR stations would be trying to acquire. This turned out to be quite complicated, as the state covariance just before the LAS/LAGEOS-2 separation depends on the separation impulse uncertainty if there is any tracking data following the separation (which was the case for most of the MMNAV solutions). While the state at the end of such a data arc may be well determined, the presence of two maneuvers between the bulk of the data and a pre-separation epoch degrade the estimate of the pre-separation state, and introduce correlations between the state and the separation ΔV. The separation impulse had a smaller effect on the LAGEOS-2 trajectory due to the larger mass of LAGEOS-2 (2.5 times more massive than LAS after motor burnout) but it still had to be included to obtain accurate results.

In addition to the pre-launch covariance study, a post-mission covariance study was performed using the actual tracking data and solutions that were obtained operationally. While the results of the two studies were similar, the post-mission study is the most definitive theoretical measure of the state uncertainty for the operational LAGEOS-2 orbit solutions, and so all the results reported here are from the post-mission study.

Table 2: Predicted RSS Position Uncertainty (1σ) for LAGEOS-2 (in km)

Mapping Epoch	Solution Number 2	3	3A	4	5	6	7
17:00	*86.87*	6.62	2.00	0.97	0.93	0.83	0.78
17:30	*129.46*	*17.75*	2.59	1.41	1.37	1.29	1.25
18:10	*166.20*	*42.71*	*6.07*	2.57	2.48	2.36	2.30
18:50		*65.71*	*10.65*	*3.65*	3.32	3.17	3.10
20:00			*14.24*	*4.44*	*3.48*	3.23	3.13
21:30				*5.55*	*4.85*	*4.65*	4.55
22:30					*6.63*	*6.32*	*6.20*

Mapping epochs given in hours and minutes (UTC) on 10/23/92
Position uncertainties after the data arc are in *italics*

The predicted position uncertainties for six MMNAV orbit solutions (starting with the first one after the LAS burn) are given in Table 2. The epochs on the leftmost column correspond to the times when a new solution would have been available to SLR stations. This time is typically 50 minutes after the last data point, split roughly equally between MMNAV processing and CDSLR processing and distribution. Each solution is mapped to the same epochs as all preceding solutions and also to the epochs of the two following solutions (except for the last two solutions listed). Starting from the time each solution was available at SLR stations, the results are given in italics. The most significant value for each solution is the first italic entry in each column, which when compared between different solutions indicates that the smallest uncertainty on any solution at the time of its delivery was Solution 5, and that the uncertainty of all subsequent solutions actually deteriorates due to the effects described in the preceding paragraph.

The actual capabilities of the SLR stations were not formally defined, but the consensus from CDSLR headquarters was that the effective beamwidth at the LAGEOS-2 altitude was 300 meters, and that the

allowable range error (or "range gate") varied from 2 to 10 kilometers depending on day or night operation, respectively. These numbers do not include the possibility that station personnel would try search procedures to effectively increase the acquisition beamwidth, but such measures would not be expected to increase these numbers by more than a factor of five in all directions during a typical pass duration of 30 to 45 minutes. It is also apparent that the range direction is more forgiving than the angular directions, which raises the question of the orientation of the covariance in the orbit plane.

One useful reference frame available to display the covariance is the Radial, Transverse, Normal (RTN) system (also known as the Radial, Downtrack, Out-of-plane system), where one axis is aligned with the position vector, the second axis lies in the orbit plane in the direction of motion, and the third axis is aligned with the angular momentum vector of the orbit. The error ellipses representing the covariance of four successive solutions (starting with Solution 3) at the time of their availability at SLR stations are plotted in Figure 3 for each combination of two directions. In the Radial-Downtrack plane the dominant feature is the correlation linking "early and low" with "late and high" in the first two solutions, which changes to an almost pure downtrack error by the last solution, while the other two plots do not show significant correlations between the two directions. While the error ellipses of the later solutions are not shown, almost all of the error is in the downtrack direction. The knowledge of this orientation of the uncertainty would allow most of the laser ranging station searches to be conducted by using a time offset,

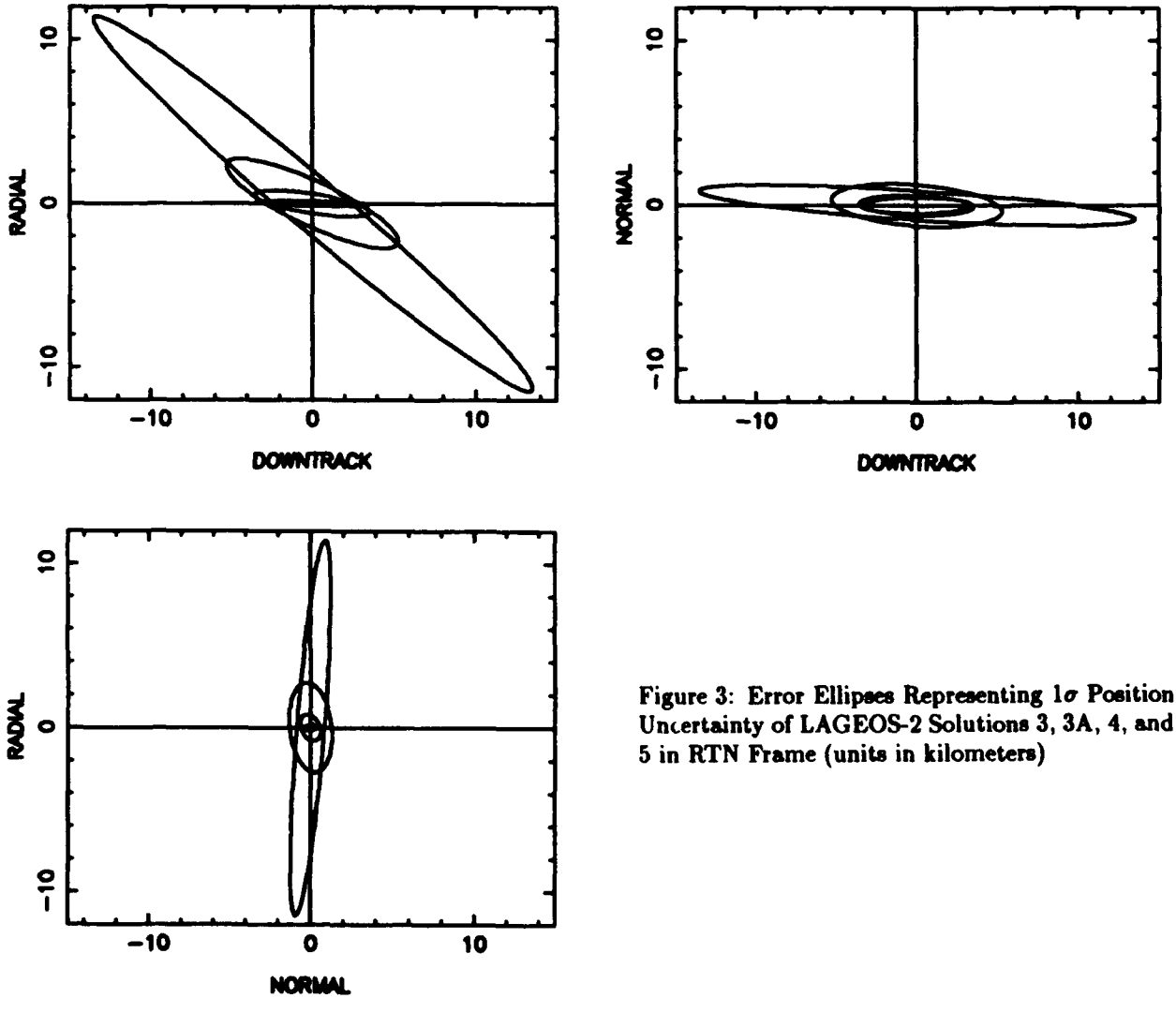

Figure 3: Error Ellipses Representing 1σ Position Uncertainty of LAGEOS-2 Solutions 3, 3A, 4, and 5 in RTN Frame (units in kilometers)

and also suggests that the larger range gate values would give a good chance of acquisition at spacecraft rise, when most of the downtrack error maps into station range. Even so, it is apparent that MMNAV solutions could not guarantee LAGEOS-2 laser acquisition, giving perhaps only a 50 percent chance of acquisition based on this study. However, this was acceptable under the rather unusual circumstances of operating purely on a "best efforts" basis. The actual course of events during MMNAV's operational support of the LAGEOS-2 mission is described below, and shows that the actual results were not quite as predicted by the pre- or post-flight covariance studies.

Operational results:

The liftoff of Columbia on STS-52 occurred almost 2 hours into the launch window on October 22, 1992. As the LAGEOS-2 deployment was not scheduled to occur until the end of the 14th shuttle orbit, most of the activity on the day of launch was confined to updating trajectories, timelines, and schedules based on the actual liftoff time. Two state vectors were received from JSC on the day of liftoff, and all the voice circuits involving MMNAV were verified.

The first of two pre-deployment state vectors from JSC arrived at 10:43 UTC on October 23 (3:43 am local time), and the second one arrived at 12:17. All of the state vector and trajectory products described above were prepared and sent within 20 minutes of each state vector's arrival in preparation for LAGEOS-2 deployment at 13:57. The deployment occurred as scheduled, and within 24 minutes the actual LAGEOS-2 deployment state vector and attitude arrived. This new state vector was almost identical with the last predicted state vector, but the actual attitude differed from the predicted attitude by about 0.1 degrees, so the trajectory was integrated again.

During this time, video images from STS-52 were available that showed the LAGEOS-2 stack receding from the shuttle. The IRIS firing at 14:42 was supposed to be visible as well, but no evidence of it was seen on the television screen. However, ASI personnel at JSC called out the beginning and end of the IRIS burn as seen in the telemetry captured at IOS. The IRIS/LAS separation was also confirmed in the telemetry.

Figure 4: LAS DSN Viewperiods. △ marks end of data arc for each solution.

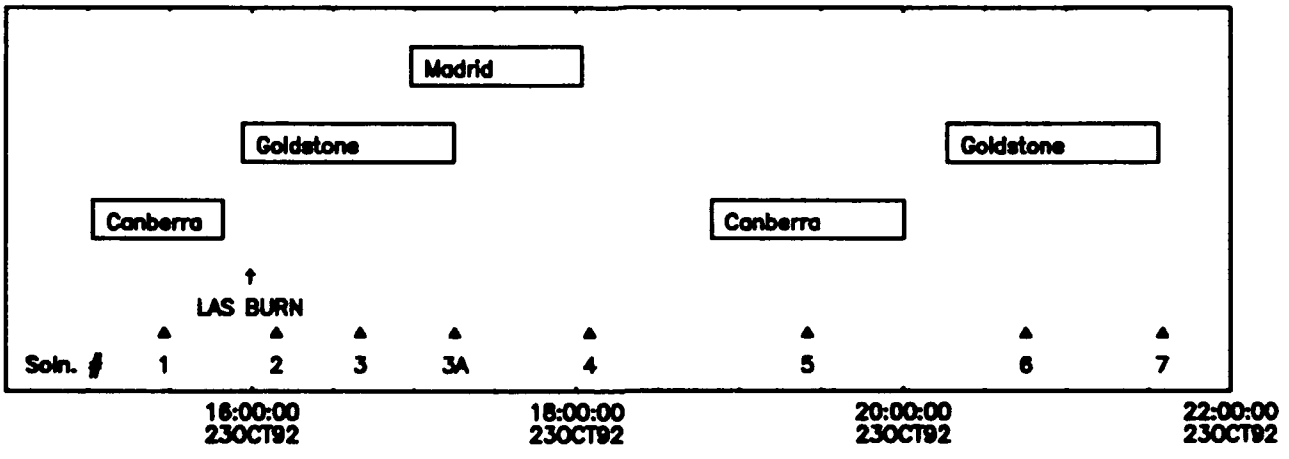

The viewperiods of the first 5 DSN passes (starting with the transfer orbit) are shown in Figure 4. The first DSN station to see LAS/LAGEOS-2 was at Canberra, where a 48 minute pass started at 15:01. While some of the early tracking data was lost due to communications failures, the station acquired on time, and a quick solution based on 18 minutes of angle data was performed. The first solution indicated that the IRIS burn had produced an orbit with an inclination and apogee height both slightly larger than planned. Quick updates were passed to the DSN stations in case of acquisition difficulties, and the first so-

lution was sent to CDSLR Headquarters. The rest of the Canberra data was available just before the LAS burn at 15:59, and was processed while waiting for post-LAS burn data.

The LAS burn and separation were also seen and described by ASI personnel from the telemetry data flowing from the CSTC station in Hawaii and the DSN station at Goldstone. In addition, a small telescope at the SLR station in Hawaii was able to observe the LAS burn, even though the dawn lighting conditions prevented more capable optics from being used, which might have steered the laser ranging system onto LAGEOS-2 from the moment it separated from LAS. This change in lighting conditions, which subsequently caused difficulties for SLR stations over North America, was probably the largest operational effect of the shuttle launch delay.

The Goldstone pass, which began 3 minutes before the LAS burn, lasted one hour and twenty minutes, but the first solution adding Goldstone data (Solution 2) was obtained from the first nine minutes of angle data following the LAS burn. This solution was sent to CDSLR because, even though the orbit uncertainty was still large, the *a priori* uncertainty of the LAS burn, and hence the subsequent state uncertainty, was significantly reduced.

The next solution (Solution 3) was obtained by adding 31 minutes of Goldstone data, and it was determined that the pointing for the LAS burn was at least three degrees from nominal (a 3σ error). The last 35 minutes of Goldstone data arrived with the first 16 minutes of Madrid data, and the resulting solution was used to update the DSN station pointing predictions. While this solution was not scheduled to be sent to CDSLR, it was in fact sent at their request, thus becoming Solution 3A.

The end of the 63 minute Madrid pass came at 18:02, with the next rise at Canberra still 47 minutes away. The solution obtained with this data (Solution 4) seemed to show that the LAS orbit was starting to converge, although changes of about 25 kilometers were still seen. Solution 4 was also sent to CDSLR with some hope, because although no SLR station had successfully acquired LAGEOS-2 to this point, the prelaunch covariance study indicated that there was a reasonable chance that one of the two Australian SLR stations would be able to use this state vector to do so. The angle residuals from this solution, combining the first passes from Canberra, Goldstone, and Madrid, are shown in Figures 5a and 5b. (The DSN 26-meter angle coordinate system consists of the primary "X" axis rotating about the local East-West line, and the secondary "Y" axis rotating about an axis perpendicular to the X axis. Both angles are at zero when the antenna is pointing at zenith.) While the angle residuals all lie within the assumed accuracy of 0.02°, it is evident that there are still unmodelled effects causing trends in the data. The quality of this angle fit is somewhat worse than that usually obtained (although perhaps not significantly so), the reason for which remains to be explained.

Figure 5a: LAS DSN X-Angle Residuals

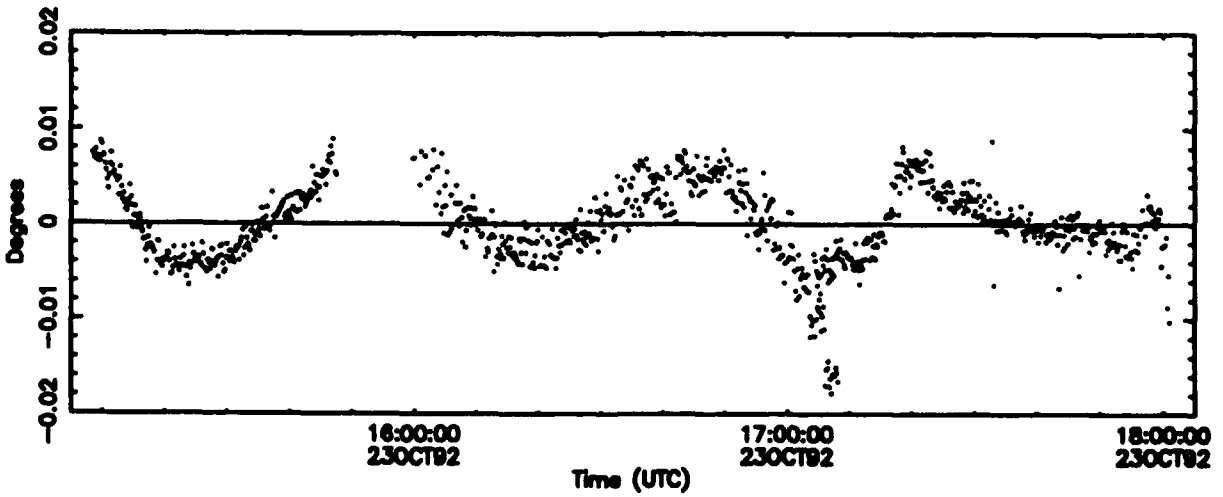

Figure 5b: LAS DSN Y-Angle Residuals

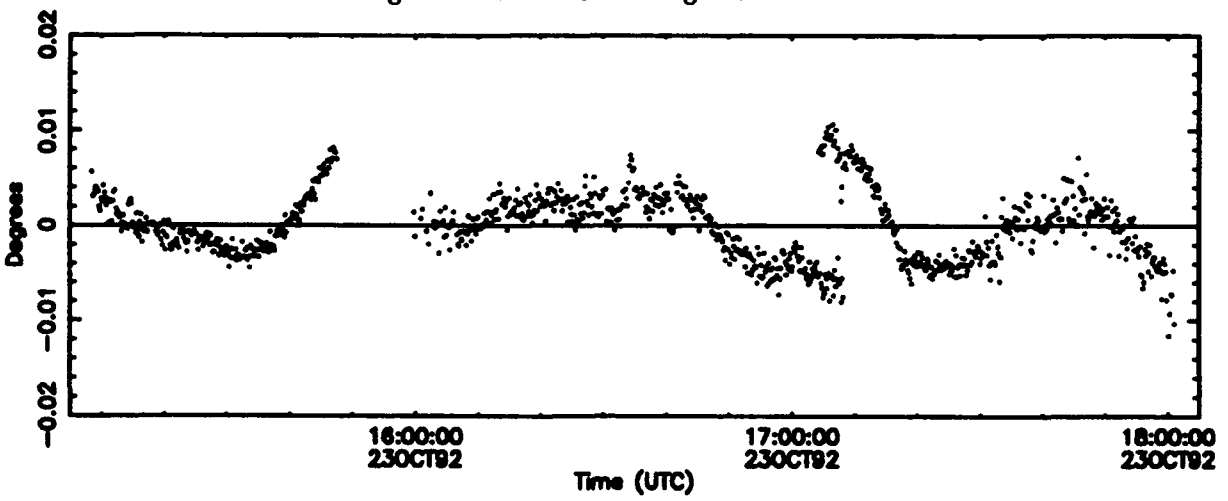

The 16 minute overlap between Goldstone and Madrid provided the opportunity to attempt to use differenced one-way Doppler collected at each site. By differencing one-way Doppler data, the effects of the LAS oscillator instability are largely removed. The prelaunch covariance study had shown that useful velocity information could be obtained by using this data. However, when the Madrid one-way Doppler data was processed it quickly became apparent that none of the Madrid Doppler data was any good, which was quite disappointing, as this opportunity only arises about once per day due to the altitude and inclination of the LAS orbit.

Solution 4 also became the basis of a preliminary report on the final orbit to the ASI team at JSC. While not supported by any SLR data, the MMNAV orbit was sufficiently accurate to determine that the eccentricity, period, and inclination of the LAGEOS-2 orbit met the ASI requirements for each parameter, even though some of the differences from the target values were unexpectedly large.

The second Canberra rise at 18:50 started a 70 minute pass, followed 16 minutes after its end by another 77 minute pass at Goldstone. During this time four more solutions were performed, three of which (Solutions 5, 6, and 7) were sent to CDSLR. None of the SLR stations in Australia, Hawaii, or the West Coast of North America were able to acquire LAGEOS-2 using these orbit solutions. In the case of the westernmost Australian station, heavy cloud cover prevented any attempt at acquisition. Subsequent solutions during this time showed consistency to better than 5 kilometers, indicating that the LAS trajectory was relatively well known, and would be not be significantly improved by additional data.

The orbit of LAS was such that at this point no DSN station was in view until Goldstone rose again 3 hours later. Consequently a rather relaxed shift change was performed between MMNAV personnel working on orbit determination. At this point considerable attention was given to the efforts of U.S. Space Command, as it was evident that they had the only remaining chance of aiding CDSLR in acquiring LAGEOS-2. MMNAV provided a state vector for LAS to be passed on to U.S. Space Command to aid in discriminating between the three objects in similar orbits, but it is not known if it was actually used. The first element set (or LSET) provided by Space Command had an unreasonably large position difference from MMNAV solutions (about 400 kilometers), but this was not unexpected due to the no doubt limited number of observations. Subsequent LSETs were more reasonable, however, and CDSLR started using them at about 04:00 on October 24, about 12 hours after the LAS burn.

The first optical acquisition of LAGEOS-2 came from the SLR station in Hawaii at 04:30, reporting a time offset of several seconds. Several unsuccessful acquisition attempts followed, but two LSETs later the western Australian SLR station acquired LAGEOS-2 with its laser system, at 09:00 on October 24. In the next 8 hours numerous SLR acquisitions were achieved, and a CDSLR orbit produced by 17:00 on October 24 had no detectable time bias. This essentially ended the launch support phase of LAGEOS-2 at both MMNAV and CDSLR. Three more MMNAV orbit solutions were provided to CDSLR during this period,

but no more were required after October 24, 17:00 (10 am PDT).

Post-mission analysis:

Once the orbit of LAGEOS-2 was well-determined from SLR data, it was possible to compare the JPL solutions to the CDSLR state vector received in the week following launch. The CDSLR orbit may be regarded as perfect due to the centimeter-level accuracy of the SLR data. Table 3 shows the difference between the JPL LAGEOS-2 trajectories and the CDSLR LAGEOS-2 trajectory (produced by numerically integrating the CDSLR state vector for a few hours) in terms of RTN position differences, given at the epoch when the solution would have been available at SLR stations (as in Table 2). While the rapid drop in the error from Solution 2 to Solution 3A is as expected, the growing downtrack error (due to a period error) that starts in Solution 4 is not predicted (except perhaps qualitatively) in any covariance study. From Table 3 it is readily apparent that only Solution 3A had any reasonable chance of aiding SLR acquisition. The relatively small position error of Solution 3A must also be regarded as somewhat accidental, as the period error in this solution was still 6 seconds. The search for the source of the unexpectedly large state error in the JPL solutions comprises the remainder of this paper.

Table 3: RTN position differences between MMNAV and CDSLR solutions for LAGEOS-2 (given at time of solution availability at SLR stations)

Solution	Radial(km)	Downtrack(km)	Normal(km)
2	-9.7	122.3	-12.2
3	9.0	-18.0	-3.6
3A	-6.4	-0.9	2.2
4	2.5	-25.3	0.8
5	0.5	-30.2	0.8
6	4.8	-35.6	-1.0
7	2.3	-45.2	-0.8

While many factors could contribute to the large LAGEOS-2 state errors, the most likely ones center around the separation impulses of LAGEOS-2 and the Yo-Mass, due to their almost complete unobservability in the DSN angle data. There are three sources of additional information on the separation impulses: the CDSLR LAGEOS-2 state vector, the DSN one-way Doppler data, and the Space Command radar data.

The Space Command data is probably the most useful, but it was not yet available to MMNAV at the time this paper was being written (although the authors expect to receive it in the future). Nevertheless, an attempt was made to use the Space Command data indirectly by drawing some conclusions from the Space Command LSETs on each object. While this led to several interesting developments, including an accurate method of converting SGP4-propagated LSETs to an equivalent numerically-integrated trajectory, the authors soon reached the conclusion that the LSETs available did not have the accuracy required to estimate the separation ΔVs. (This is not unexpected, especially as MMNAV did not request any special effort from Space Command on LAS and the Yo-Mass.)

Although the one-way Doppler data collected by the DSN served no useful purpose during actual operations, post-mission analysis of Doppler residuals shows some interesting features. Figure 6a and 6b show Doppler residuals during part of the first Goldstone pass, to which a polynomial has been fit to reduce the effects of spacecraft oscillator instabilities. (All of the features mentioned here are marked with arrows in Figure 6a and 6b.) The large feature at the beginning of Figure 6a is the LAS burn, which indicates a different velocity profile from the constant thrust that was modelled. The LAS-LAGEOS-2 separation can be seen at 16:05:30, and the end of the LAS telemetry at 16:10 also has a definite effect on the residuals. However, one additional frequency (and hence velocity) discontinuity shows up in Figure 6b at 16:32, with an equivalent line-of-sight velocity magnitude of 70 cm/sec. While all of these features may simply be due to the LAS oscillator, there were no discontinuities such as these observed in the Doppler data after this

time. This leads to the suspicion that the LAS suffered either a partial breakup or a collision, possibly with the Yo-Mass, at 16:32.

Figure 6a: LAS DSN Doppler Residuals

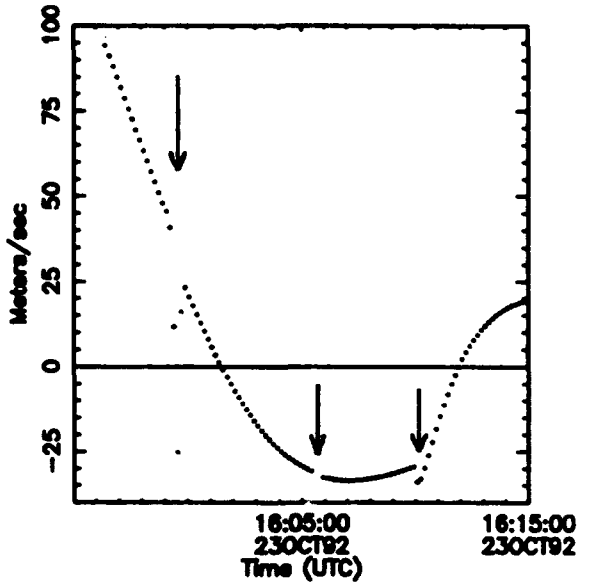

Figure 6b: LAS DSN Doppler Residuals

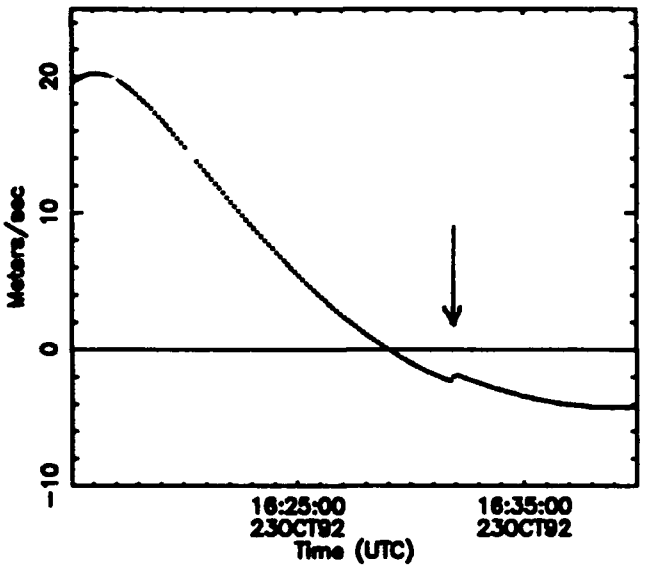

The Doppler data from a few minutes around both the LAS/LAGEOS-2 separation and the discontinuity at 16:32 were included in the angle data solution. For each segment of Doppler data, a fifth order polynomial bias model was estimated to account for oscillator instability, which had the effect of only allowing the Doppler data to determine the magnitude of the velocity discontinuity in the line-of-sight direction. The assumed accuracy of the Doppler data was 1 cm/sec after the bias model was included, and the RMS of the Doppler residuals was slightly smaller than the assumed accuracy. The combination of angle and Doppler data still did not have a strong sensitivity to maneuvers of about 1 meter/second magnitude at the epochs above, but a consistent combined solution was obtained that indicated that the LAS/LAGEOS-2 separation ΔV was roughly perpendicular to the nominal direction, and that the possible maneuver at 16:32 had a statistically non-zero magnitude. These results are somewhat tempered by their extreme sensitivity to the *a priori* uncertainty assigned to each maneuver, and so can only be taken as an approximate indication that the nominal separation maneuver models are not correct.

The last piece of information available was the CDSLR LAGEOS-2 state vector. A procedure was developed that allowed the state vector to be treated as an observation following the LAS/LAGEOS-2 separation maneuver (as it applied to LAGEOS-2) and then combined with the Doppler and angle data from the LAS trajectory in a consistent manner. Two solutions were performed in this manner - one using the nominal LAS/LAGEOS-2 separation time and the other assuming that the separation had actually occurred at 16:32 for some unknown reason. The results, measured primarily by the quality of the angle and Doppler data residuals, were much better when the nominal separation time was used. However, even in the nominal case a statistically non-zero ΔV resulted at 16:32, and the separation ΔV at the nominal time was not very close to the original model. For further comparison, a solution using only the CDSLR state vector and angle data (ie. without the Doppler data) was obtained for the nominal case. While the results for the maneuvers were qualitatively similar to those from the full data set, the estimates were not statistically consistent, which implies that the assumed data accuracies are too small and/or that there are still modelling errors. However, it seems safe to state that the LAS-LAGEOS-2 separation ΔV probably was not within the *a priori* uncertainty of 10 percent, and that there probably was an unplanned perturbation of the LAS trajectory at 16:32. These conclusions are enough to account for the differences between MM-NAV and CDSLR solutions for LAGEOS-2, although there may be additional factors involved.

Conclusion:

The LAGEOS-2 deployment and injection into its operational orbit was successfully supported by MMNAV. MMNAV was not able to assist the CDSLR laser network in acquiring LAGEOS-2, which was not overly surprising based on the predicted accuracy of the MMNAV solutions. Post-mission analysis showed additional unmodeled errors in the separation ΔVs, although the analysis is not yet complete.

Acknowledgements:

The work described in this paper was performed at the Jet Propulsion Laboratory, California Institute of Technology, under contract with the National Aeronautics and Space Administration. The authors wish to gratefully acknowledge the technical direction of Jordan Ellis, who supervised the authors during the LAGEOS-2 navigation effort, and to thank Bernadette Tucker, Earl Higa, Prem Menon, Mark Ryne, and Scott Fullner for their work during LAGEOS-2 operations. The assistance of Captains Aiken and Slauenwhite of U. S. Space Command is also sincerely appreciated.

Electro-Optical Space Surveillance Experiments With a Workstation-Based Data Acquisition System

P. D. Tennyson and P. J. Shread (MIT / Lincoln Laboratory)

I. Introduction

The Advanced Electro-Optical Space Surveillance (EOSS) Technology Program at MIT / Lincoln Laboratory develops Visible and Mid-Wave Infrared staring imager technology and optimal signal processing technology for space and missile surveillance applications. The program emphasizes system studies to determine requirements and perform design trades, and laboratory and field testing of the technology. The transfer of technology to the user community and the resulting interaction is a key goal of the program.

The laboratory and field testing serves many purposes to the program. Technology is evaluated in realistic modes of operation with real targets and backgrounds. Sensor designs can be evaluated. Functional experiments can be performed to support the development of space-based systems. A database of realistic backgrounds and target signatures can be generated for the evaluation of target and detection models, as well as sensor modeling efforts.

The primary field test location for the EOSS program is the Experimental Test System (ETS) Site in Socorro, NM. This site performs a number of space and missile surveillance functions. Sensor technologies and concepts are evaluated and demonstrated. Surveillance techniques are developed and refined in a quasi-operational surrounding. Space object measurements can be performed on objects at all altitudes. The ETS telescope suite includes computer controlled 31 inch and 14 inch telescopes in two domes. Routine observations performed at the ETS site include debris search and White Sands Missile Range launch support.

The visible band CCD experimental camera is used to provide the support electronics to operate the Lincoln Laboratory visible imagers. This camera houses the imager in a dewar which is capable of cooling the focal plane to -50C. The camera performs imager timing and analog video processing. Each frame is time tagged with IRIG-B to the nearest millisecond. The camera generates status information including exposure time, electronic gain, shutter state and focal plane, electronics and dewar temperatures. The camera is controlled through a RS-232 serial link and is form-factor compatible with the GEODSS EBSICON cameras.

The visible sensor camera system runs a 420 by 420 pixel Lincoln Laboratory CCID-7. The camera has a demonstrated total system noise of 3.5 to 5 electrons at a 1 MHz pixel rate. The video signal is digitized to 12 bits. The highest gain yields 2.39 electrons per digital number on average. The dark current of the camera is 8 electrons per pixel per second at -50C. The camera has a range of exposure times from 0.2 seconds to 102.4 seconds. The camera may be mounted on the 31 inch ETS main telescope at either Prime or Cassegrain focus. A second configuration emulates the plate scale of the 6 inch telescope used in the Space Based Visible (SBV) package on the SDI Midcourse Experiment (MSX) Satellite.

II. Data Acquisition System

The laboratory and field testing for the EOSS program has driven the development of a data acquisition system. The data acquisition system is based on a UNIX workstation. The workstation system was designed to perform multiple processing functions for the EOSS program. The primary role of the workstation is that of data acquisition and recording. The workstation serves as a quasi-real-time signal processor evaluation platform during data acquisition. The post-test data reduction is performed on the same workstation. The planning and conducting of experiments utilize many of the same data reduction tools. The workstation is used to organize the data into a database for user access in a timely manner. The imagers are characterized with both live and recorded data. The workstation is used to emulate the signal processors to evaluate advanced algorithms. The workstation is used to perform data communication with the camera, telescope mount and the data processing centers in Lexington.

The system requirements were driven by desired functionality and budgetary constraints. The workstation must be small, lightweight and commercially available and supported. The workstation must be programmable in a 'high level' language such as C or FORTRAN. The data acquisition system must be able to handle the input of data at the camera rate of 2 Mbytes per second for a DMA burst. The system must be able to archive and display imagery data in real-time. The system must be relatively inexpensive. There must be clearly defined expansion paths. Finally, the system must be easy to maintain.

The system developed to meet these goals was a commercially available Silicon Graphics Personal IRIS 4D/35. The processor in the workstation is 36 MHz MIPS R3000 with 40 Mbytes of RAM. The graphics sub-system was the TURBO-GRAPHICS option. The external disk farm consisted of three 1.2 Gbyte SCSI-2 disks configured as a logical device. The disk farm achieved a sustained throughput

greater than 4 MBytes per second. The archive media used is an EXABYTE 8200 2.2 Gbyte 8 MM tape drive with a sustained throughput of 0.26 MBytes per second. Newer EXABYTE drives can be up to 10 times faster. The workstation provides 4 internal serial RS-232 compatible ports and a high performance Ethernet connection. An IKON 10099 board is the DMA interface to the camera. The entire system is easily programmable in both C and FORTRAN languages. The data flow through the data workstation is shown in the figure.

A custom C-language device driver was written to provide low level access to the IKON DMA board. The device driver handles all the time critical interactions with the DMA board. This device driver has a measured response latency of 150 micro-seconds. The device driver inverts the image to match the sky and also synchronizes requests from two processes. Programs access the hardware through the UNIX file system just as if it were a standard UNIX file. This transparent access allows the applications code to be debugged without need of the hardware interface. The interface to existing programs is also simplified, thus dramatically increasing the re-usability of code and increasing programmer efficiency.

The communication between the various processes in the applications program is accomplished through the UNIX Interprocess Communication (IPC) facility. The data communication is through the use of Shared Memory allowing multiple processes to access the same data in RAM. The communication of small data packets is accomplished by the use of the Message Queue facility. The flexibility of this technique is that the writer and reader of the queue need not know anything about each other. Thus signal processing algorithms may be changed easily and transparently to other processes. The bi-directional nature of the queues allows for synchronization of non-time critical processes. This technique also simplifies the testing of modules. Only the interface must be designed before testing of the other module can take place. There is a natural "hook" for diagnostics. The use of message queues allows the processes to reside on different physical machines and to communicate by way of UNIX sockets. This allows the processing load to be distributed for maximum throughput.

The user interacts with the application program through a window-based user interface. The raw image is displayed as it is recorded. A processed image with crude target enhancement is displayed upon request. The gain and contrast of the displayed images are controlled by directly accessing the hardware color tables. The user adjusts these values by a set of sliders. The camera and utility status and control are displayed in a set of network transparent windows. The status of the tape archiving and

signal processing processes are each displayed in a separate window. The user controls the function of the data acquisition programs by use of Function keys.

III. Field Test Results

The workstation data acquisition system has been successfully used in two field data gathering efforts at the ETS. The first field test was in November of 1991 and the second was in September-October of 1992. The imagers tested included both front and back illuminated CCID-7's. A variety of resident space objects and astronomical objects was observed. The recorded data has been used to test signal processing and mission planning algorithms of the SPOCC and its associated network communication processor.

The Soviet space station, MIR, was observed during a terminator crossing pass. The object was acquired while fully illuminated in twilight background conditions. At acquisition, MIR saturated the CCD on the 6 inch telescope. It had an estimated brightness of second magnitude (V-band). The sky background was measured by the CCD to be about 17th magnitude per square arcsecond. As the object was tracked, the sky background dropped to about 20.5th magnitude per square arcsecond. The object brightness dropped after the background brightness dropped due to the shadow height. The object decreased in brightness to about 13th magnitude. The object was tracked for approximately 250 seconds, of which 100 seconds were after terminator crossing. The residual brightness of MIR is thought to be due to self-illumination and earthshine.

Geosynchronous satellites are routinely used as calibration targets as they always move at approximately the same apparent angle rate with respect to the fixed stars. The same geosynchronous satellites are almost always visible. The frameset which contains three geosynchronous communication satellites has a highly inclined object with a large brightness fluctuation moving through the frame. This frameset with crossing streaks was used to identify a weakness in the SBV signal processing algorithm, which has been corrected. Many framesets have been successfully processed with the SBV algorithm to validate the underlying assumptions. The development and validation of signal processing algorithms is a key aspect of the EOSS program.

The ability of the data acquisition system to control the camera exposure time and mount position allows for the efficient detection of objects moving at a wide range of apparent angle rates. MIR was detected in both staring and track modes with exposure times of 0.2 seconds and 1.6 seconds. The typical exposure time for

geosynchronous objects using the 6 inch telescope is a dwell-in-cell matched 1.6 seconds. Super-synchronous objects move at even slower apparent angle rates near apogee. The Soviet X-ray astronomy satellite, GRANAT, is in a highly elliptical orbit with apogee near 180,000 kilometers. This object was acquired with the 6 inch telescope at a range of 120,000 kilometers. The apparent angle rate was 1.6 arcseconds per second. The SBV signal processing algorithm successfully detected the object.

While satellites are the principle target of the EOSS program's field measurements effort, astronomical objects are convenient metric and photometric calibration sources. The brightness and color indices of the stars in the old galactic cluster NGC-188 have been accurately measured. NGC-188 is a handy calibration field as it is near the North Celestial pole and is thus always above the horizon for a mid-latitude site such as the ETS. The minimum brightness object in this field is a 20th magnitude star near the center of the cluster. This object is detectable with an SNR of greater than 3 for a front illuminated CCID-7 mounted on the 31 inch telescope in a 1.6 second exposure. The minimum detectable star with the 6 inch telescope at a 1.6 second exposure is fainter than 16th magnitude.

The imaging ability of the sensor system can be qualitatively evaluated by observing nebulae. The nebulae have diffuse dust and gas spatial backgrounds with stars present in the same field. The stars may be foreground, background or associated with the nebula. The large intra-scene dynamic range, greater than 1 million, is stressing to the electronic imager. The nebula in Orion is a good background for synthetic target framesets as there is a strong gradient in background and several saturated stars adding to the scene clutter. The Great Nebula in Andromeda, M31, is also a good candidate for synthetic scene generation and quite often has real resident space objects passing through its image.

IV. Summary

A UNIX workstation based data acquisition system has been designed to gather imagery data for advanced technology cameras. This system has demonstrated the capabilities of the imagers developed as part of the Advanced EOSS technology program at Lincoln Laboratory. The data acquisition system has been successfully used in several field measurement efforts. The data recorded has been extensively used in signal processing algorithm development for both the EOSS and the SBV programs.

DATA ACQUISITION SYSTEM – DATA FLOW

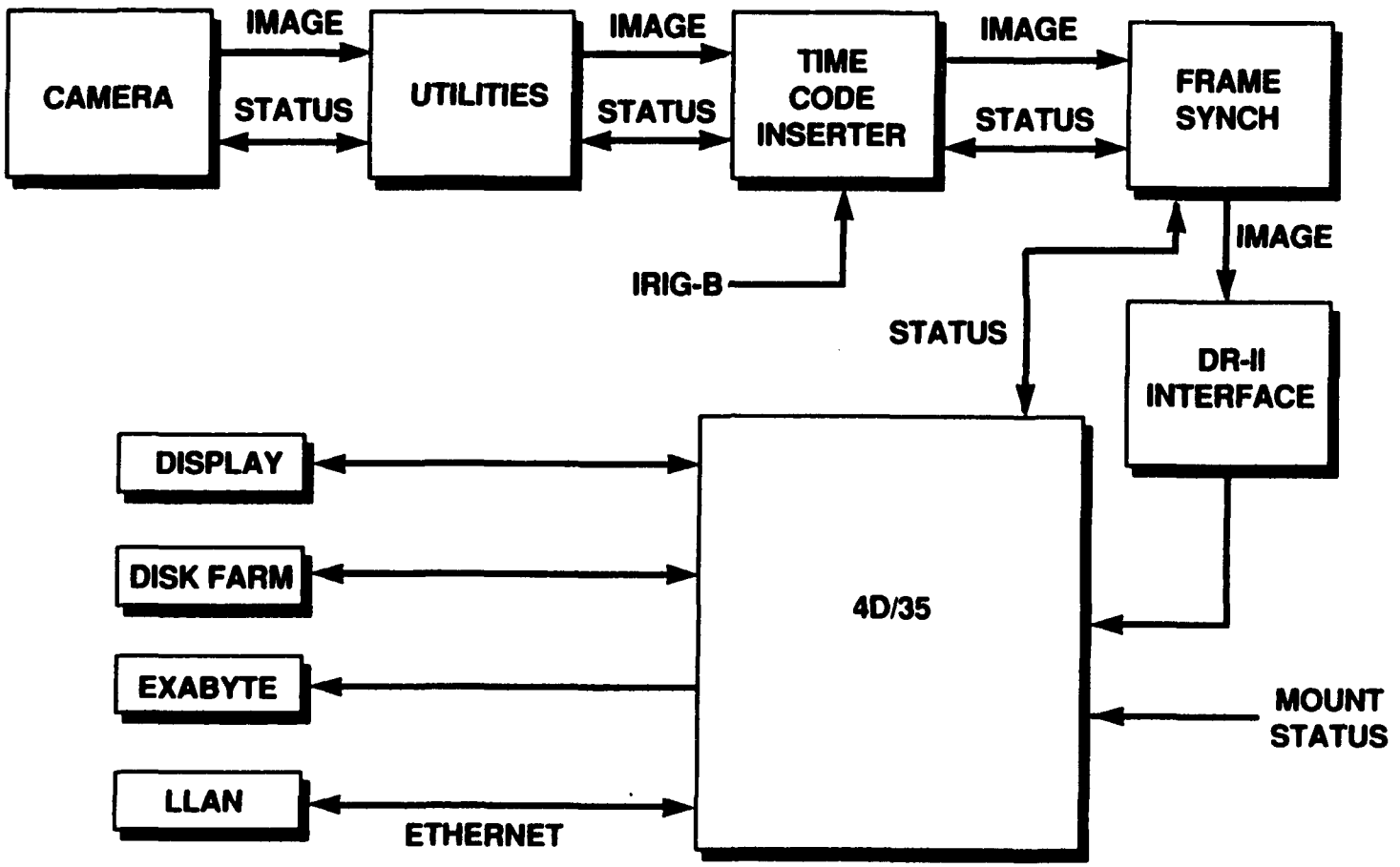

193292-2

SEMIANALYTIC SATELLITE THEORY: MATHEMATICAL ALGORITHMS

D. A. Danielson (Mathematics Dept., Naval Postgraduate School)

Modern space surveillance requires fast and accurate orbit predictions for myriads of objects in a broad range of Earth orbits. Conventional Special Perturbations orbit propagators, based on numerical integration of the osculating equations of motion, are accurate but extremely slow (typically requiring 100 or more steps per satellite revolution to give good predictions). Conventional General Perturbations orbit propagators, based on fully analytical orbit theories like those of Brouwer, are faster but contain large errors due to inherent approximations in the theories. New orbit generators based on Semianalytic Satellite Theory have been able to approach the accuracy of Special Perturbations propagators and the speed of General Perturbations propagators.

Semianalytic Satellite Theory has been originated by P. J. Cefola and his colleagues, whose names are listed in the references. The theory is scattered throughout the listed conference pre-prints, published papers, technical reports, and private communications. We have simplified, assembled, and extended the theory in a single integrated document [Danielson, Early, and Neta, 1993]. In this summary some of the salient features of the theory will be briefly described.

Semianalytic Satellite Theory represents the orbital state of a satellite with an equinoctial element set $(a_1, \cdots a_6) = (a, h, k, p, q, \lambda)$. The first five elements $a_1, \cdots a_5$ are slowly varying in time. The sixth element a_6 is the mean longitude λ and so is rapidly varying.

The orbital elements are governed by the Variation-of-Parameters equations of motion

$$\frac{d\hat{a}_i}{dt} = n(\hat{a})\delta_{i6} + F_i(\hat{a}, \hat{h}, \hat{k}, \hat{p}, \hat{q}, \hat{\lambda}, t) \tag{1}$$

Here t is the time, n is the Kepler mean motion, δ_{i6} is the Kronecker delta, and F_i give the element rates of change due to the perturbing forces. Hats distinguish the elements of the osculating ellipse from the elements of the averaging procedure. The osculating rate functions F_i may be decomposed into the sum of the contributions due to separate perturbations:

$$F_i = \sum_{\alpha} F_{i\alpha} \tag{2}$$

Semianalytic Satellite Theory decomposes the osculating elements $\hat{a}_i$ into mean elements a_i plus a small remainder which is 2π periodic in the fast variable:

$$\hat{a}_i = a_i + \sum_{\alpha} \eta_{i\alpha}(a, h, k, p, q, \lambda, t) + \sum_{\alpha,\beta} \eta_{i\alpha\beta}(a, h, k, p, q, \lambda, t) + \cdots \tag{3}$$

Using the Generalized Method of Averaging, we can show that the mean elements are governed by equations of the form

$$\frac{da_i}{dt} = n(a)\delta_{i6} + \sum_{\alpha} A_{i\alpha} + \sum_{\alpha,\beta} A_{i\alpha\beta} + \cdots \tag{4}$$

The mean element rates A_i are given at each order by

$$A_i = < G_i > \tag{5}$$

where the functions G_i are given to first and second order by

$$G_{i\alpha} = F_{i\alpha}(a, h, k, p, q, \lambda, t) \tag{6}$$

$$G_{i\alpha\beta} = \sum_{j=1}^{6} \frac{\partial F_{i\alpha}}{\partial a_j} \eta_{j\beta} + \frac{15}{8} \frac{\eta_{1\alpha}\eta_{1\beta}}{a^2} n(a)\delta_{i6} - \sum_{j=1}^{6} \frac{\partial \eta_{i\alpha}}{\partial a_j} A_{j\beta} \tag{7}$$

Here $< f >$ denotes an averaging operator, which for single-averaged perturbations (atmospheric drag, solar radiation pressure, central-body gravitational zonal harmonics, third-body point mass effects) is

$$< f >= \frac{1}{2\pi} \int_{-\pi}^{\pi} f(a, h, k, p, q, \lambda, t) d\lambda \tag{8}$$

and for double-averaged perturbations (central-body gravitational tesseral harmonics) is

$$\begin{aligned} < f > \; = \; & \frac{1}{4\pi^2} \int_{-\pi}^{\pi} \int_{-\pi}^{\pi} f(a, h, k, p, q, \lambda, \theta, t) d\lambda d\theta \\ & + \frac{1}{2\pi^2} \sum_{(j,m)\in\mathcal{B}} \left[\cos(j\lambda - m\theta) \int_{-\pi}^{\pi} \int_{-\pi}^{\pi} f(a, h, k, p, q, \lambda', \theta') \cos(j\lambda' - m\theta') d\lambda' d\theta' \right. \\ & \left. + \sin(j\lambda - m\theta) \int_{-\pi}^{\pi} \int_{-\pi}^{\pi} f(a, h, k, p, q, \lambda', \theta') \sin(j\lambda' - m\theta') d\lambda' d\theta' \right] \end{aligned} \tag{9}$$

Here $\mathcal{B}$ is the set of all ordered pairs (j, m) with the properties

$$\begin{aligned} & m \geq 1 \\ & |j\dot{\lambda} - m\dot{\theta}| < \frac{2\pi}{\tau} \end{aligned} \tag{10}$$

where τ is the minimum period desired for perturbations included in the averaged equations of motion, θ is the central-body rotation angle, and dots denote time derivatives.

If all the perturbations are single-averaged, the short-periodic variations η_i are given at each order by

$$\eta_i \; = \; \xi_i + \sum_{k=1}^{K} \frac{(-1)^k}{n^k} \int_k \frac{\partial^k \xi_i}{\partial t^k} d\lambda^k - \frac{3}{2a} \delta_{i6} \left[\int \xi_1 d\lambda + \sum_{k=1}^{K} (k+1) \frac{(-1)^k}{n^k} \int_{k+1} \frac{\partial^k \xi_1}{\partial t^k} d\lambda^{k+1} \right] \tag{11}$$

where

$$\xi_i = \frac{1}{n} \int (G_i - < G_i >) d\lambda \tag{12}$$

$$\left\langle \int_j \xi_i d\lambda^j \right\rangle = \left\langle \underbrace{\int \cdots \int}_{j} \xi_i \underbrace{d\lambda \cdots d\lambda}_{j} \right\rangle = 0 \tag{13}$$

Here the derivative terms account for weak time-dependence effects, such as the motion of the moon.

If the perturbations are single-averaged, then the osculating rate functions $F_{i\alpha}$ can be written as a Fourier series in λ:

$$F_{i\alpha}(a,h,k,p,q,\lambda,t) = C^0_{i\alpha}(a,h,k,p,q,t) + \sum_{j=1}^{\infty}[C^j_{i\alpha}(a,h,k,p,q,t)\cos j\lambda + S^j_{i\alpha}(a,h,k,p,q,t)\sin j\lambda] \tag{14}$$

Using (5, 6, 8, 11, 12, 13), we obtain the first-order mean element rates $A_{i\alpha}$ and short-periodic variations $\eta_{i\alpha}$:

$$A_{i\alpha} = C^0_{i\alpha} \tag{15}$$

$$\eta_{i\alpha} = \sum_{j=1}^{\infty}(C^j_{i\alpha}\cos j\lambda + S^j_{i\alpha}\sin j\lambda) \tag{16}$$

where

$$\begin{aligned}
C^j_i &= -\frac{1}{jn}\left[S^j_i - \frac{3}{2}\frac{1}{a}\frac{\delta_{i6}}{j}C^j_1\right] + \frac{1}{(jn)^2}\left[\frac{\partial C^j_i}{\partial t} + \frac{3}{2}\frac{2}{a}\frac{\delta_{i6}}{j}\frac{\partial S^j_1}{\partial t}\right] \\
&\quad + \frac{1}{(jn)^3}\left[\frac{\partial^2 S^j_i}{\partial t^2} - \frac{3}{2}\frac{3}{a}\frac{\delta_{i6}}{j}\frac{\partial^2 C^j_1}{\partial t^2}\right] - \frac{1}{(jn)^4}\left[\frac{\partial^3 C^j_i}{\partial t^3} + \frac{3}{2}\frac{4}{a}\frac{\delta_{i6}}{j}\frac{\partial^3 S^j_1}{\partial t^3}\right] - \cdots \\
S^j_i &= \frac{1}{jn}\left[C^j_i + \frac{3}{2}\frac{1}{a}\frac{\delta_{i6}}{j}S^j_1\right] + \frac{1}{(jn)^2}\left[\frac{\partial S^j_i}{\partial t} - \frac{3}{2}\frac{2}{a}\frac{\delta_{i6}}{j}\frac{\partial C^j_1}{\partial t}\right] \\
&\quad - \frac{1}{(jn)^3}\left[\frac{\partial^2 C^j_i}{\partial t^2} + \frac{3}{2}\frac{3}{a}\frac{\delta_{i6}}{j}\frac{\partial^2 S^j_1}{\partial t^2}\right] - \frac{1}{(jn)^4}\left[\frac{\partial^3 S^j_i}{\partial t^3} - \frac{3}{2}\frac{4}{a}\frac{\delta_{i6}}{j}\frac{\partial^3 C^j_1}{\partial t^3}\right] + \cdots
\end{aligned} \tag{17}$$

Substituting (14)–(16) into (7), we obtain the second-order functions $G_{i\alpha\beta}$:

$$G_{i\alpha\beta} = \mathcal{C}^0_{i\alpha\beta} + \sum_{j=1}^{\infty}(\mathcal{C}^j_{i\alpha\beta}\cos j\lambda + \mathcal{S}^j_{i\alpha\beta}\sin j\lambda) \tag{18}$$

where

$$\begin{aligned}
\mathcal{C}^0_{i\alpha\beta} &= \frac{1}{2}\sum_{j=1}^{\infty}\left[\sum_{r=1}^{5}\left(\frac{\partial \mathcal{C}^j_{i\alpha}}{\partial a_r}C^j_{r\beta} + \frac{\partial \mathcal{S}^j_{i\alpha}}{\partial a_r}S^j_{r\beta}\right) + j\mathcal{S}^j_{i\alpha}C^j_{6\beta} - j\mathcal{C}^j_{i\alpha}S^j_{6\beta} + \frac{15n}{8a^2}\delta_{i6}(C^j_{1\alpha}C^j_{1\beta} + S^j_{1\alpha}S^j_{1\beta})\right] \\
\mathcal{C}^j_{i\alpha\beta} &= \sum_{r=1}^{5}\left[\frac{\partial \mathcal{C}^o_{i\alpha}}{\partial a_r}C^j_{r\beta} - \mathcal{C}^0_{r\beta}\frac{\partial \mathcal{C}^j_{i\alpha}}{\partial a_r} + \frac{1-\delta_{j1}}{2}\sum_{k=1}^{j-1}\left(\frac{\partial \mathcal{C}^{j-k}_{i\alpha}}{\partial a_r}C^k_{r\beta} - \frac{\partial \mathcal{S}^{j-k}_{i\alpha}}{\partial a_r}S^k_{r\beta}\right)\right. \\
&\quad \left. + \frac{1}{2}\sum_{k=1}^{\infty}\left(\frac{\partial \mathcal{C}^{j+k}_{i\alpha}}{\partial a_r}C^k_{r\beta} + \frac{\partial \mathcal{C}^k_{i\alpha}}{\partial a_r}C^{j+k}_{r\beta} + \frac{\partial \mathcal{S}^{j+1}_{i\alpha}}{\partial a_r}S^r_{k\beta} + \frac{\partial \mathcal{S}^k_{i\alpha}}{\partial a_r}S^{j+k}_{k\beta}\right)\right] \\
&\quad - j\mathcal{C}^o_{6\beta}S^j_{i\alpha} + \frac{1-\delta_{j1}}{2}\sum_{k=1}^{j-1}\left[(j-k)(\mathcal{S}^{j-k}_{i\alpha}C^k_{6\beta} + \mathcal{C}^{j-k}_{i\alpha}S^k_{6\beta}) + \frac{15n}{8a^2}\delta_{i6}(C^{j-k}_{1\alpha}C^k_{1\beta} - S^{j-k}_{1\alpha}S^k_{1\beta})\right] \\
&\quad + \frac{1}{2}\sum_{k=1}^{\infty}\left[(j+k)(\mathcal{S}^{j+k}_{i\alpha}C^k_{6\beta} - \mathcal{C}^{j+k}_{i\alpha}S^k_{6\beta}) + k(\mathcal{S}^k_{i\alpha}C^{j+k}_{6\beta} - \mathcal{C}^k_{i\alpha}S^{j+k}_{6\beta})\right. \\
&\quad \left. + \frac{15n}{8a^2}\delta_{i6}(C^{j+k}_{1\alpha}C^k_{1\beta} + C^k_{1\alpha}C^{j+k}_{1\beta} + S^{j+k}_{1\alpha}S^k_{1\beta} + S^k_{1\alpha}S^{j+k}_{1\beta})\right] \\
\mathcal{S}^j_{i\alpha\beta} &= \sum_{r=1}^{5}\left[\frac{\partial \mathcal{C}^o_{i\alpha}}{\partial a_r}S^j_{r\beta} - \mathcal{C}^0_{r\beta}\frac{\partial \mathcal{S}^j_{i\alpha}}{\partial a_r} + \frac{1-\delta_{j1}}{2}\sum_{k=1}^{j-1}\left(\frac{\partial \mathcal{C}^{j-k}_{i\alpha}}{\partial a_r}S^k_{r\beta} + \frac{\partial \mathcal{S}^{j-k}_{i\alpha}}{\partial a_r}C^k_{r\beta}\right)\right. \\
&\quad \left. + \frac{1}{2}\sum_{k=1}^{\infty}\left(-\frac{\partial \mathcal{C}^{j+k}_{i\alpha}}{\partial a_r}S^k_{r\beta} + \frac{\partial \mathcal{C}^k_{i\alpha}}{\partial a_r}S^{j+k}_{r\beta} + \frac{\partial \mathcal{S}^{j+k}_{i\alpha}}{\partial a_r}C^k_{r\beta} - \frac{\partial \mathcal{S}^k_{i\alpha}}{\partial a_r}C^{j+k}_{r\beta}\right)\right] \\
&\quad + j\mathcal{C}^o_{6\beta}C^j_{i\alpha} + \frac{1-\delta_{j1}}{2}\sum_{k=1}^{j-1}\left[(j-k)(\mathcal{S}^{j-k}_{i\alpha}S^k_{6\beta} - \mathcal{C}^{j-k}_{i\alpha}C^k_{6\beta}) + \frac{15n}{8a^2}\delta_{i6}(C^{j-k}_{1\alpha}S^k_{1\beta} + S^{j-k}_{1\alpha}C^k_{1\beta})\right] \\
&\quad + \frac{1}{2}\sum_{k=1}^{\infty}\left[-(j+k)(\mathcal{S}^{j+k}_{i\alpha}S^k_{6\beta} + \mathcal{C}^{j+k}_{i\alpha}C^k_{6\beta}) + k(\mathcal{S}^k_{i\alpha}S^{j+k}_{6\beta} + \mathcal{C}^k_{i\alpha}C^{j+k}_{6\beta})\right. \\
&\quad \left. + \frac{15n}{8a^2}\delta_{i6}(-C^{j+k}_{1\alpha}S^k_{1\beta} + C^k_{1\alpha}S^{j+k}_{1\beta} + S^{j+k}_{1\alpha}C^k_{1\beta} - S^k_{1\alpha}C^{j+k}_{1\beta})\right]
\end{aligned} \tag{19}$$

Using (5, 7, 8, 11, 12, 13), we obtain the second-order mean element rates $A_{i\alpha\beta}$ and short-periodic variations $\eta_{i\alpha\beta}$:

$$A_{i\alpha\beta} = \mathcal{C}^o_{i\alpha\beta} \tag{20}$$

$$\eta_{i\alpha\beta} = \sum_{j=1}^{\infty}(C^j_{i\alpha\beta}\cos j\lambda + S^j_{i\alpha\beta}\sin j\lambda) \tag{21}$$

where the $C^j_{i\alpha\beta}$ and $S^j_{i\alpha\beta}$ are again given by (17) in terms of $\mathcal{C}^j_{i\alpha\beta}$ and $\mathcal{S}^j_{i\alpha\beta}$.

As a first example of a specific perturbation to which this theory has been applied, let us consider atmospheric drag. The perturbing acceleration $\mathbf{q}$ for atmospheric drag is commonly modeled by the formula

$$\mathbf{q} = -\frac{C_D A}{2m}\rho|\dot{\mathbf{r}} - \mathbf{v}|(\dot{\mathbf{r}} - \mathbf{v}) \tag{22}$$

where C_D, A, m, and $\dot{\mathbf{r}} = \frac{d\mathbf{r}}{dt}$ are the drag coefficient, cross-sectional area, mass, and velocity of the satellite, and $\mathbf{v}$ is the velocity of the atmosphere. The osculating rate functions appropriate for a nonconservative perturbing force are

$$F_i(a, h, k, p, q, \lambda, t) = \frac{\partial a_i}{\partial \dot{\mathbf{r}}} \cdot \mathbf{q} \tag{23}$$

The Fourier coefficients in the λ-expansion (14) of the osculating rate functions are thus

$$\begin{aligned} C_i^o &= \frac{1}{2\pi}\int_{\lambda_1}^{\lambda_2} \frac{\partial a_i}{\partial \dot{\mathbf{r}}} \cdot \mathbf{q}\, d\lambda \\ C_i^j &= \frac{1}{\pi}\int_{\lambda_1}^{\lambda_2} \frac{\partial a_i}{\partial \dot{\mathbf{r}}} \cdot \mathbf{q}\cos j\lambda\, d\lambda \\ S_i^j &= \frac{1}{\pi}\int_{\lambda_1}^{\lambda_2} \frac{\partial a_i}{\partial \dot{\mathbf{r}}} \cdot \mathbf{q}\sin j\lambda\, d\lambda \end{aligned} \tag{24}$$

where (λ_1, λ_2) indicate the values of λ at atmosphere entry and exit. The integrals (23) are evaluated numerically using Gaussian quadrature formulas.

As a second example, let us consider the central-body gravitational potential. When expressed in terms of equinoctial elements, the disturbing function due to the central-body tesseral harmonics turns out to be

$$\begin{aligned} \mathcal{R} = \mathrm{Re}\Big\{\frac{\mu}{a}\sum_{j=-\infty}^{\infty}\sum_{m=1}^{M}\sum_{s=-N}^{N}\sum_{n=\max(2,m,|s|)}^{N} &(\frac{R}{a})^n I^m V_{ns}^m \Gamma_{ns}^m K_j^{-n-1,s} P_\ell^{vw} \\ &(G_{ms}^j + iH_{ms}^j)(C_{nm} - iS_{nm})e^{i(j\lambda - m\theta)}\Big\} \end{aligned} \tag{25}$$

Here μ and R are the central-body gravitational constant and equatorial radius, C_{nm} and S_{nm} are geopotential coefficients, I is $+1$ for the direct equinoctial elements and -1 for the retrograde equinoctial elements, N and M denote the maximum degree and order of the geopotential field, and $i = \sqrt{-1}$. The V_{ns}^m, Γ_{ns}^m, G_{ms}^j, H_{ms}^j functions are defined by

$$V_{ns}^m = \begin{cases} \dfrac{(-1)^{\frac{n-s}{2}}}{2^n}\dfrac{(n+s)!(n-s)!}{(n-m)!(\frac{n+s}{2})!(\frac{n-s}{2})!} & \text{if } n-s \text{ is even} \\ 0 & \text{if } n-s \text{ is odd} \end{cases} \tag{26}$$

$$\Gamma_{ns}^m(\gamma) = \begin{cases} (-1)^{m-s}2^s(1+I\gamma)^{-Im} & \text{if } s \le -m \\ (-1)^{m-s}2^{-m}\dfrac{(n+m)!(n-m)!}{(n+s)!(n-s)!}(1+I\gamma)^{Is} & \text{if } |s| \le m \\ 2^{-s}(1+I\gamma)^{Im} & \text{if } s \ge m \end{cases} \tag{27}$$

$$G^j_{ms} + iH^j_{ms} = \begin{cases} [k + ih\ \mathrm{sgn}(s-j)]^{|s-j|}(\alpha + iI\beta)^{m-Is} & \text{if} \quad |s| \le m \\ [k + ih\ \mathrm{sgn}(s-j)]^{|s-j|}[\alpha - i\beta\ \mathrm{sgn}(s-m)]^{|s-Im|} & \text{if} \quad |s| \ge m \end{cases} \tag{28}$$

where $\mathrm{sgn}(x)$ denotes the sign of x, and (α, β, γ) are the cosines of the angles between the geographic central axis and the equinoctial reference axes. The kernels K^{ns}_j of the Hansen coefficients are defined by

$$K^{ns}_j(e) = \frac{e^{-|s-j|}}{2\pi} \int_{-\pi}^{\pi} \left(\frac{r}{a}\right)^n \cos(sf - jM) dM \tag{29}$$

where e is the orbital eccentricity, r is the distance from the center of mass of the central body to the satellite, f is the true anomaly, and M is the mean anomaly. The $P^{vw}_\ell(\gamma)$ are Jacobi polynomials with indices defined by

$$\begin{aligned} \ell &= \begin{cases} n-m & \text{if} \quad |s| \le m \\ n-|s| & \text{if} \quad |s| > m \end{cases} \\ v &= |m-s| \\ w &= |m+s| \end{aligned} \tag{30}$$

Each of the functions V^m_{ns}, Γ^m_{ns}, G^j_{ms}, H^j_{ms}, K^{ns}_j, P^{vw}_ℓ and their derivatives may be efficiently calculated using recurrence relations. The osculating rate functions appropriate for a conservative force are

$$F_i(a,h,k,p,q,\lambda,\theta,t) = -\sum_{j=1}^{5} (a_i, a_j) \frac{\partial \mathcal{R}}{\partial a_j} \tag{31}$$

where (a_i, a_j) are the Poisson brackets. By substituting (25) into (31) and then taking the real part of the result, we can cast F_i into the real form

$$F_i(a,h,k,p,q,\lambda,\theta,t) = \sum_{j,m} \left[C^{jm}_i(a,h,k,p,q,t) \cos(j\lambda - m\theta) + S^{jm}_i(a,h,k,p,q,t) \sin(j\lambda - m\theta) \right] \tag{32}$$

where C^{jm}_i and S^{jm}_i are known analytical functions. Then using (5, 6, 9), we obtain the first-order mean element rates $A_{i\alpha}$:

$$A_{i\alpha} = \sum_{\substack{j=-\infty \\ (j,m)\in B}}^{\infty} \sum_{m=1}^{M} [C^{jm}_i \cos(j\lambda - m\theta) + S^{jm}_i \sin(j\lambda - m\theta)] \tag{33}$$

i. e., only the resonant tesserals contribute to the mean element rates. By a similar procedure as was used to derive (16), we obtain the first-order short-periodics $\eta_{i\alpha}$ in the absence of explicit time-dependence:

$$\eta_{i\alpha} = \sum_{\substack{j=-\infty \\ (j,m)\notin B}}^{\infty} \sum_{m=1}^{M} [C^{jm}_i \cos(j\lambda - m\theta) + S^{jm}_i \sin(j\lambda - m\theta)] \tag{34}$$

where

$$
\begin{aligned}
C_i^{jm} &= -\frac{1}{jn - m\dot{\theta}} \left[S_i^{jm} - \frac{3}{2} \frac{n}{a} \frac{\delta_{i6}}{jn - m\dot{\theta}} C_1^{jm} \right] \\
S_i^{jm} &= \frac{1}{jn - m\dot{\theta}} \left[C_i^{jm} + \frac{3}{2} \frac{n}{a} \frac{\delta_{i6}}{jn - m\dot{\theta}} S_1^{jm} \right]
\end{aligned}
\tag{35}
$$

Semianalytic Satellite Theory has also been fully developed for the central-body gravitational zonal harmonics, the third-body point mass gravitational potential, and solar radiation pressure. For certain perturbations, expansions in the true longitude L or eccentric ongitude F have advantages over the λ-expansions. Complete details are given in [Danielson, Early, and Neta, 1993].

Having formulas for the mean element rates, we integrate the mean equations (4) numerically using a Runge-Kutta method with large step sizes (typically one day in length). The formulas for the Fourier coefficients of the short-periodic variations also are only evaluated at the integrator step times. Values of the mean elements and short-periodic variations at times not coinciding with the integrator step times are calculated from Hermite and Lagrange interpolation formulas, respectively.

References

Battin, R. H., *An Introduction to the Mathematics and Methods of Astrodynamics*, American Institute of Aeronautics and Astronautics Education Series, 1987.

Bobick, A., GTDS Subroutine QR, CSDL, 1981.

Broucke, R. A., and Cefola, P. J., "On the Equinoctial Orbit Elements," *Celestial Mechanics* 5, pp. 303–310, 1972.

Capellari, J. O., Velez, C. E., and Fuchs, A. J., (eds.), "Mathematical Theory of the Goddard Trajectory Determination System," Goddard Space Flight Center, X-582–76–77, April 1976.

Cefola, P. J., Long, A. C., and Holloway, G., "The Long-Term Prediction of Artificial Satellite Orbits," AIAA Paper 74–170, AIAA Aerospace Sciences Meeting, Washington, DC, January 1974.

Cefola, P. J., and Broucke, R. A., "On the Formulation of the Gravitational Potential in Terms of Equinoctial Variables," AIAA Paper 75–9, AIAA Aerospace Sciences Meeting, Pasadena, CA, January 1975.

Cefola, P. J., "A Recursive Formulation for the Tesseral Disturbing Function in Equinoctial Variables," AIAA Paper 76–839, AIAA/AAS Astrodynamics Conference, San Diego, CA, August 1976.

Cefola, P. J., and McClain, W. D., "A Recursive Formulation of the Short-Periodic Perturbations in Equinoctial Variables," AIAA Paper 78–1383, AIAA/AAS Astrodynamics Conference, Palo Alto, CA, August 1978.

Cefola, P. J., "Second Order Coupling of M-Daily Terms with J_2 Secular Rates," Draper Laboratory internal memo IRD-011-15Z-PJC, July 1981.

Cefola, P. J., "Numerical Testing of the Second Order J_2/M-Daily Coupling Model," Draper Laboratory Internal Memo, September 1981

Cefola, P. J., "Simplified Analytical Model for the Solar Radiation Pressure for Use in the Averaged Orbit Generator," Draper Laboratory internal memo AOD/SD-020-15Z-PJC, October 1982.

Cefola, P. J., and Proulx, R. J., "Application of the Semianalytical Satellite Theory to Shallow Resonance Orbits," AAS Paper 91–139, AAS/AIAA Spaceflight Mechanics Meeting, Houston, TX, February 1991.

Collins, S. K., and Cefola, P. J., "Computationally Efficient Modelling for Long Term Prediction of Global Positioning System Orbits," *Journal of the Astronautical Sciences*, Vol. XXVI, No. 4, pp. 293-314, Oct. - Dec. 1978.

Collins, S. K., "Long Term Prediction of High Altitude Orbits," Ph.D. Dissertation, Department of Aeronautics and Astronautics, Massachusetts Institute of Technology, March 1981.

Danielson, D. A., *Vectors and Tensors in Engineering and Physics*, Addison-Wesley, 1991.

Danielson, D. A., Early, L. W., and Neta, B., "Semianalytic Satellite Theory (SST): Mathematical Algorithms," Naval Postgraduate School Technical Report, 1993.

Early, L. W., "Evaluation of Numerical Quadrature Formulas for Use in Numerically

Averaged Orbit Generators," Computer Sciences Corporation Report CSC/TM-75/6038, 1975.

Early, L. W., "Orbital Mechanics Notes," unpublished, 1982.

Early, L. W., "A Portable Orbit Generator Using Semianalytical Satellite Theory," AIAA Paper 86-2164-CP, AIAA/AAS Astrodynamics Conference, Williamsburg, VA, August 1986.

Escobal, P. R., *Methods of Orbit Determination*, Krieger, 1965.

Ferziger, P., *Numerical Methods for Engineering Application*, Wiley, 1981.

Green, A. J., "Orbit Determination and Prediction Processes for Low Altitude Satellites," Ph.D. Dissertation, Department of Aeronautics and Astronautics, Massachusetts Institute of Technology, December 1979.

Hansen, P. A., "Entwickelung Des Product Einer Potenz Des Radius Vectors Mit Dem Sinus Oder Consinus Eines Vielfachen Der Wahren Anomalie in Reihen," *Abhandlungen Der Mathematisch-Physischen Classer Der Koniglich Sachsischen Gesellschaft Der Wissenschaften*, Vol. 2, Leipzig, FRG, pp. 181–281, 1855. (English translation by J. C. Van der Ha, Mission Analysis, European Space Operations Center, Robert Bosch Str. 5, 6100 Darmstadt, FRG.)

Long, A. C., McClain, W. D., and Cefola, P. J., "Mathematical Specifications for the Earth Satellite Mission Analysis Program (ESMAP)," Computer Sciences Corporation Report CSC/SD-75/6025, June 1975.

Long, A. C., and McClain, W. D., "Optimal Perturbation Models for Averaged Orbit Generation," AIAA/AAS Astrodynamics Conference, San Diego, CA, Aug 18-20, 1976.

Long, A. C., and Early, L. W., "System Description and User's Guide for the GTDS R & D Averaged Orbit Generator," Computer Sciences Corporation Report CSC/SD-78/6020, 1978.

McClain, W. D., "A Recursively Formulated First-Order Semianalytic Artificial Satellite Theory Based on the Generalized Method of Averaging," Volume 1, Computer Sciences Corporation Report CSC/TR-77/6010, 1977.

McClain, W. D., "A Recursively Formulated First-Order Semianalytic Artificial Satellite Theory Based on the Generalized Method of Averaging," Volume 2, Computer Sciences Corporation Report CSC/TR-78/6001, 1978.

McClain, W. D., Long, A. C., and Early, L. W., "Development and Evaluation of a Hybird Averaged Orbit Generator," AIAA Paper 78–1382, AIAA/AAS Astrodynamics Conference, Palo Alto, CA, August 1978.

McClain, W. D., and Early, L. W., "Numerical Evaluation of the GTDS R & D Averaged Orbit Generator," Computer Sciences Corporation Report CSC/TM-78/6138, 1978.

McClain, W. D., and Slutsky, M., "A Theory for the Short Period Motion of an Artificial Satellite," AIAA Paper 80–1658, AIAA/AAS Astrodynamics Conference, Danvers, MA, August 1980.

McClain, W. D., "Modeling Impulse and Continuous Thrust Maneuvers with the Semianalytical Satellite Theory," Draper Laboratory internal memo AOD/SD-008-152-WDM, August 1982.

McClain, W. D., "Weak Time Dependence Formulation for the Closed Form Third-Body

Short-Periodic Variations," Draper Laboratory internal memo PL-039-152-WDM, November 1982.

McClain, W. D., "Semianalytic Theory Autonomous Orbit Determination Study," Draper Laboratory Report CDRL 012A2, January 1983.

Nayfeh, A., *Perturbation Methods*, Wiley-Interscience Publication, 1973.

Proulx, R. J., McClain, W. D., Early, L. W., and Cefola, P. J., "A Theory for the Short-Periodic Motion Due to the Tesseral Harmonic Gravity Field," AAS Paper 81–180, AAS/AIAA Astrodynamics Specialist Conference, Lake Tahoe, NV, August 1981.

Proulx, R. J., "Detailed Mathematical Description of the Tesseral Short Periodic Model," Draper Laboratory internal memo M-110-15Z-RP, December 1981.

Proulx, R. J., "Mathematical Description of the Tesseral Resonance and Resonant Harmonic Coefficient Solve-For Capabilities," Draper Laboratory internal memo NSWC-001-15Z-RJP, April 1982.

Proulx, R. J., "Numerical Testing of the Generalized Tesseral Resonance Capability in the GTDS R & D Program," Draper Laboratory Internal Memo NSWC 98115, April 1982.

Proulx, R. J., and McClain, W. D., "Series Representations and Rational Approximations for Hansen Coefficients," *Journal of Guidance, Control, and Dynamics*, Vol. 11, No. 4, pp. 313–319, July–August 1988, .

Shaver, J. S., "Formulation and Evaluation of Parallel Algorithms for the Orbit Determination Problem," Ph.D. Dissertation, Department of Aeronautics and Astronautics, Massachusetts Institute of Technology, March 1980.

Slutsky, M., "Mathematical Description for the Zonal Harmonic Short-Periodic Generator," Draper Laboratory internal memo, 1980.

Slutsky, M., and McClain, W. D., "The First-Order Short-Periodic Motion of an Artificial Satellite Due to Third-Body Perturbations," AAS Paper 81–106, AAS/AIAA Astrodynamics Specialist Conference, Lake Tahoe, NV, August 1981.

Slutsky, M., "The First-Order Short-Periodic Motion of an Artificial Satellite Due to Third-Body Perturbations: Numerical Evaluation," AAS Paper 83–393, AAS/AIAA Astrodynamics Specialist Conference, Lake Placid, NY, August 1983.

Szegō, G., *Orthogonal Polynomials*, American Mathematical Society Colloquium Publications, Vol. XXIII, 1959.

Zeis, E., "A Computerized Algebraic Utility for the Construction of Nonsingular Satellite Theories, MS Dissertation, Department of Aeronautics and Astronautics, Massachusetts Institute of Technology, September 1978.

Zeis, E., and Cefola, P. J., "Computerized Algebraic Utilities for the Construction of Nonsingular Satellite Theories," *Journal of Guidance and Control*, Vol 3, No. 1, pp. 48-54, January–February 1980.

Parallelization of the Naval Space Surveillance Center Satellite Motion Model

CPT W. Phipps (USMA), B. Neta (NPS), D. Danielson (NPS)

Introduction:

The Naval Space Surveillance Center (NAVSPASUR) currently tracks daily over 6000 objects in elliptical orbits around the Earth. To assist in identification and tracking of these objects in orbit, NAVSPASUR uses an analytic satellite motion model implemented in the FORTRAN subroutine, PPT2. This subroutine predicts an artificial satellite's position and velocity vectors at a selected time to aid in the tracking endeavor. Several calls to the subroutine may be required to aid in the identification of one object. A substantial increase in the number of objects will cause the use of PPT2 on a serial computer to become less responsive and computationally burdensome. Additionally, if there exists a desire to increase the accuracy of the NAVSPASUR model, the resulting subroutine would require even more computing resources and make achieving results even more time consuming.

Parallel computing offers one option to decrease the computation time and achieve more real-time results. Use of parallel computers has already proven to be beneficial in reducing computation time in many other applied areas. Parallel computing offers an opportunity to both increase the efficiency of the current model or reduce the computational burden of a more accurate future model. The ultimate objective of this research is to quantitatively determine the parallel computing potential of the current NAVSPASUR analytic model and determine the subsequent reduction in computer time if the model is applied to a hypercube multicomputer.

NAVSPASUR Satellite Motion Model:

NAVSPASUR satellite motion is implemented by the FORTRAN subroutine, PPT2. The subroutine predicts the state vector of cataloged objects in orbit about Earth at selected times in order to identify the objects as they pass through a sensor's window. The NAVSPASUR model is based on a general perturbations, variation of elements model. The model predicts a satellite's state vector based on the analytical integration of the satellite's perturbing accelerations. General perturbation models are usually not as accurate as a special perturbations model (numerical integration of the perturbing accelerations), but can save a considerable amount of computation.

The NAVSPASUR model is based on a theory developed in 1959 by Dirk Brouwer of Yale University (Brouwer, 1959, pp. 378 - 397) and modified by R. L. Lyddane of the U. S. Naval Weapons Laboratory in 1963 (Lyddane, 1963, pp. 555 - 558). The model by Brouwer and Lyddane considers only the zonal perturbations (the Earth's oblateness and asymmetry about the equatorial axis up to the J_5 term). NAVSPASUR modified the model to include atmospheric drag. The effect of sectoral and tesseral perturbations may be computed by a call to a separate subroutine. For a more detail description of the NAVSPASUR model, see (Phipps, 1992, pp. 3 - 33 or Solomon, 1991).

Parallel Computing:

Many articles and books have been written describing the methods to exploit parallel computing, see e.g. (Hwang, 1984) and (Quinn,1987). Parallel computers may be classified by type, architecture, and topology. In this emerging field, there exists slight differences in how to define parallel computing. For

the purposes of this article, the definition of *parallel computing* is defined as the efficient form of information processing emphasizing the concurrent computations and manipulation of data to solve a single problem.

Implicit in the definition of parallel computing are three methods to achieve parallelism. The three methods are temporal parallelism, spatial parallelism, and asynchronous parallelism (Hwang, 1984, p. 20). These methods offer a manner to classify the various types of parallel computers. Parallel computers are classified by type as follows: pipeline computers (like Cray-1), array processors (like Connection Machine), multiprocessors (like Cm* of Carnegie-Mellon University), and multicomputers (like INTEL iPSC hypercube). Multicomputers offer the user an added degree of freedom in programming, because each processor has its own memory and may perform independent operations, . However, interaction between the processors (nodes) may require synchronization to be explicitly programmed in the multicomputer code. The four type classifications are not necessarily mutually exclusive. Many commercially available array processors, multiprocessors, and multicomputers employ pipeline processors to complete operations such as vector processing.

Parallel computers may also be classified according to their architecture. One scheme for classifying digital computers was introduced by Michael J. Flynn in 1966. He introduced a scheme to classify computers based on the multiplicity of instruction and data streams. An *instruction stream* is a sequence of instructions to be executed by the computer. Likewise, a *data stream* is a sequence of data used by the computer. Most serial computers and pure pipeline processors fall in the single instruction stream, single data stream (SISD) category. Array processors are categorized as single instruction stream, multiple data stream (SIMD), while most multiprocessors and multicomputers are multiple instruction stream, single data stream (MISD) machines. (Flynn, 1966)

Another method of classification is by the topology of inter processor connection (see e.g. Quinn, 1987). These connections are the means through which communication between individual processors is conducted.

With faster computation speed being the ultimate objective, certain measures are needed to determine the effectiveness of parallel computing versus serial computing to achieve this objective. Computation speed depends on many factors that include the computer hardware design, the technical specifications of its components, and the algorithm or method of solution used to complete the computations. Two common measures of effectiveness, accounting for both the hardware and the algorithm, are *speedup* and *efficiency*. *Speedup*, S_p, refers to the ratio between the time taken to execute a set of computations serially, T_s, and the time taken to complete the same set of computations exploiting parallelism, T_p,

$$S_p = \frac{T_s}{T_p}.$$

In fact one usually run the same program on one node to find T_s. The other measure, *efficiency*, accounts for the relative cost of achieving a specific speedup. Relative cost is measured as the number of processors required to achieve the speedup. *Efficiency*, E_p, is the ratio between the speedup, S_p, and the number of processors, p (the theoretical speedup),

$$E_p = \frac{S_p}{p}.$$

Many factors could possibly limit the possible speedup and efficiency of a parallel program. These factors include the number of sequential operations that cannot be parallelized, the communication time between individual processors, and the time each processor is idle due to synchronization requirements.

To maximize speedup and efficiency, parallel algorithms must be developed with a specific parallel computer in mind. In determining the parallel computing potential of the NAVSPASUR satellite motion model, an INTEL iPSC/2 hypercube computer, located at the Department of Mathematics at the Naval Postgraduate School, was used. The iPSC/2 is a MIMD multicomputer with a hypercube topology. It consists of a system resource manager (host) and eight (in our configuration) individual processors (nodes). The system resource manager provides the interface between the user and the computing nodes. The host is a 386-based computer, which may be used to process data in addition to providing the interface for the user. The computing nodes are complete, self-contained INTEL 80386 microprocessors. Each computing node also contains a 80387 numeric coprocessor, its own local memory, and a Direct-Connect communications module (DCM). For a full description of the iPSC/2 multicomputer, see iPSC/2 User's Guide, 1990.

Vectorization:

Vectorization is one method to parallelize an existing sequential program. Vectorization is the process of converting blocks of sequential operations into vector instructions that may be pipelined. To assist in the vectorization of a serial program, there exist many commercially-available vectorizing compilers (Quinn, 1987, pp. 233 - 235). Most vectorizing compilers have a limited ability in recognizing sequential blocks to be vectorized and translations may not be always straight forward. INTEL iPSC/2 contains the vectorizing compiler, VAST2. The VAST2 compiler supports only FORTRAN programs and is limited to vectorizing only *do loops* and *if statements* (iPSC/2 VAST2 User's Guide, 1989).

The first method of parallelization considered for the NAVSPASUR model was vectorization. Vectorization is usually simpler than the other methods of parallelization to apply. Additionally, if vectorization proved to be beneficial, it may be incorporated with other parallel computing methods in order to realize even greater speedup and efficiency. The realized speedup due to vectorization is a function of the number of vector operations within a specific algorithm.

Analysis of the FORTRAN subroutine PPT2 showed that the current subroutine contains very few explicit or implicit vector operations. The only apparent vector operation in the satellite state vector prediction portion of PPT2 is the computation of the velocity vector at the very end of the algorithm. VAST2 failed to identify any significant amount of sequential operations that could be vectorized. The propagation of the orbital element set comprises the majority of the computations. The formulas used to propagate the orbital elements may be characterized as lengthy, algebraically-complex, non-linear scalar functions of the mean orbital elements (Phipps, 1992, pp. 11 - 15). Attempts to transform these formulas into a set of vector operations quickly became algebraically overwhelming. Therefore, based on this initial assessment of limited vectorizing potential, vectorization was not considered as a viable method to reduce computation time and efforts to vectorize PPT2 were pursued no further.

Control Decomposition:

Control decomposition is the strategy of dividing tasks or processes among the individual processors (nodes). This strategy incorporates a divide and conquer approach. Control decomposition is recommended for problems with irregular data structures or unpredictable control flows. There exists two methods to schedule the tasks for each node. One method is for the parallel program to self-schedule tasks. One node assumes the role of a manager with the remaining nodes assuming roles as workers. The managing node maintains a list of processes to be accomplished and assigns a processes to the working nodes. The working nodes request jobs, receive processes, and perform the indicated tasks. Implied in the self-scheduling method is the cost of one processor to perform the manager duties. (iPSC/2 User's Guide, 1990, p. 4-4) A second method to pre-schedule the processes. The exact tasks required of each node are explicitly stated in the parallel program. Although this method saves the cost of the managing node and minimizes communication, care must be taken to ensure the processes are evenly distributed among the nodes.

In order to predict a satellite's state vector considering the secular and periodic correction terms due to the zonal harmonics and a correction term for each element due to the sectoral harmonics, the NAVSPASUR model requires the completion of 55 major tasks. The first step in partitioning these tasks among the nodes was to determine which tasks could be completed concurrently. Concurrency was determined by the development of a hierarchy of the formulas used by the NAVSPASUR model. Each of the individual tasks were listed with its respective required input. Tasks which required output from the completion of other tasks were listed below those tasks. Tasks which could be executed concurrently were listed on the same level of the hierarchy.

From this hierarchy of formulas, the number of tasks that can be completed concurrently ranges from 2 to 14. Additionally, the number of FLOPS required varied considerably among tasks. Some tasks required as little as 2 FLOPS, while others could require up to 650 FLOPS. The variance in the number of FLOPS presented a potential problem in load balancing. It was found that a manager-worker algorithm (to achieve load balancing among the nodes) would substantially increase communication time and thus decrease efficiency; therefore a strategy of pre-scheduling the tasks was chosen. The optimal number of nodes was found to be four. Figure 1 shows how the tasks were distributed. Program set named P^3T-4 implements this algorithm. The computation time, t_c, for P^3T-4 to propagate a single satellite is less than half of the computation time for PPT2. Unfortunately, the communication time, t_m, was so high that the total time for P^3T-4 almost twice as long as PPT2 (see Table 1). The causes of the long communication time are number of messages required by this specific partition of tasks and synchronization problem of nodes waiting to receive computed values from other nodes.

One method to reduce the communication to computation ratio is to reduce the amount of communication. One way to reduce the number of communications is to restructure the partitions. However, other partitions using four nodes were analyzed, yet none could significantly reduce the number of messages. One alternative to possibly achieve any speedup was to partition the computations among fewer nodes. Although a two node algorithm displayed potential in reducing the total execution time to less than PPT2, speedup would be further bounded by two. A second alternative for reducing the communication to computation ratio is to somehow increase the amount of computation between messages. The amount of computation could be increased by computing the intermediate values for n satellites in an array and sending the array in one message. The communication would remain essentially

constant and the computation between messages would increase by a factor of n. The efficiency for propagating n objects, E_p^n, is given by

$$E_p^n = \frac{n t_1}{p(n t_c + t_m)}$$

since the communication time is not affected essentially by length of the message. As n increases, the limit is

$$\lim_{n \to \infty} E_p^n = \frac{t_1}{p t_c}$$

Using the values from Table 1, one finds the efficiency is bounded by 0.48, which implies a maximum speedup of the modified algorithm would be bounded by 1.92. Again the benefit of using this strategy is quite limited.

Domain Decomposition:

Domain decomposition is the strategy of dividing the input data or domain among the nodes. The partitioned sets of domain may be specific data sets such as blocks of matrix or represent a specific grid such as used in finite difference or finite element methods to solve partial differential equations. The major difference between control and domain composition is that domain decomposition strategy requires each node to perform essentially the same tasks but with different input data. Domain decomposition is recommended if the calculations are based on a large data structure and the amount of work is the same for each node. An example of domain decomposition is multiplying two large matrices by block multiplication.

The strategy of domain decomposition is to reduce the NAVSPASUR model's computation time by the concurrent computation of several satellites' state vectors. Each node of the hypercube would complete identical tasks on different satellite data sets, simultaneously. Unlike the application of the control decomposition strategy, the application of the domain decomposition strategy to the NAVSPASUR model was seemingly less arduous. First, because each node propagates satellite data sets independent of the other nodes, there exists no requirement for communication or synchronization among the nodes. This lack of communication simplifies the load balancing and sequential bottleneck problems present in the P^3T-4 parallel algorithm. The concern for this algorithm was the potential sequential bottlenecks at input/output portions of the program set. Reading and writing to external files can be very time consuming. In addition to the actual time spent reading/writing to an external file, a certain amount of time is spent to access the file. In order to minimize this time, the number of calls to read/write to a file should be minimized. To minimize time lost to accessing the file cataloging the set of satellites, a node was devoted to both the reading/distributing of input satellite data. Another node is devoted to collecting/writing of the results.

Program set named P^3T implements this algorithm. Table 2 shows the speedup and efficiency for various number of satellites propagated using hypercubes of four and eight nodes. P^3T was successful in reducing overall execution time. As seen in Table 2, the speedup achieved using eight nodes was approximately three times larger than the speedup achieved using four nodes. The efficiency increased

from .45 to .67. The increase in efficiency indicates that P^3T applied to a hypercube of greater dimension could yield even greater speedup and efficiency. Table 2 also shows an small increase in performance as the number of satellites is increased. This increase is due to the diminishing impact of the algorithm's overhead as the total execution time is increased.

The efficiency of the algorithm should increase with the cube dimension until the time to distribute a separate satellite data to each working node exceeds the time required by node to propagate a single satellite. Therefore, a possible improvement in the algorithm's performance can be achieved by applying the algorithm to an optimal dimension hypercube. Because the hypercube at the Naval Postgraduate School is limited to eight nodes, a model was used to estimate the optimal hypercube dimension. The total execution time for P^3T to propagate n satellites with p processors, t(p), can be modeled by the following expression:

$$t(p) = t_{w1}(p) + t_{w2}(p) + t_c(p)$$

where $t_{w1}(p)$ is the time the last node must wait to receive its first satellite data set, $t_{w2}(p)$ is the total time the last node must wait to receive all of its subsequent satellite data sets, and $t_c(p)$ is the time for each node to propagate each share of the n satellites. The time of a single message between the distributing node and each working node was found to be essentially constant (Phipps, 1992, p. 74). For this algorithm, there are p-2 working nodes. Denoting the time to send a single message between the distributing node and a working node as $t_m(1)$, the $t_{w1}(p)$ may be modeled by the following:

$$t_{w1}(p) = (p-3)t_m(1)$$

where $t_m(1)$ denotes the time to send a single message between the distributing and working nodes. For the iPSC/2 it was found that the mean value of $t_m(1)$ was approximately .693 milliseconds. The wait time, $t_{w2}(p)$ is zero unless the number of working nodes is large enough, i.e.

$$t_{w2}(p) = \begin{cases} 0, & t_{w1}(p) \le t_1 \\ (t_{w1}(p) - t_1)\left[\dfrac{n}{p-2} - 1\right] & t_{w1}(p) > t_1 \end{cases}$$

where t_1 is the computation time to propagate a single satellite (11.2 msec). Note that the factor $\frac{n}{p-2} - 1$ is the number of subsequent satellite data sets. The computation time t_c is given by

$$t_c(p) = \frac{n}{p-2} t_1$$

Therefore, the speedup and efficiency are given by

$$S_p = \frac{n \cdot t_1}{t_{w1}(p) + t_{w2}(p) + t_c(p)},$$

$$E_p = \frac{n \cdot t_1}{p\left[t_{w1}(p) + t_{w2}(p) + t_c(p)\right]}.$$

Figure 2 depicts these theoretical estimates of S_p and E_p for propagating 1728 satellites using various dimension hypercubes. The maximum efficiency occurs for hypercube of dimension 4 (16 nodes). A hypercube of dimension 4 achieves a speedup of nearly 14 and an efficiency of almost 90 percent.

Conclusions:

In determining the parallel computing potential of the NAVSPASUR satellite motion model, we found that vectorization and control decomposition strategies proved not beneficial in significantly reducing the computation time. On the other hand, the domain decomposition strategy showed promise. Overall, the main lesson learned from this research was that satellite position prediction can be made more timely through parallel computing. Although the best method of parallelization might vary depending on the specific model used, parallel computing is a viable option to achieve timely satellite position prediction for the growing number of objects in orbit around the Earth.

References:

Brouwer, Dirk, "Solution of the Problem of Artificial Satellite Theory without Drag", *Astronomical Journal*, 64, pp. 378 - 397, 1959.

Flynn, M. J., "Very High-speed Computing Systems", *Proceedings of the IEEE*, v. 54, pp. 1901 - 1909, December 1966.

Hwang, Kai and Briggs, Faye A., *Computer Architecture and Parallel Processing*, McGraw-Hill, Inc., 1984.

iPSC/2 User's Guide, INTEL Corporation, Order Number 311532-006, June 1990.

iPSC/2 VAST User's Guide, INTEL Corporation, Order Number 311571-002, February 17, 1989.

Lyddane, R. H., "Small Eccentricities or Inclinations in the Brouwer Theory of the Artificial Satellite", *Astronomical Journal*, v. 68, pp. 555 - 558, 1963.

Phipps, Warren E., *Parallelization of the Naval Space Surveillance Center (NAVSPASUR) Satellite Motion Model*, M. S. thesis, Naval Postgraduate School, Monterey, CA, 1992.

Quinn, Michael J., *Designing Efficient Algorithms for Parallel Computers*, McGraw-Hill, Inc., 1987.

Solomon, Daniel, *THE NAVSPASUR Satellite Motion Model*, Naval Research Laboratory, Contract N00014-87-C-2547, August 8, 1991.

Table 1:

Algorithm	t_e (milliseconds)	t_m (milliseconds)	t (milliseconds)
PPT2			
(one node)	11.2	NA	11.2
P³T-4			
node 0	4.3	19.0	23.3
node 1	2.2	15.9	18.1
node 2	2.7	14.7	17.4
node 3	5.8	15.7	21.5

Table 2:

P³T	Number of Satellites	S_p	E_p
8 nodes	20736	5.31	.66
	1728	5.37	.67
	144	5.24	.66
	12	4.13	.52
4 nodes	20736	1.78	.45
	1728	1.80	.45
	144	1.79	.45
	12	1.66	.33

Figure 1:

Node 0	Node 1	Node 2	Node 3
Recover a"		Compute T2	
Compute secular corrections -- l, a, and e	Compute secular correction -- g	Compute long period correction -- z	Compute secular correction -- h
Compute long period correction -- l	Compute long period corrections -- e and I	Solve Kepler's Equation	Compute sectoral terms
Compute short period corrections -- l and a	Compute short period corrections -- e and I	Compute short period corrections -- z	Compute long period correction -- h
Solve Kepler's Equation			Compute short period correction -- h
Collect all terms			
Compute state vector			

Figure 2:

N=1728, $T_M(1)$=.693, T1=11.2

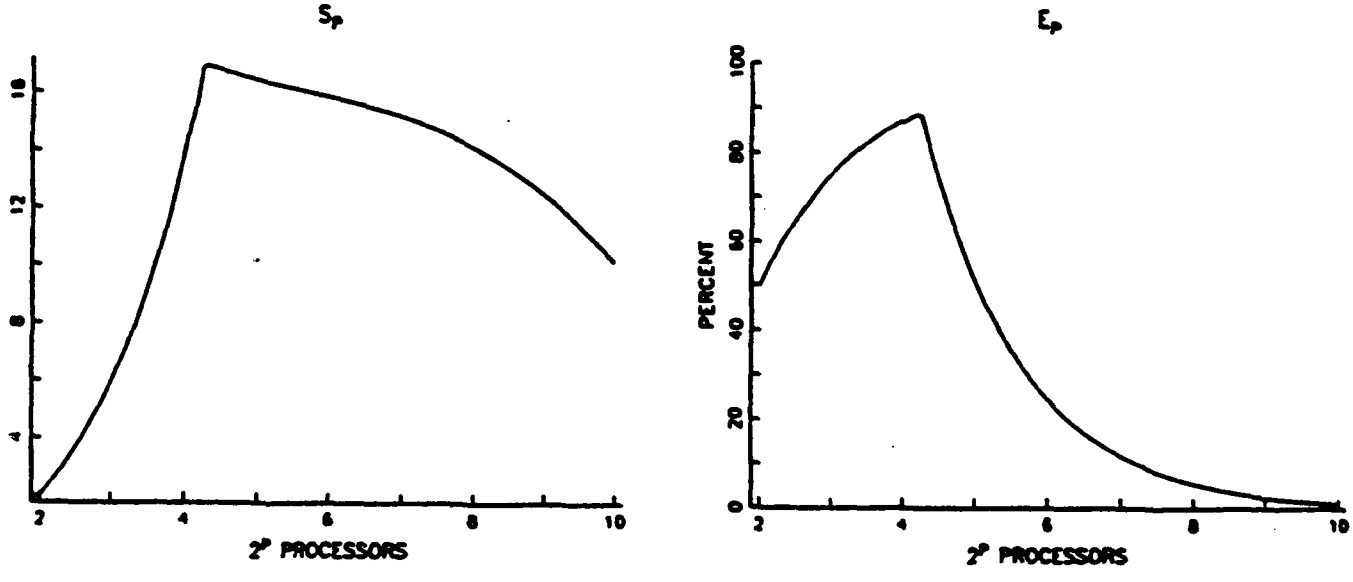

Deep-space imaging with a mm-wave free electron laser*

D. Prosnitz, E. T. Scharlemann (Lawrence Livermore National Laboratory),
Maj. E. P. Gebhard (USAF Ret.)

Abstract

Free electron lasers (FELs) can be thought of as a technique for extending traveling-wave tube technology to higher frequencies and power levels. In the laboratory, mm-wave FEL amplifiers have demonstrated large instantaneous bandwidth, broad tunability and high peak power. We have examined the potential for using a mm-wave FEL as a high resolution, 94-GHz deep-space imaging system. The conceptual design of such a radar system is described below, with particular attention paid to those properties of the FEL that require special consideration if the system is to be used as an imaging radar. These aspects include phase stability, pulse modulation to permit compression, and pulse format.

Introduction

Radar systems for imaging deep-space (e.g., geosynchronous) objects require high average power in order to achieve adequate signal-to-noise ratio in a short observation time, excellent phase stability over the observation time, a broad bandwidth for high resolution, and a rapidly modulated (chirped, phase-modulated, etc.) output signal to exploit the bandwidth. Desirable features include all-weather capability, high frequency to permit small antennas, and an overall size commensurate with relocatability. High resolution, which in principle allows one to distinguish a wealth of features in the imaged object, requires very low range and Doppler sidelobes.

Free electron lasers operating in the millimeter wavelength regime have the potential to meet most, if not all, of the parameters needed for a deep-space imaging radar system. Broad bandwidth with excellent mode quality at very high peak power has been experimentally demonstrated. High average power capability can be achieved by high pulse repetition frequency (PRF) operation of the accelerator that provides the amplifying medium, a relativistic electron beam. Burst-mode high-PRF operation has also been demonstrated in the laboratory. Because an FEL amplifier is nonlinear at high peak power, the instantaneous bandwidth does not directly translate into the ability to amplify a rapidly modulated signal, but simulations indicate that 2-3 GHz modulation of a 94 GHz carrier frequency can be obtained. The radar phase stability requirements impose strict limits on the range over which the accelerator voltage is allowed to sweep during a pulse or a pulse train; the voltage control requirements can be achieved with active control of the accelerator current profile.

FEL amplifiers permit high power operation at frequencies determined primarily by the availability of an input source. Proper design can permit operation of a single FEL amplifier at either 35 or 94 GHz (for example); different mm-wave hardware would be required before the input and after the output of the amplifier, but only a change in electron beam energy or undulator magnetic field would be required in the amplifier. (The undulator is a series of alternating polarity magnets that bunch the electron beam.)

Experimental Background

The Electron Laser Facility (ELF) [Refs. 1, 2, 3] at LLNL provided much of the available experimental data used to assess the utility of mm-wave FEL amplifiers for radar applications. Fig. 1 shows data (compared with simulations) on the amplification of a relatively low power input signal at 35 GHz in a 3-m undulator. With tapering of the undulator - decreasing the undulator magnetic field along its length to compensate for electron energy loss to the mm-wave radiation - a peak output power of 1 GW was achieved, corresponding to the conversion of about 35% of electron beam energy to mm-wave radiation. The overall system gain was 43 dB.

The same accelerator and undulator were also operated at 140 GHz (Fig. 2)with only a change of input source, output diagnostics hardware, and undulator magnetic field. The undulator was an air-core electromagnet, so the undulator field was changed simply by decreasing coil currents. The reduced undulator field lowered the amplifier gain; with the lower input power available at 140 GHz, the FEL amplifier only saturated near the end of its 4-m length and tapering was not useful for enhancing efficiency.

Fig. 3 shows the instantaneous bandwidth achieved in the 35 GHz ELF experiments. The magnetron oscillator was not tunable, but bandwidth was determined by varying the magnetic field of the undulator; over a moderate range in field and frequency varying either drive frequency or undulator magnetic field is approximately equivalent. A magnetic field range of ± 6%, corresponding to a frequency range of about ±12%, could be swept with only 1 dB reduction in total gain. Fig. 4 presents simulations of the anticipated bandwidth (12.5 GHz, or > 10%, to the -1 dB point) at 94 GHz.

The ELF experiments were designed to amplify the TE_{n1} modes, n even, of a highly oversized waveguide (3 cm x 10 cm, compared to 0.87 cm wavelength). The undulator magnetic field was parallel to the short dimension of the waveguide, so that the motion of the electron beam - in the long waveguide direction - coupled primarily to the electric field of the TE_{n1} modes. Measurements of the mode content of the amplified radiation indicated that, at and beyond saturation in the tapered wiggler, 85-90% of the power was contained in the TE_{01} mode despite the oversizing of the waveguide (Fig. 5). The excellent mode quality of the FEL amplifier makes its output power potentially much easier to handle - for example, with a quasi-optical beam transport system - between the amplifier output and the antenna.

Pulse Modulation and Pulse Format

As indicated above, the tapered FEL amplifier is nonlinear, and a bandwidth over which a single frequency can be amplified does not translate into the bandwidth over which a modulated signal can be amplified without distortion. The most significant nonlinearity in a mm-wave FEL amplifier arises from the effects of "slippage": the group velocity of the signal differs slightly from the longitudinal velocity of the electron beam, leading to a smoothing of abrupt transitions in the signal phase or amplitude. No experiments were done at ELF to determine what distortion arises from slippage, but simulations have been done for a bi-phase modulated 94 GHz signal to estimate the distortion [Ref. 4]. Fig. 6 shows the simulated phase distortion for bit rates of 1, 2, 3, and 4 GHz; at 3 GHz the phase modulation shows only modest distortion, but at 4 GHz slippage has nearly completely obliterated the phase transition. The full 12.5 GHz bandwidth of the amplifier is reduced by the nonlinear effect of slippage, but the bandwidth of a signal that can be amplified remains substantial: a 3 GHz bit rate corresponds to 5 cm range resolution. No attempt has been made to date to design a FEL that could be modulated at the full

instantaneous bandwidth. (A frequency-jumped system, could, of course use the full bandwidth.) The pulse format for a mm-wave FEL amplifier is determined by the need to maintain both low range sidelobes and unambiguous Doppler resolution of velocities across the objects to be imaged. Low range sidelobes can be achieved by bi-phase modulation of a 1-μs pulse with a pseudo-random noise (PRN) pattern that has an autocorrelation function characterized by a sharp peak and small (~1/N, where N is the number of bits in the PRN pattern) lobes away from the main peak. Sidelobes in the autocorrelation function will be increased by unintended phase variations during a modulated pulse which may be caused by the FEL amplifier; the dominant source of phase variations will probably be a ripple or sweep of the electron beam voltage during the ~1μs pulse. The requirements on range sidelobe levels thus impose specifications on the permissible voltage ripple of the pulse-power train that drives the accelerator.

A 5-MW, 94-GHz FEL Amplifier

We have examined the potential use of a mm-wave FEL driven by a linear induction accelerator (LIA) as a high resolution, 94-GHz deep-space imaging system. Table I lists the important parameters for the accelerator and the FEL amplifier that would produce 5 MW of average power over the time required to acquire data for an image (which will depend on the apparent rotation rate of the imaged object). A 2.5-kHz PRF not only provides high average power but permits unambiguous velocity resolution up to 4 m/s over the imaged object.

TABLE I. 5-MW 94-GHz FEL parameters

Electron beam voltage	4	MeV
Electron beam current	2	kA
Pulse length	1	μs
PRF	2.5	kHz
Accelerator average power	16	MW
Undulator period	8	cm
Undulator length	3	m
Extraction efficiency†	31	%
Peak mm-wave power	2	GW
Modulation bandwidth	3	GHz

†the fraction of electron beam power converted to mm-wave signal.

A radar system based on the FEL with parameters of Table I would provide a resolution of ~5 cm for features with an RCS of -35 dBsm in a 0.3-s observation time with SNR of 10 dB at 40 Mm.

State of the Technology

The FEL described in Table I represents an extension of present LIA technology in two areas: average power and pulse length. The most recent LIA technology development - as represented by the ETA-II accelerator at LLNL - has been for other purposes and has concentrated on a different pulse format than required for an imaging radar system: specifically, on 50-ns pulses at 2 to 5-kHz PRF. (50-ns pulses are too short to provide low range sidelobes, and 5-kHz is too low a PRF to permit frequency-jump-burst synthesis of a broad bandwidth signal.) The 1-μs pulse of Table I can be achieved by changing the composition (from ferrite to Metglas) and amount of magnetic material in each accelerator cell. ETA-II has recently achieved operation in 50-pulse bursts (limited by the capacitor banks that provided the prime power) at 6 MeV and 2 kA with 50-ns

pulse length and 2-kHz PRF, representing an average electron beam power of 1.2 MW (over the 25-ms burst). The ETA-II electron beam was used to drive a 140-GHz FEL amplifier. In single-pulse experiments, up to 2 GW of peak output power was obtained. In burst-mode FEL experiments (with no optimization because of schedule and funding constraints), amplified pulse trains up to 28 pulses long were obtained, with approximately 10 J per pulse output energy (Fig. 7).

Summary

We have examined the technical feasibility of employing a mm-wave Free Electron Laser for deep-space high-resolution imaging. The FEL appears to offer high power at high frequencies in conjunction with suitable phase control and ample bandwidth.

References

1. T.J. Orzechowski, B.R. Anderson, W.M. Fawley, D. Prosnitz, E.T. Scharlemann, D.B. Hopkins, A.C. Paul, A.M. Sessler and J.S. Wurtele, Phys. Rev. Lett. 54 (1985) 889.

2. T.J. Orzechowski, B.R. Anderson, J.C. Clark, W.M. Fawley, A.C.Paul, D. Prosnitz, E.T. Scharlemann, S.M. Yarema, D.B. Hopkins,A.M. Sessler and J.S. Wurtele, Phys. Rev. Lett. 57 (1986) 2172.

3. A.L. Throop, T.J. Orzechowski, B. Anderson, F.W. Chambers, J.C. Clark, W.M. Fawley, R.A. Jong, A.C. Paul, D. Prosnitz, E.T. Scharlemann, R.D. Stever, G.A. Westenskow, S.M. Yarema, K. Halbach, D.B. Hopkins, and A.M. Sessler, AIAA 19th Fluid Dynamics, Plasma Dynamics, and Laser Conference, Honolulu, Hawaii, June, 1987.

4. D. Prosnitz, E.T. Scharlemann, and M.K. Sheaffer, Proc. 13th International Free Electron Laser Conference, eds. J. C. Goldstein and B. E. Newnam (North-Holland, Amsterdam, 1992) p. 691.

* Work performed under the auspices of the U.S. Department of Energy by Lawrence Livermore National Laboratory under contract W-7405-ENG-48.

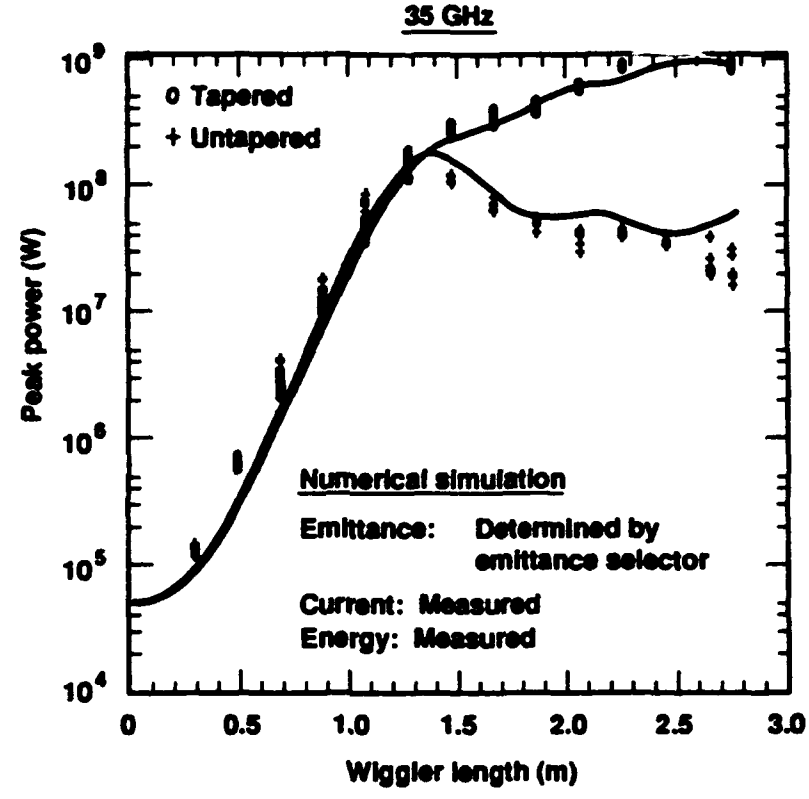

Fig. 1. 35-GHz power from ELF

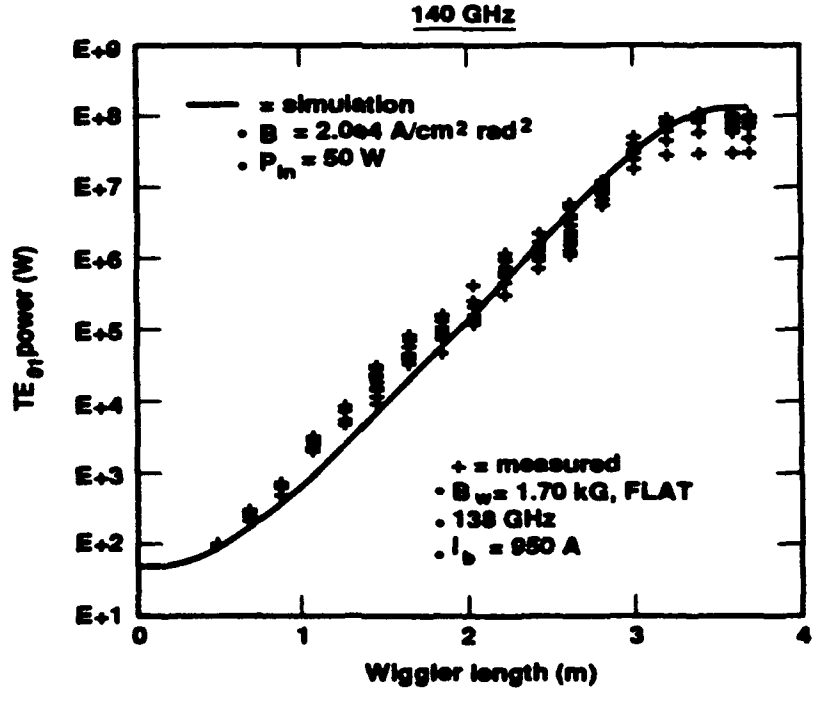

Fig. 2. 140-GHz power from ELF

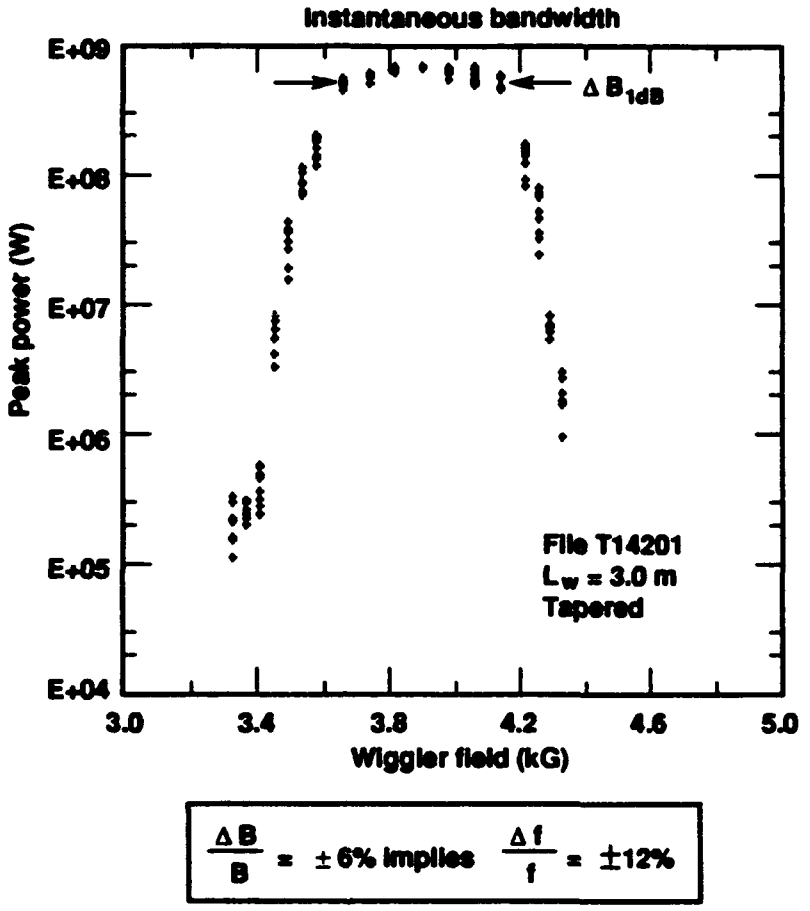

Fig. 3. 35-GHz bandwidth on ELF

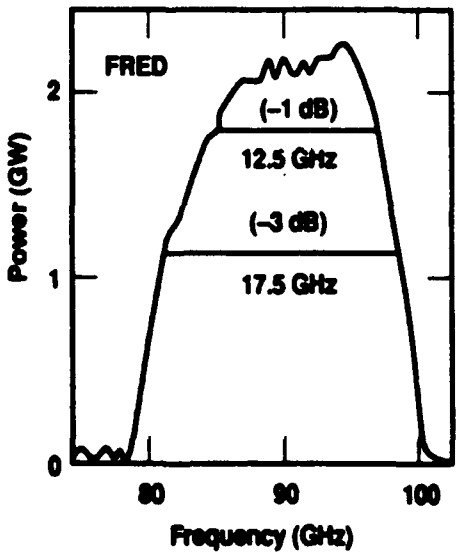

Fig. 4. Simulated 94-GHz FEL bandwidth

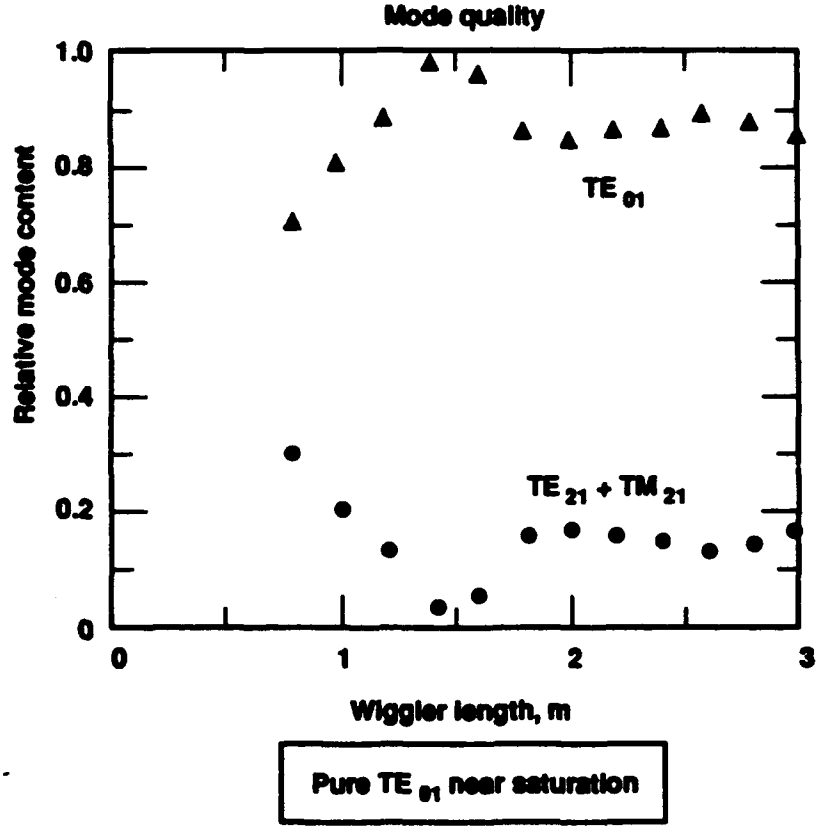

Fig. 5. 35-GHz mode content from ELF

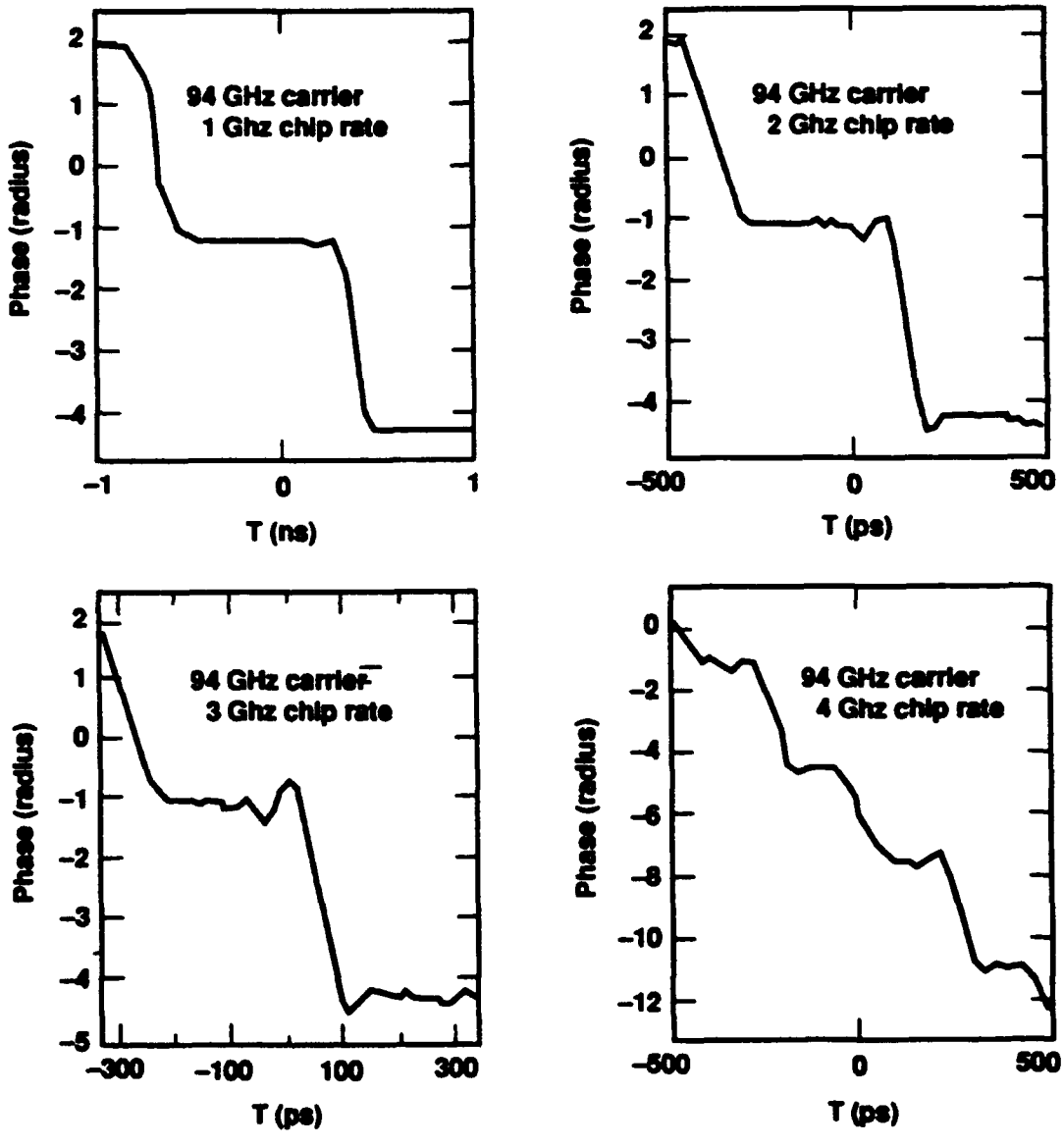

Fig. 6. Simulated amplification of 94-GHz biphase modulation

Creating and Keeping a Space Debris Catalog

Stephen H. Knowles
Naval Space Surveillance Center
Dahlgren, Va. 22448-5180

Introduction - The present space object catalog has undergone only slow growth from its initial size of one to its present size of approximately 7000 objects. As a result, a data handling capability has grown up that is sized to handle the present load, with little thought to possible expansion capability. There is now considerable thought being given to expanding this capacity by a large factor. This is being done for a variety of reasons, including collision protection for Space Station Freedom and for other space assets, as well as for possible debris-causing combat scenarios. It is known that the present system will have considerable problems handling an expanded catalog. This paper, however, will examine what is needed to handle a large space object catalog from first principles, since 'patches' to the existing computational and sensor system will almost surely not be adequate. The postulated catalog will be 250,000 objects, of size 1 cm. and larger. This represents an extreme case of what is considered necessary to meet requirements. It will be demonstrated that it is indeed possible for a catalog to fail if certain criteria are not met. On the other hand, initially creating the catalog is not as hard as is commonly thought. Basic performance required of the system is determined by the number of objects in the catalog and by exoatmospheric drag, which degrades the accuracy of orbits and requires periodic reobservation. Particular attention will be paid to strategies for creating the catalog from 'scratch', which must be done during initialization.

Catalog Creation - During the formation of a large space object catalog, it will initially appear that almost every object is unidentified, and appears as an 'uncorrelated target', or UCT. This prospect has caused apprehension in the surveillance community because normal UCTs pose such a performance challenge. There is a specific question that must be formulated and answered to judge the validity of such concerns. This question is: **is it necessary to correctly identify every object on its first pass through the debris sensor system, or can the catalog be constructed gradually?** In other words, can the system operate temporarily with a large number of targets that are unidentified/ignored, while keeping track of a gradually increasing number of identified targets,

or must (almost) everything be identified immediately. The author suggests that the catalog creation can indeed be done gradually, as long as a certain fundamental criterion is obeyed. This criterion is: **The accuracy of orbit determination at the first attempt must be sufficient so that the probability of correct identification at the next sighting is quite high.** Underlying this seemingly simple statement are the following factors

The distribution,and accuracy of sensors
Spatial density of catalog
Drag degradation of orbital accuracy

From this criterion follows a simple working rule, to wit: **the typical error in predicted arrival time of objects must be significantly less that the average arrival time interval.** If this criterion is satisfied, most objects will be reidentified correctly, and the catalog will be 'kept'. If this criterion is not satisfied, the catalog will fail due to a large number of misidentifications, and no cataloging will be possible. The spatial density and thus arrival time interval may be computed approximately for LEO objects by, for example, taking the actual or predicted catalog size and dividing by the approximate cubic volume of the LEO orbit range of about 300 to 800 km. In terms of population, the commonly accepted total LEO population is about *250000 for a catalog complete to 1 cm.*, and of course the baseline is a catalog of 7000 for objects 20 cm. in size or greater. The corresponding numbers are a spatial density spacing of about 1.5 km. for a 1 cm. catalog, and a mean interval of about 2 seconds between objects passing through a radar fence (the mean interval between passes through the present NAVSPASUR fence is about 10 seconds). This means that each object's pass time must be predictable to about 1 km., or 0.3 seconds, to enable correct identification (the discrepancy between these two numbers represents the uncertainty in the estimation methods used). If this criterion is satisfied, most object must be correctly identified and the catalog will work. Otherwise, it will fail.

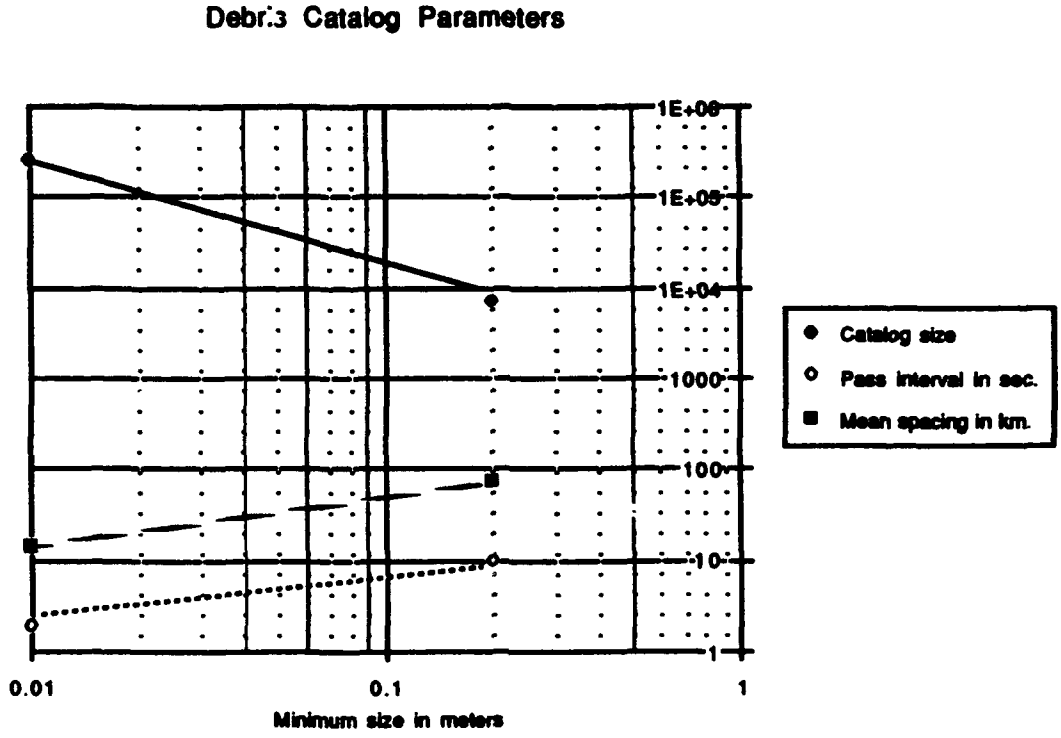

One important question concerns the probability of correct identification that is necessary in order to make the catalog work. It is clear from first principles of statistics that a 100% probability of correct identification cannot be obtained; the most that can be done is to identify possible contenders when they exist. Traditionally, the space catalog keepers have attached a very high importance to identifying each observation. However, it should be noted that much of this emphasis is for the military/political reason that says it is vitally important to have nothing up there whose provenance is unknown. While valid, this reasoning does not really apply to the keeping of a space debris catalog, which is applied as a statistical protection measure. To put it dramatically, a debris catalog can be kept in a sloppier fashion than a military/political related catalog, because it is not a major handicap if a few debris pieces are misidentified some of the time. This statement is important because it controls the real precision needed in orbit prediction. If a prediction confusion level of only 80% correct is acceptable, then an accuracy of about 0.25 of the mean interval is satisfactory. However, if a correct identification level of 99.9% is required, accuracy of a much smaller percentage of the mean interval is required. The exact numbers can be obtained from Poisson statistics. Thus, maintaining a

very high (but not 100%) correct reidentification level places a very severe stress on the prediction and observation required, and one that is probably not attainable. The author's opinion is that an accuracy level of 90 to 95 percent correct reidentification is probably satisfactory for reidentification in a space debris catalog. It must be recognized that this will inevitably result in a continual number of misidentifications, or UCTs, and that this will require the development of automatic procedures for dealing with this problem.

Now that the deceivingly simple question of the accuracy necessary to keep a catalog has been addressed, it is time to consider the related question of what requirements must be met to achieve this accuracy. In general, there are three factors limiting the accuracy of an orbit obtained from surveillance observations. These include sensor observation accuracy, propagator accuracy, and drag-related accuracy degradation. **Under normal conditions, the limitation in knowledge of atmospheric drag is the limitation that sets requirements on observation frequency for LEO orbits.** It is actually not the drag itself but the unavoidable error in the drag that sets limitations, normally dwarfing errors in the propagator and observation errors. Fig. x shows the typical atmospheric drag as as function of satellite altitude. This drag is a function of the ballistic coefficient of the satellite as well as being a very strong function of the orbital altitude. As is shown in figures 2 and 3, typical drag values for medium to large objects in the 300 to 600 km. altitude range are several kilometers per day (under quiet sun conditions), but can be much more. The most optimistic estimate of the accuracy with which the drag can be determined is +/- 15%; this means that an uncalibratable prediction error of several kilometers per day accumulated. This, combined with the catalog success requirement, means that **observations at least once daily of every debris piece are essential.** The mean drag delay for small debris pieces can be expected to be at least 3 times higher than the numbers given above for catalog object. The surface area to mass ratio, which controls ballistic coefficient, varies inversely as satellite diameter. This factor is somewhat compensated for by the fact that density can be expected to be higher for a debris piece because of the lack of void spaces present in a typical payload.

Drag Error
Most Favorable Solar Conditions

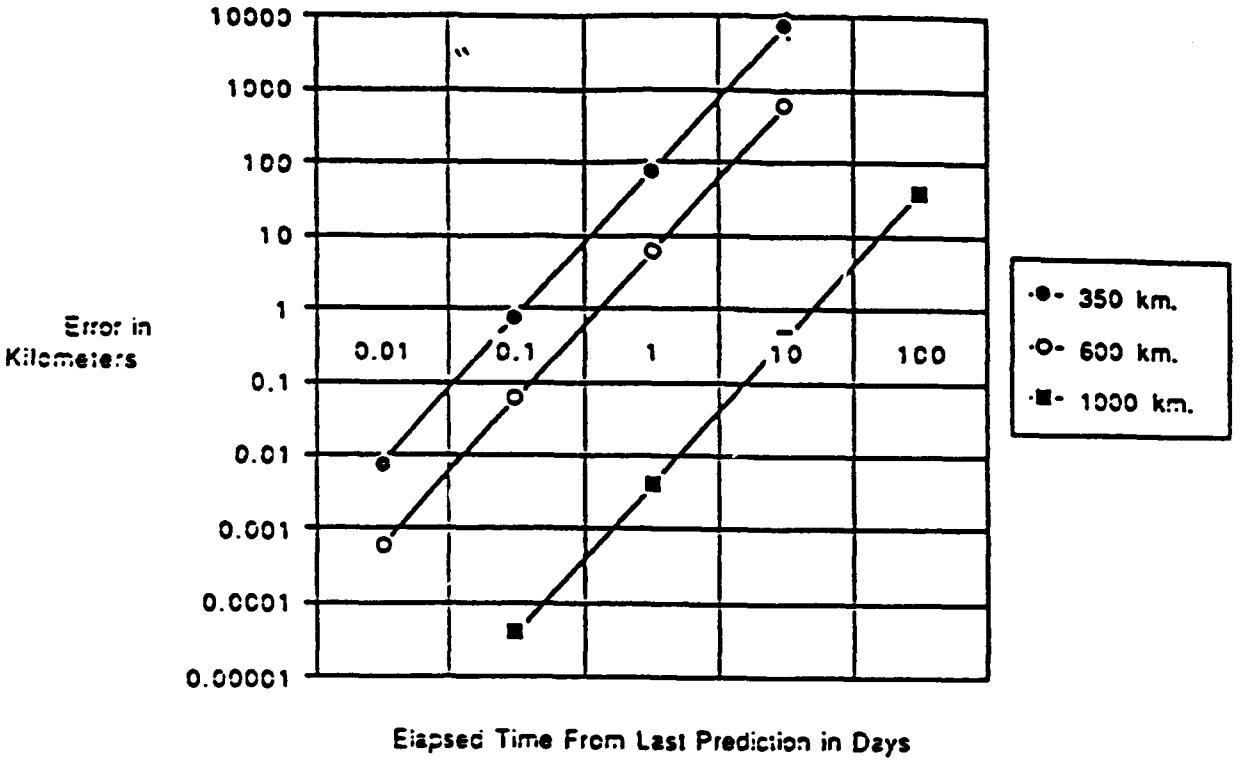

1-Day Drag Retardation for Typical 300-600 km. Objects

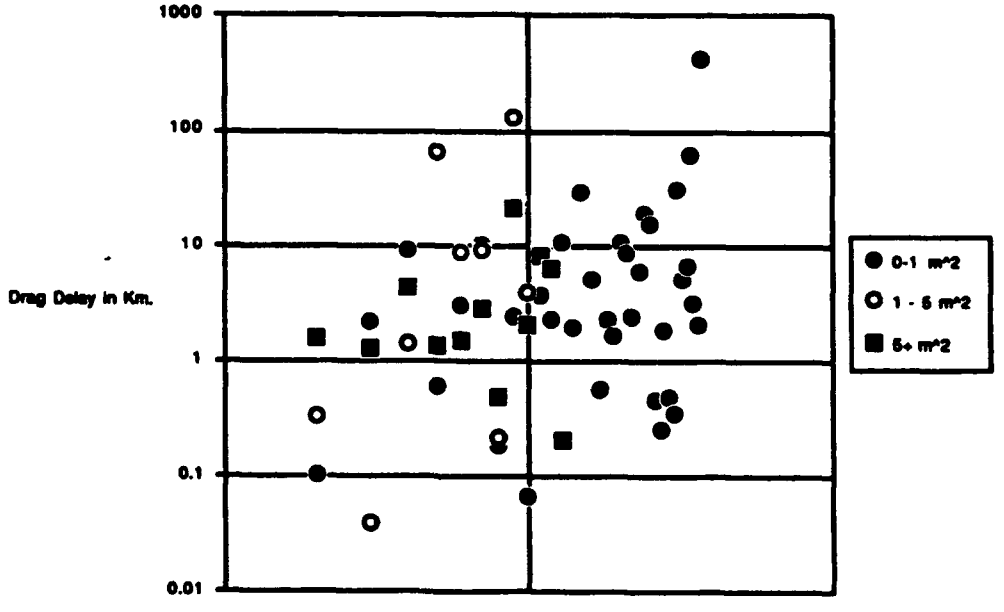

This daily observation requirement leads inevitably to the need for an unalerted sensor of a design similar to the NAVSPASUR radar fence as the backbone of a cataloging operation. The sensor system for a 1 cm. debris catalog will have to operate at frequencies of X-band or higher to avoid Rayleigh loss. However, phased-array designs for this frequency inevitably require a mechanical frame for full-sky coverage, which reduces both search and reacquire capability below the minimum necessary. An unalerted NAVSPASUR-type fence, however can be designed with the required sensitivity and capacity

The accuracy needed for effective collision prediction/avoidance is desirably very significantly better than customarily obtained for surveillance quality orbits. This is because any actual conjunction prediction to be used effectively postulate actually thrusting the target. This event is of moderate significance for any system, and for a target as complex as Space Station Freedom is clearly not undertaken lightly. Unfortunately the current prediction accuracies inevitably require a high ratio of unneeded maneuvers for every needed maneuver, because the prediction error ellipse is much larger than the physical size of either object. If the number of 'false alarms' is too great, collision/conjunction prediction s will inevitably be ignored. Fig. 4 is an indication of the number of false collision predictions for each real prediction for a space station postulated to be 30 meters in size, and assuming a 5:1:1 ratio error ellipsoid. It will be seen that when the along-track error is greater than about 500 meters, the number of false alarms for each real danger situation is such as to discourage use of this protection tool. Thus , the debris catalog mandates the difficult requirement of **achieving 500 meter along-track accuracy or better for prediction spans of up to 1 day in advance.**

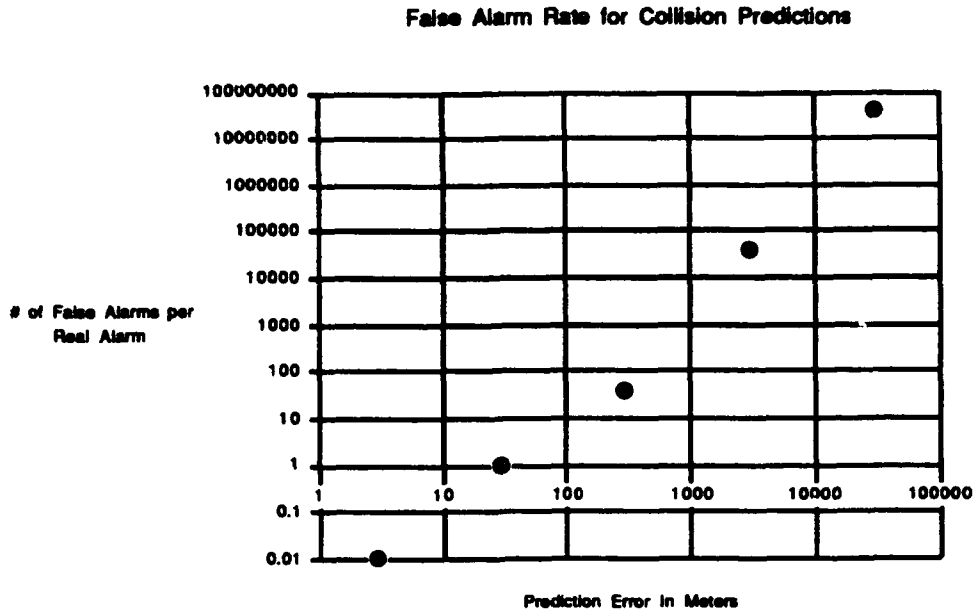

Computational Requirements - The computational power required is obviously a function of the catalog size. Present computers are 'barely able to handle the catalog'; but this is primarily because they have been sized to handle the problem. There are now machines available of much higher capacity, and the appropriate question is an economic one: how much computing does it take to do the job, and how much will the appropriate machine cost? As a baseline, computing differential corrections for 7000 objects now takes NAVSPASUR about 3 hours on a 5 megaflop Control Data Cyber 760 (1 megaflop = 1 million floating point operations per second). This amounts to 2.5 million floating point operations per differential correction (flop-seconds). Thus, a differential correction for a 250,000 object catalog would take about 65 gigaflop seconds, which means that it could be accomplished by a 2 gigaflop machine in about 1 minute. For the minimum postulated working size of the Space Station catalog of 5000, only a small increment in computer power is needed. Table I shows some other examples of computer 'horsepower' needed. The 2 GHz example machine used is a Connection Machines CM-200 with 8K nodes. This is typical of a 'run-of-the-mill' current generation parallel processor. More powerful machines are now available.

Table I

Computational Requirements for a Space Debris Catalog

Application	Total computation in flopsec	Time req. on 5 Mflop frame	
Differential correction on 7000 object catalog, using GP	5 x 10^10	180 min.	30 sec.
Differential correction on 250000 object catalog, using GP	2 x 10^12	107 hr.	16 min.
Differential correction on 25000 object catalog using SP	2 x 10^13	1070 hr.	2.7 hr.
36 hr. COMBO prediction, 1 against all	6 x 10^9	20 min.	80 sec.
36 hr. COMBO prediction, all against all	4 x 10^13	97 days	6 hr.

Conclusion - Some relatively simple fundamental criteria for a debris catalog are set forth. It is technically feasible to track all LEO debris down to a size of 1 cm. However, the economically attractive approach of modifying existing assets will not work well because of the higher sensitivity and larger catalog size needed. To somewhat balance this factor, a debris network will not require the high degree of redundancy present in the current defense-related network.

ORBITAL DEBRIS ENVIRONMENT : RECENT RESULTS

Phan D. Dao, Bill Borer, and Alex M. Wilson
Phillips Laboratory, Geophysics Directorate
Hanscom AFB, MA 01731

ABSTRACT

The Air Force Phillips Laboratory is undertaking a concerted effort to assess the debris environment by measurement and modeling. Measurement of orbital objects with optical telescopes operated by MIT/Lincoln Laboratory in Socorro, New Mexico, and Phillips Laboratory, Laser and Imaging Directorate, in Maui, Hawaii and the NASA-sponsored debris Haystack radar has resulted in a wealth of data on eccentricity, semi-major axis and inclination distributions. The observed distributions are not in complete agreement with that of the radar-based catalog. The differences could result in a profound revision of the projected collision fluxes. This paper reviews the observations and presents an analysis of the observed differences in an attempt to model them in using simple sensor and collision flux models. We also attempt to simulate the environment using historical data of past break-up events and compare the results with observations.

RESULTS OF STARE AND CHASE DEBRIS SEARCH AT THE EXPERIMENTAL TEST SYSTEM

E.C. Pearce, M.S. Blythe, D.M. Gibson, and P.J. Trujillo (MIT Lincoln Laboratory)

ABSTRACT

Since May 1991, MIT Lincoln Laboratory's Experimental Test System has been performing a unique series of optical debris measurements. The first phase of the observing program developed the ability to detect, track, and generate accurate element sets for debris sized objects. Using these techniques, a series of unbiased "stare and chase" searches were started in 1992 and continue to date. For the first time, this program has allowed detailed analysis of the uncataloged debris population.

Initial results indicate that uncataloged debris are tightly distributed near traditional operational inclinations. However, the orbital distribution in eccentricity differs significantly from that of the Space Surveillance Catalog. Specifically, a much higher fraction of debris occupies moderate and high eccentricity orbits.

The ETS has a unique ability to detect, acquire, track, and maintain a catalog of faint debris. Further, its capability to do multicolor, high-speed photometry allows detailed study of the physical properties of uncataloged objects. Accurate estimates of the size, rotation rate, drag coefficient, albedo, and composition for individual debris objects have been made. Thus, properties of the cataloged and uncataloged orbital population can be compared.

1. INTRODUCTION

Currently, more than 7000 cataloged objects reside in Earth orbit. Only about 500 of these objects are cataloged as active satellites. Nearly half of these objects are cataloged as orbital debris and an additional 1000 objects are discarded rocket bodies. More importantly, these statistics do not include the uncataloged debris population with sizes between 1 and 10 cm. These objects are too small to be tracked by the Space Surveillance Network (SSN), but would cause catastrophic damage if one were to collide with an operational satellite or manned spacecraft. Unfortunately, the extent and distribution of the 1-10 cm debris population is still not well determined from observational data.

Starting in late 1990, MIT/LL conducted a second "staring" survey at the request of the Air Force Phillips Laboratory (PL). In this survey, both ETS 80 cm (31") telescopes would stare at the same position near the zenith during twilight. Objects passing through the field of view were recorded on video tape. Special emphasis was placed on developing techniques to monitor the photometric conditions of the sky throughout the observing period. For this survey, both telescopes stared at the same selected Guide Star Photometric Catalog (GSPC) [1] field near the zenith. Photometric analysis of the video tapes allowed continuous monitoring of the transparency and brightness of the sky. These techniques allowed the observational bias against smaller objects to be precisely determined and removed from the survey data. Now, these techniques are an integral part of all the PL coordinated optical debris observations. A total of 32 hours of dual-telescope data was acquired from November 1990 to March 1991.

In May 1991, MIT/LL began the current optical debris measurements program under the direction of Phillips Laboratory. This program was part of a Phillips Laboratory organized effort to search for and track space debris in support of the DoD effort to characterize the space environment [2]. Ideally, the debris environment would be characterized optically down to a size of a few centimeters. An additional program requirement imposed by Air Force Space Command (AFSPACECOM) was to specify debris orbital element sets. Consequently, the new effort is unique from the previous programs outlined above.

The first phase of the new MIT/LL observing program was designed to demonstrate the ability to detect, track and generate accurate element sets for detected objects. The searches targeted specific sun-synchronous debris clouds, including the NIMBUS-6 rocket body breakup. These clouds range in altitude from 500 to 1500 km. In order to achieve maximum sensitivity, all searches used a technique called "pseudo-tracking." When searching in this mode, the telescope tracked along the orbit of previously cataloged debris cloud members. When an object was detected, the operator would manually acquire and track the object. Once acquired, the object would be tracked to the horizon, generating enough astrometric ("metric") data for an accurate orbit determination. During 25 hours of observing, orbits were determined for eight previously uncataloged objects.

The pseudo-tracking searches successfully proved that uncataloged debris objects could be acquired and tracked. While the pseudo-tracking search mode enhanced sensitivity greatly, it also biased the search volume significantly. Thus, in February 1992, the ETS initiated a new series of debris observations. For this series of observations, the ETS 80 cm telescopes would stare at different selected GSPC fields. However, instead of simply recording and measuring streaks, detected objects were acquired and tracked. Thus, the new "stare and chase" observations combined the best features of both the high-volume staring search and the pseudo-tracking searches.

This paper documents the methods and results of the first eight months of the stare and chase debris searches at the ETS. An analysis of the orbits of all detected and tracked objects has been completed, along with a correlation of all detected objects against all cataloged satellites and Space Surveillance Center (SSC) analyst satellites. Additionally, the orbital distribution of the newly tracked debris will be compared to the currently cataloged population.

2. THE INSTRUMENTATION

Lincoln Laboratory's Experimental Test System (ETS) is located in southern New Mexico on the northwest corner of the White Sands Missile Range. The site was originally constructed in 1975 as a prototype for the Ground Based Electro-Optical Deep Space Surveillance (GEODSS) system. Only the instrumentation relevant to the debris observations will be discussed here.

The primary instruments at the ETS are twin 80 cm telescopes mounted on Boller and Chivens German Equatorial mounts. For the debris observations, one of the two telescopes is operated in a f/5 Cassegrain configuration while the other is operated in a f/2.87 prime focus configuration (only one telescope is currently capable of operating at prime focus). Typically, the Cassegrain configuration offers a 1.0° field of view while prime focus offers approximately 2.0°. Thus, the prime focus telescope offers a significantly larger field of view, increasing the detection rate and facilitating object acquisition.

Westinghouse intensified electron-bombarded silicon diode array cameras (I-EBSICONs) were used exclusively [3]. The I-EBSICON cameras utilize a large 80 mm fiber-optic faceplate, allowing full coverage of the telescope focal plane while the intensifier stage provides a significant sensitivity

enhancement in comparison to the unintensified GEODSS cameras. The cameras are sensitive enough to provide sky background limited performance at RS-170 video rates.

Each telescope is controlled by a dedicated, distributed computer system comprised of four Motorola 68020 and 68040 single board computers on two VMEbuses. Most higher level control functions are performed by a pair of Motorola 68040 single board computers. Lower level functions, such as servo loop control, are performed on a pair of Motorola 68020 single board computers. The system provides a robust control system capable of tracking objects in a variety of modes. Objects can be tracked using several propagation models, including SSC SGP4 or MIT/LL ANODE or ANODE-R, manually under joystick control, or with an DBA Systems video tracker. The versatility of this control system has proved to be a key element in the success of the program.

3. OBSERVING METHODOLOGY

3.1. Scheduling Considerations

Since the goal of the observing program is to detect and track objects at altitudes between 500 and 1500 km, observing was scheduled to take place during the twilight periods. During this time, the objects are illuminated by sunlight, but are observed against a dark sky. Most sessions took place during evening twilight. In the evening, observing began at nautical twilight (at an unrefracted solar depression angle, $E_\odot = 12°$) and continued for one hour. Typically, the end of the session occurred about 30 minutes after astronomical twilight and at a solar depression angle of $E_\odot \approx 24°$. Thus, at the beginning of the observing session, the earth shadow height at the zenith would be 132 km. By the end of the session, the shadow height climbed to approximately 600 km.

Later in the program, the evening twilight stare fields were moved approximately 20° of right ascension east of the zenith. The elevation of the field was typically 70-80° at the end of the stare period. With the stare fields further east, the typical second pass geometry of detected objects was much better (since the second pass would now be higher in the west by a corresponding amount). Thus, the opportunity to reacquire objects was greatly enhanced. The costs in terms of increased shadow height, air mass, and object range were negligible in comparison.

3.2. Search and Acquisition Procedures

During the observing session, both telescopes were positioned on the selected GSPC fields. These fields were selected so that they contained sufficient background stars to provide both an astrometric and a photometric reference. (GSPC fields have between 5 and 7 reference stars over a 0.5° field.) Fields with unusually bright stars were avoided to eliminate camera saturation. Since previous studies and the orbital distribution of cataloged debris imply an enhanced population in high inclination orbits, the two stare fields were selected to be offset in right ascension [4]. Thus, the two telescopes' fields of view formed an incomplete fence with minimal overlap for the populous near-polar orbits.

When the telescope operator detected an object crossing the field of view, the operator used an acceleration joystick track mode, combined with a video tracker, to acquire and track the object. The special acceleration joystick mode was developed specifically for this program to facilitate the manual acquisition of the objects. In this mode, the joystick displacement is translated directly into commanded accelerations of the telescope drive axes. Once a coarse track was established with the joystick, the video tracker would lock onto the object and establish precision track.

Once precision tracking was established, the object was correlated against the SSC catalog of space objects. If the object did not correlate to a known object, metric data would be taken on the

object for the remainder of the visible track. Typically, this would result in a 3 to 5 minute track on the object and allow reasonably accurate initial orbit determination.

After tracking an uncorrelated object, a sequence of four GSPC fields at airmasses from 1.0 to 3.5 were observed. These fields provided an all-sky photometric calibration. With this photometry, taken from the video tapes, and the solar illumination angle reconstructed from the determined element set, an accurate estimate of the object's size-albedo product was possible.

3.3 Reacquisition and Subsequent Tracking

One of the significant advantages of the stare and chase technique is the ability to determine element sets for the detected objects. The element sets derived from a single pass of the satellite are more than adequate for studying the orbital distribution of debris and represent a significant improvement over the inclination and mean altitude determined from previous streak measurement techniques. However, determining an element set accurate enough to track the object on future passes is not as straight forward as simply tracking the object for a single pass. Metric data from the initial track ("rev zero"; subsequent post-discovery passes are referred to by successive cardinal numbers) alone is not sufficient to establish such an element set. Typically, the initial element set will have a well determined inclination, i, and right ascension of the ascending node, Ω. However, the mean motion, n, and eccentricity, e, will be relatively poorly determined, causing a significant along orbit error in the predicted position at later epochs. In order to reacquire the object on its first post-discovery pass, rev one, an along orbit search covering from ± 1 to ± 5 minutes along orbit is required, depending on the quality of the zeroth pass data and the length of the track.

The extent of the along orbit search required on the first pass is too large to allow a pseudo-tracking search to be employed. Instead, a special along orbit stare search has been developed especially for the first pass reacquisition. In this search mode, the telescope first begins tracking on the initial element set. Then, a positive time bias is introduced, causing the telescope to track several minutes ahead in the orbit. The telescope is then frozen in the along orbit direction and the operator waits for the object to streak across the field of view. Notice that during this time, the telescope is actually tracking a fixed point in an Earth centered inertial (ECI) coordinate system. When the object is detected, the observed along orbit error is used to adjust the mean motion of the initial element set, the time bias is removed, and the telescope begins to track the object.

With the additional metric data from rev one, the initial element set can be updated, improving its quality dramatically. Typically, the newly determined orbit will be accurate enough to allow reacquisition on the following night (rev 12-15 depending on the object's period) with a brief search spanning less than a minute in time along orbit. After approximately 5 days of data have been obtained, the object's orbit can be easily maintained until it drifts out of the site's twilight visibility. During this time, detailed visual, infrared, and radar observations could be made on the object from other collaborating sensors.

4. RESULTS

4.1. Summary of Observing

This section summarizes the results of eight months of observing from February to September 1992. Typically, 10 evening sessions per month were scheduled, beginning near the third quarter moon and extending to shortly after new moon. Due to the summer monsoon season in the Southwest, no observing was scheduled during July. During these eight months, a total of 37 hours of data were collected with two telescopes. A total of 336 objects were detected, of which 140 were

previously uncataloged objects. Enough metric data was acquired on 24 uncataloged objects (called uncorrelated targets or UCTs by the SSN) to allow accurate orbit determination.

4.2. Inclination Distribution of Debris

The inclination distribution of the detected UCTs is shown in Figure 1. It is clear that the uncataloged objects are tightly concentrated into discrete orbital planes. For comparison, the distribution of all cataloged objects is shown in Figure 2. In Figure 2, only objects with i > 33.82, the latitude of the ETS, are shown. Note that with a zenith stare search, only objects with an inclination equal to or greater than the site's latitude are observable. Both histograms are scaled in units of object density per unit inclination, allowing direct comparison of the two distributions.

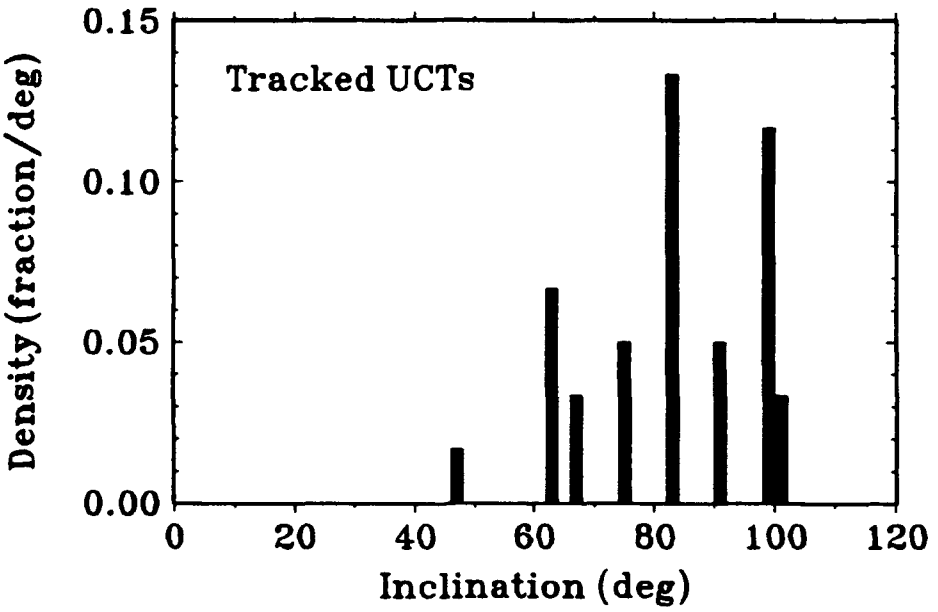

Figure 1. Inclination distribution of tracked UCTs.

Concentrations in the distribution are apparent at inclinations of 63°, 74°, and 83°. Each of these planes corresponds to Soviet satellite constellations. Specifically, 63° is used by Soviet Molniya and early warning satellites, 74° by low altitude communication satellites, and 83° by a variety of communication, navigation, and surveillance satellites. Moreover, each of these orbital planes has been plagued by numerous breakups. The breakup of Cosmos 1275 at an inclination of 82.96° is the most notable example. The 63° plane is littered with at least 14 breakups of Cosmos 862-class satellites [5]. Typically, debris from this class of breakup is poorly tracked since perigee occurs consistently in the Southern Hemisphere. Not surprisingly, a large percentage of the tracked UCTs near 63° inclination have eccentricities larger than 0.15. These objects could be decayed debris associated with Cosmos 862-class breakups.

Figure 1 also shows a large enhancement in the debris population between 98° and 102°. These orbits, with altitudes between 700 and 1500 km, are sun synchronous. Sun synchronous orbits are designed to maintain near constant solar illumination angles along the satellite ground track.

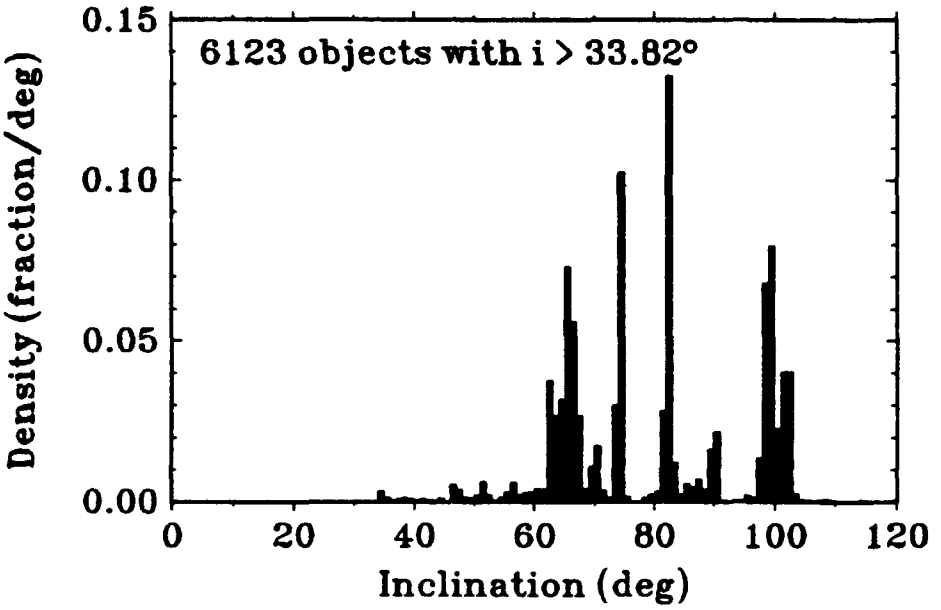

Figure 2. Inclination distribution of cataloged objects.

These orbits are used predominately by a variety of US and European Space Agency (ESA) payloads. Sun synchronous orbits are also littered with the debris from 11 major debris events, mostly Delta upper stage rocket body breakups. A comparison of Figure 1 and Figure 2 shows a larger ratio of uncataloged to cataloged objects in this inclination range than for the catalog as a whole. A previous pseudo-tracking search by the ETS of the sun synchronous NIMBUS-6 debris cloud implied 4:1 ratio of uncataloged to cataloged objects in this cloud in the 2-40 cm size range.

The final inclination band shown prominently in Figure 1 is near 90°. All of the detected UCTs in these polar orbits are attributable to the breakup of the US payload Snapshot (SSC 1314, 1965-027A). Currently, there are 62 cataloged objects associated with this fragmentation. The average cloud member has a period of 111 minutes and a height of 1278 km. Although it would appear from Figure 1 and Figure 2 that the uncataloged ratio is also higher than average near 90°, this is probably an artifact. Because of the near polar inclination of this cloud, the differential precession of the ascending node is very small. Consequently, the cloud is still concentrated over approximately 20° in right ascension (Ω) and visibility of the cloud at the zenith during twilight occurs in a narrow window twice annually.

4.3. Eccentricity Distribution of Debris

Preliminary results of the eccentricity distribution are also interesting. Figure 3 shows the eccentricity distribution of the tracked UCTs while Figure 4 shows the distribution of all cataloged objects. Again, only objects with inclinations greater than the latitude of the ETS (33.82°) are shown. Once again, the figures are scaled so that they are directly comparable. Although the sample size is small, there is a significant tendency for the uncataloged objects to have higher

eccentricities than the catalog in general. In particular, the number of "moderate" eccentricity (0.1 to 0.4) is enhanced.

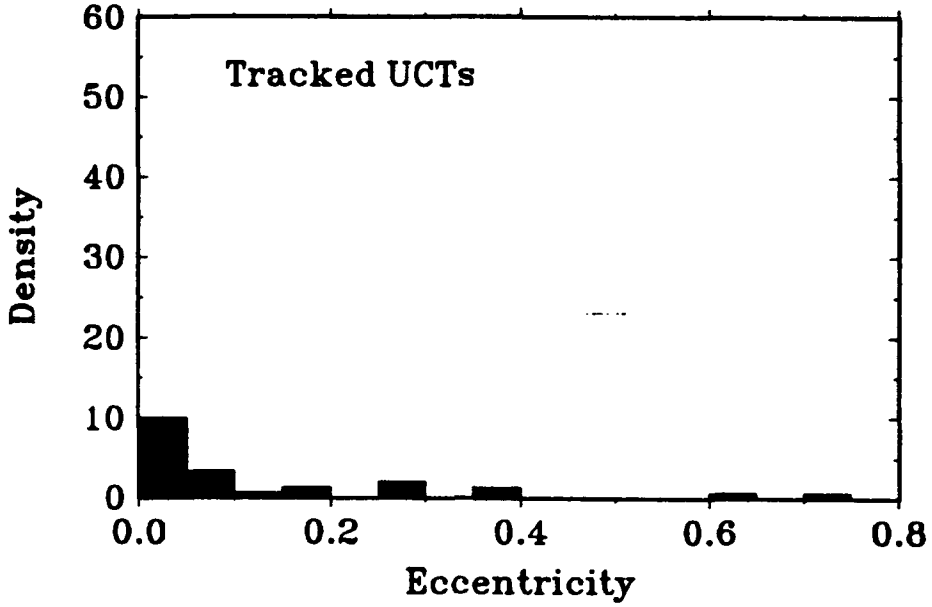

Figure 3. Eccentricity distribution of tracked UCTs.

There is reason to believe that moderate and high eccentricity orbits are under-represented in the catalog. First, objects in elliptical orbits are difficult to track by the SSN since they may be detectable only along a fraction of their orbits near perigee. Since perigee tends to occur at the same latitude on each revolution, it may also be difficult to track the object with multiple sites. This problem is particularly acute at inclinations where the rate of argument of perigee precession is low, such as 63.4°. Most of these moderate eccentricity objects are likely to be partially decayed transfer orbit debris, launch hardware from early warning and Molniya satellites, and, as we saw in the last section, uncataloged Cosmos 862-class debris.

Recently, data from other sources also indicated the possibility of a large population of uncataloged moderate and high eccentricity debris. Results from impact studies on NASA's Long Duration Exposure Facility (LDEF) have shown a significant number of impacts on the trailing surface to be of manmade origin [6]. Only highly elliptical, low inclination orbits could be responsible for these impacts.

4.4 Supplementary Analysis of Tracked Objects

One of the fundamental aspects of the stare and chase techniques is the opportunity to take supplementary data on the discovered objects. Thus, detailed visual, infrared, and radar observations can be made on these uncataloged objects. The supplementary observations can be used to characterize the object's size, color, albedo, and rotational period. Ultimately, these measurements will allow determination of what physical traits, other than small size, distinguish

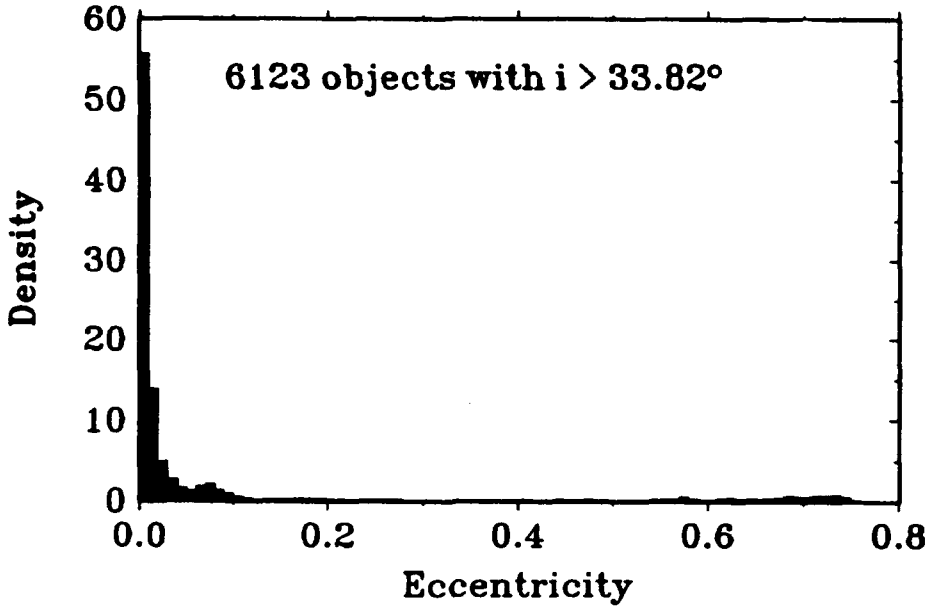

Figure 4. Eccentricity distribution of cataloged objects.

measurements will allow determination of what physical traits, other than small size, distinguish uncataloged from cataloged objects.

Although a complete discussion of these measurements is beyond the scope of this paper, some sample observations of a single object will be presented briefly as an example. This object, known internally as ETS 97034, was first tracked on 22 September 1992 (92:267) and was successfully reacquired on rev one, only 46.32 s behind the initial rev zero element set. Ultimately, after several more tracks over the next nine evenings, a highly accurate element set was determined for the object. The object was in a 1094×1020 km orbit at an inclination of 99.36° and a period of 106.34 min. Orbital analysis over the next 80 days showed that the semi-major axis of the orbit was decaying at the unusually high rate of 3.48±0.05 m/day (see Figure 5). Using the element set determined by the ETS, the object was later tracked by the Maui GEODSS, the Air Force Maui Optical Station (AMOS), and the MIT/LL Millstone Hill Radar.

ETS 97034 is probably related to the breakup of the NIMBUS-6 rocket body on 1 May 1992. It is interesting to note that the object is a member of a "cloudlet" of seven very tightly spaced objects within the larger cloud. In fact, two of the objects in the cloudlet are still on the same revolution, even though the breakup occurred over 500 days ago.

High speed optical photometry was taken on the object at the ETS using a 1 kHz Gallium-Arsenide photomultiplier tube (GaAs PMT). As can be seen from Figure 6, the object is highly specular, with two flashes per rotation. A rotational period of 0.4798 s can also be deduced from the data. Additionally, the two specular beams are 10.5° out of alignment and are not simply reflections from two sides of a flat plate. Typical specular flashes for ETS 97034 reach a visual magnitude of 8.0, however, flashes as bright as 6.0 have been observed in ideal geometries. Between flashes, the object is less than 14 magnitude. The events are have a duration of only 3-4 ms,

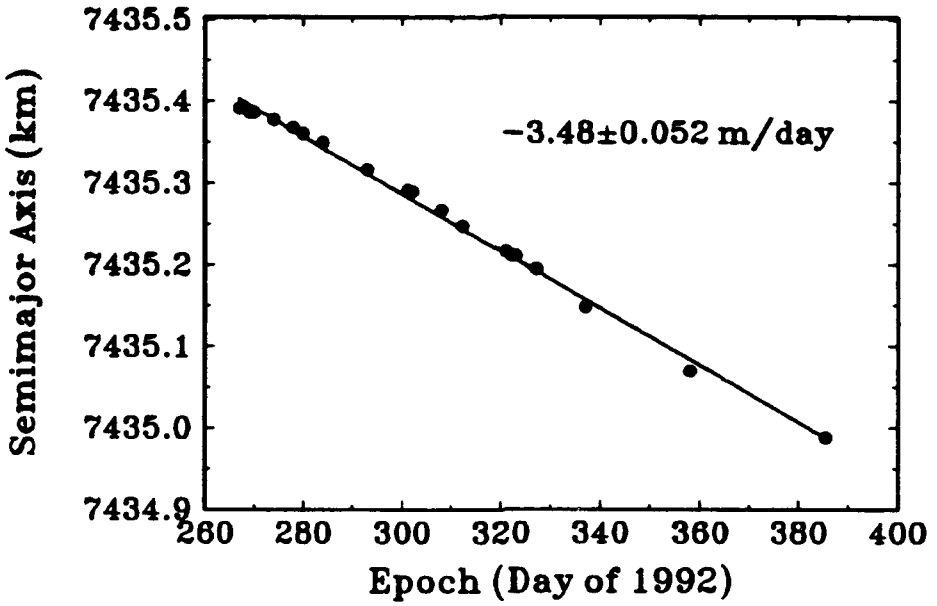

Figure 5. Orbital decay of object ETS 97034.

indicating a beam width of approximately 6°. Apparently, the reflections are from two nearly flat surfaces of a highly reflective material. By assuming a 0.5 albedo (typical for a highly reflective aluminum surface), a reflecting area of approximately 50 cm is indicated.

The object has also been tracked at L-band by the MIT/LL Millstone Hill Radar. At L-band, the object shows similar short period variations in RCS. The L-band RCS varied from -15 to less than -40 dBsm (320 to 1 cm^2). Interesting, the mean RCS, averaged over several rotations of the object, also showed significant variations over the pass. Mean RCS varied from -19 to -32 dBsm (125 to 6.3 cm^2). These RCS values are roughly consistent with the observed visual magnitude. However, it is incorrect to assume a direct relationship between RCS and physical size.

5. CONCLUSION

The magnitude and evolution of the orbital debris hazard are still subjects of controversy. The primary reason for the controversy is the lack of reliable estimates for the distribution and characteristics of objects in the size range from 0.1 cm to 10 cm. Because of the difficulty in measuring the debris environment in the sub-10 cm size range, it is common to assume that the orbital distribution and physical properties of small debris are similar to the cataloged population. The ETS has developed a number of new observing techniques leading to the detection and reacquisition of previously uncataloged debris. The new techniques permit determination of both accurate orbital elements and the physical properties of small uncataloged objects and will allow the validity of these assumptions to be evaluated.

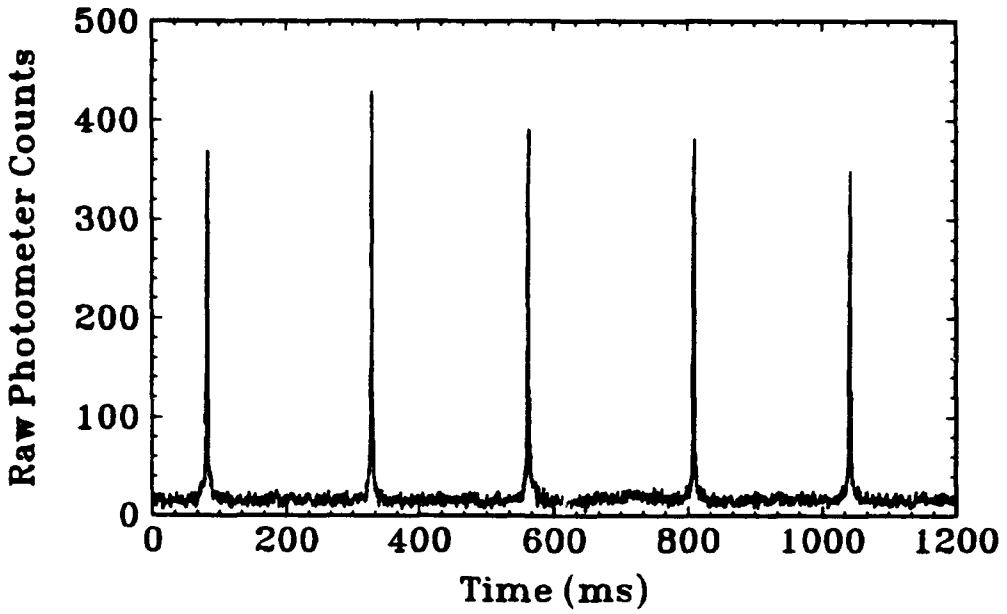

Figure 6. High speed photometry of object ETS 97034.

ACKNOWLEDGEMENTS

This program would not have been successful without the support of the dedicated people of the ETS. In particular, we thank our observers, Bob Irelan and Debbie Borden, our software staff, Frank Shelly and Julie Johnson, and Ed Johnson for porting ANODER-R to the ETS computer systems.

REFERENCES

1. B.M. Lasker, C.R. Sturch, *et. al.*, "The Guide Star Photometric Catalog. I.," *Astrophys. J. Suppl.*, **68**, 1, pp. 1-90 (September 1988).
2. A.E. Reinhardt, "Potential Effects of the Space Debris Environment on Military Systems," presented at Preservation of Near-Earth Space for Future Generations, University of Chicago (June 1992).
3. R. Weber, "Large-Format EBSICON for Low Light Level Satellite Surveillance," *Optical Engineering* **20**, No. 2, 212-215 (March/April 1981).
4. L.G. Taff and D.M. Jonuskis, "Results and Analysis of a Bi-Telescopic Survey of Low Altitude Orbital Debris," *Adv. Space Res.* **6**, 7, pp. 131-137 (1986).
5. N.L. Johnson and D.S. McKnight, *Artificial Space Debris*, Malabar, Florida: Krieger (1991).
6. D.J. Kessler, "Origin of Orbital Debris Impacts on LDEF's Trailing Surfaces," NASA CR (in press).

Orbital Debris Characterization Measurements at the Air Force Maui Optical Station (AMOS)

P W Kervin, S D Kuo, R Medrano (Phillips Laboratory), J L Africano, J V Lambert (Rockwell International), K E Kissell (Rockwell Power Systems)

The Air Force Maui Optical Station (AMOS) is conducting searches, measurements, and analyses of orbital debris for Air Force Space Command and the Phillips Laboratory (PL) in support of the Air Force Orbital Debris Measurements Program. The objective of this program is to detect orbiting objects not currently in the United States Space Command Space Surveillance Center (SSC) catalog. Once detected, further objectives are to track, catalog, and maintain those objects locally, to determine statistics on detected objects, and perform relevant analyses. In addition to this surveillance activity, AMOS is also automating the detection and analysis process, and developing a prototype surveillance system for detection of orbital debris. The AMOS program is a joint effort between various government and contractor agencies to employ the wide field of view optical sensors at the Groundbased Electro-Optical Deep Space Surveillance (GEODSS) site at the Maui Space Surveillance Site (MSSS) and narrow field of view tracking sensors at AMOS (which is also located at the MSSS).

There are several partners in this program. Air Force Space Command provides the funding and the direction for the program. Phillips Laboratory in New Mexico provides the program management, as well as simula and analysis, as does its Geophysics Directorate in Massachusetts. The Lasers and Imaging Directorate of Phillips Laboratory provides the search, measurement, and analysis capabilities using its AMOS facility in Hawai'i. Rockwell Power Systems (RPS) is the prime contractor for the AMOS facility, with additional support from Rockwell International. The prime contractor for the GEODSS facility is Planning Research Corporation (PRC). In addition, Massachusetts Institute of Technology/Lincoln Laboratory (MIT/LL) provides PL with capabilities similar to that of AMOS, at the Experimental Test System (ETS) in New Mexico. The success of this program depends quite heavily on the support and cooperation of all of these organizations.

A wide variety of equipment and resources are available to the Orbital Debris Measurements Program. The optical assets include a multitude of sensors and mounts at both the MSSS as well as Diego Garcia. The optical assets at the MSSS include a total of eight telescopes on seven mounts, with a wide range of associated sensors. A brief description of the MSSS assets is shown in Table 1. Note the availability of visible and infrared photometric sensors, imaging sensors, and video capability. Video equipment is available both at the MSSS, located at the 3,000 meter summit of Mt Haleakala, as well as the support facility located at sea level in the town of Kihei. A broad range of computer equipment is also available. The platforms most commonly used in support of the program include products from Silicon Graphics, Sun, Datacube, and Macintosh.

MSS OPTICAL ASSETS

TELESCOPE	APERTURE (m)	SENSOR	RESPONSE (μm)
1.6	1.596	AATS	.4-.8
		CIS	.4-.8
		PHIAT	.35-1.0
		PtSi Array	1.2-5.9
		ASR	1-30
		Boresight TV	.4-.8
		ELSI	2.2-5.5 8-13.5
1.2 (829)	1.219	MATS	.4-.8
		AMTA	3-23
		CMP	.3-.92
		Boresight TV	.4-.8
1.2 (837)	1.219	MAIS	.4-.8
		LLLTV	.4-.8
LBD	0.635	Boresight TV	.4-.8
BD/T	0.815	BATS	.4-.8
		Boresight TV	.4-.8
GEODSS Main	1.01	Video	.4-.8
GEODSS Aux	0.38	Video	.4-.8

Table 1

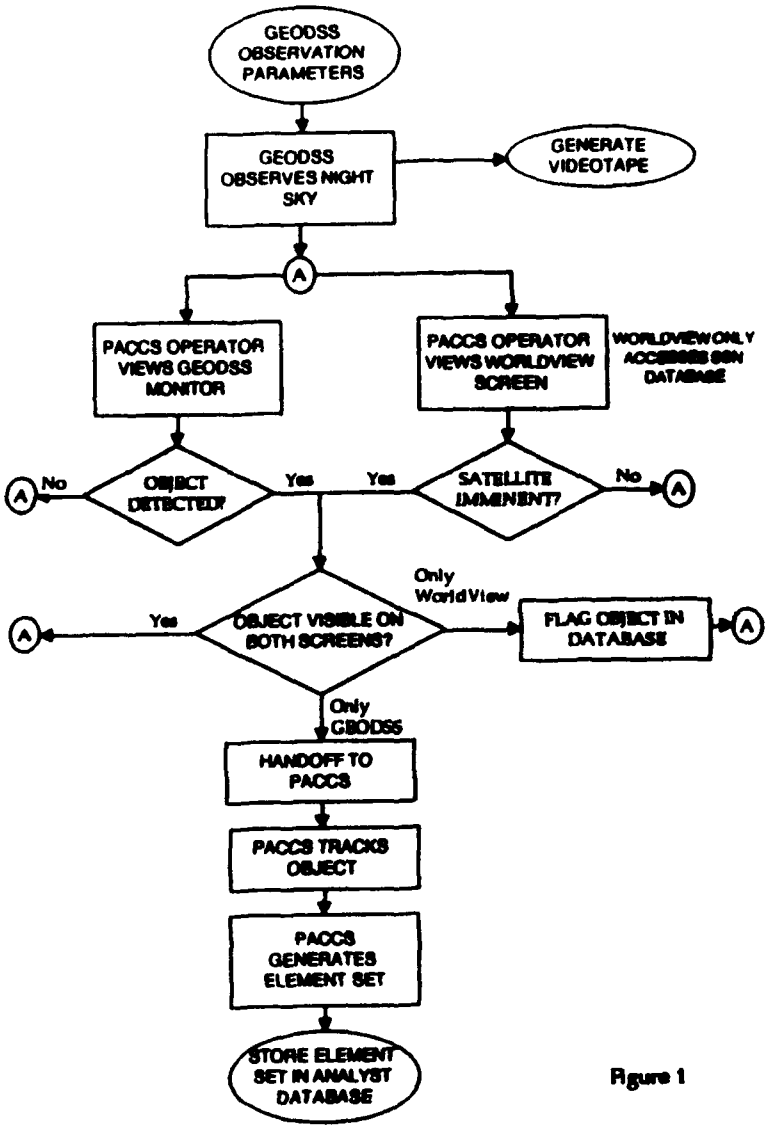

Figure 1

The operational goals of this program are to detect, track, catalog, and maintain new objects. During real time operations, only the detect and track goals are achieved. During post-processing, all goals are either achieved or supported. It is therefore appropriate to describe the operations in sections which address these types of operations.

The most appropriate sensor at the MSSS for the detection process is the sensor with the widest field of view. The sensors which vie for sensor-of-choice are the two GEODSS main telescopes, with a nominal field of view of 2 degrees and sensitivity of 16th magnitude, and the GEODSS auxiliary telescope, with a nominal field of view of 6 degrees and sensitivity of 13th magnitude. Which of these telescopes to use is the first decision which must be addressed. The greater field of view of the auxiliary allows search of a greater volume of space, scaling by the linear increase rather than the area increase, since the objects pass across the field of view. The greater sensitivity of the main allows detection of fainter (smaller) objects, which should scale as the number of objects greater than the minimum size detectable. Preliminary analysis indicates that, if detection rate is the most important factor, the choice should be the GEODSS auxiliary telescope.[1] The best way to test this hypothesis is to observe in the same direction with both telescopes, simultaneously. However, since the GEODSS sites are required by contract with AF Space Command to always have two sensors on-line supporting their primary mission, AMOS has access to only one GEODSS sensor at the MSSS at any given time. AF Space Command could task a main and an auxiliary telescope to test this hypothesis, AMOS can not. The next best alternative is to view the same area of the sky, using a main telescope one night, the auxiliary telescope the next, then back to a main, and so on. This was attempted earlier this fiscal year, but was abandoned when AMOS was notified of a recent breakup. In an effort to detect objects due to this breakup, and because of the scan rates associated with this search, the main/auxiliary test was postponed. This will be attempted again later this fiscal year.

The second decision which must be addressed is the search mode to use. There are several types of searches which are used at the AMOS site. If the objects of the search are the resultant particles from a recent breakup, the search technique will be different than if the object of the search is the handoff of a recently discovered object from the ETS in New Mexico. Other object-oriented searches include follow-up searches for objects in the AMOS Analyst catalog (those objects which have been observed at the MSSS or ETS, but are not yet in the SSC catalog), or looking at objects which are expected to break up soon, based on historical data (e.g., SL-12 Proton fourth stages or Delta second stages). In addition, AMOS also performs zenith stares, where the search objective is not to detect any specific object.

The modes chosen for these searches fall into two broad categories: staring and scanning searches. The staring search, as the name implies, is simply pointing at a fixed position and waiting for an object to pass through the field of view. The scanning search is where the telescope mount follows a hypothesized debris orbit, and is primarily used to detect objects in the debris cloud resulting from a

[1]Lambert, J V, "Comparison of Expected with Observed Orbital Debris Detection Rates for the GEODSS Main and Auxiliary Telescopes," Draft paper, 1992

recent breakup. Although the staring search mode provides the best volume coverage for debris detection, the effective sensor sensitivity is reduced by the trailing of the image due to its relative motion across the field-of-view during an exposure. For the GEODSS auxiliary telescope, this motion results in a loss of detection sensitivity of 1.5 to 0.2 stellar magnitudes for objects in 300 to 1000 km orbits, respectively.[2]

The most common search mode is to use the auxiliary telescope in a staring search. GEODSS is tasked by AMOS for approximately 60 hours of observation per month, primarily during morning and evening twilight: terminator passes, at which time the objects are solar-illuminated but the sky background is dark. The video data from the ISIT camera is recorded on 3/4 inch tape for additional processing and analysis.

Correlation of objects with the SSC catalog is performed in real time using the RPS code WorldView. The Prototype AMOS Computer Control System (PACCS) is a system developed jointly by the Phillips Laboratory and RPS which can control all of the AMOS and MOTIF mounts simultaneously. For the Orbital Debris Measurements Program, the PACCS operator views two screens: the video output of the GEODSS ISIT camera, and the output of the WorldView program. The WorldView program has access to a star catalog, as well as the entire SSC catalog. It projects on its screen the star field at which the GEODSS telescope is pointing, as well as those satellites expected to cross the GEODSS field of view. Since the SSC element set may be old, and the predicted appearance of the satellite may be off by several degrees and/or several seconds, the satellite appears on the WorldView screen as a "bead on a wire", with the "wire" appearing on screen for some time before and after the expected appearance of the satellite. The flow of events is shown in Figure 1. If the same object appears on both screens, the object being observed by GEODSS is already in the catalog, and is of no further interest. If an object appears on the WorldView screen, but is not seen by GEODSS, that object is flagged for further study (comparison of objects seen by radar or optical sensors, but not both, discussed later in this paper). If an object appears on the GEODSS screen but not WorldView, it is likely a new object, and is therefore handed off to a tracking sensor.

There are several sensors at the MSSS which are appropriate for tracking objects. The only sensor eliminated from consideration is the GEODSS sensor being used for detection. If this sensor were to be used, the detection of other objects would be precluded during the track of the first object. This is not desirable, so the operational mode is that GEODSS continues its detect mission while the track sensor takes on the tracking mission. Any of the sensors at MOTIF or AMOS would be acceptable. The sensor usually chosen is the one which is not being used by other missions at the time, in most cases, the Beam Director/Tracker (BD/T). Under some circumstances, however, it may be appropriate to use a sensor with greater sensitivity, with different instrumentation, or larger acquisition field of view. In any case, the system which controls these sensors is always PACCS, since this system has the greatest flexibility. Once PACCS is fully developed, there can be multiple mounts simultaneously dedicated to tracking

[2]Lambert, J.V, Africano, J L, Kissell, K E, "Results of Orbital Debris Measurements Using AMOS and GEODSS Sensors," Proceedings of the 1992 MIT/LL Space Surveillance Workshop

debris objects.

Once the track of the object deteriorates, due to slant range, illumination, cloud cover, etc., the PACCS operator returns his attention to the GEODSS screen, and the detection process begins again, searching for the next uncorrelated object which passes through the GEODSS field of view. During this entire time, GEODSS has been maintaining its search profile, with its output video signal being recorded for post-processing.

It is often of interest to determine albedos of objects, and eventually sizes of objects, independent of radar measurements. This is accomplished using a radiometric analysis of simultaneous visible and longwave infrared measurements with MSSS instrumentation. The technique used is similar to that used by astronomers to determine the albedos and sizes of asteroids. The basic theory is that while a large, dark object may be visually as bright as a small, highly-reflective object, it will be hotter, hence brighter, in the thermal infrared. For this reason, AMOS periodically looks at debris objects in both the visible and the infrared.

The primary data used in the post-processing phase of operations is GEODSS video data which has been previously recorded on 3/4 inch tape. These tapes are transferred daily from the observatory at the top of Mt. Haleakala to the Kihei facility, and processed under more benign conditions.

Processing consists of detection of targets moving against the background star field, recording the object entry and exit times and positions, and determining brightnesses based on comparison to calibrated stars. The positions are converted to apparent right ascension and declination and reported to Air Force Space Command for correlation with the catalog of known satellites for that date. The observations are also processed to obtain initial estimates of object orbital height and inclination using a circular-orbit approximation.

Detection originally was accomplished using human operators (Air Force or Rockwell personnel) to view the videotapes, and log all events for later processing. Much of this time-consuming process has been automated, and the human operator plays a much smaller role. Because of the large amounts of data which must be processed, it is desirable to process the data at video frame rates. Otherwise, the overall process would take much longer than the time available, and the data would begin to backlog. AMOS has chosen to use the Datacube MaxTower system to perform the analysis. (Coincidentally, this is the same platform which the ETS has chosen, which allows unexpected synergism.) Although AMOS is continuing to examine alternative algorithms, the current technique uses the equivalent of background subtraction and creation of "super frames." A fuzzy mask of the background star field is generated, and then successive frames are added together, using this fuzzy mask. "Super frames" comprised of several seconds worth of data are then generated, and the human operator is able to view a processed "tape" which is approximately four minutes long, compared to the original tape which is approximately one hour long. This pass comprises the detection phase.

In addition to the correlation which takes place in real time, correlation also takes place in the video processing phase. Every object detected during processing of the videotape is correlated with the SSC catalog, as well as the local AMOS Analyst catalog. Because of the very short time for which an object is visible as it crosses the GEODSS field of view, it is not possible to obtain a very good element set for the object. Nevertheless, it is possible to screen the objects in the SSC catalog to determine possible correlations, based on time of observation, inclination, and altitude. This correlation process uses a series of filters, ranging from coarse to fine, until final correlation is achieved. If the object is not correlated, it is assigned a new AMOS identification number and inserted into the AMOS Analyst catalog. If the object is correlated with an object in the SSC catalog, it is ignored and the next object is analyzed. If the object is correlated with an object in the AMOS Analyst catalog, this observation is used in conjunction with previous observations to generate a better element set, which may be used to either detect the object on its next pass, or to hand it off to another site, such as the ETS.

The main thrust of these operating procedures is to keep track of those objects which are not in the SSC catalog, attempt to understand why they are not in the SSC catalog, and to provide Space Command with enough information and sightings to ensure their addition to the catalog.

Table 2 is a summary of detection and analysis statistics covering the first few months of this fiscal year. Meteor numbers are included as a statistic of interest, without drawing conclusions on the meaning. Because meteor detection rates are dependent on the time of the year as well as time of the night of observations (e.g., more meteors will be seen in mid-August in the early morning hours than several weeks later during early evening hours), additional analysis needs to be performed on this data to draw meaningful conclusions. Nevertheless, the data exists as a by-product of the debris search program.

DETECTION STATISTICS	
Hours observed:	98
Debris objects detected:	474
Meteors detected:	444

Table 2

The most intensively processed data to date resulted from a multi-site debris observing campaign organized by Air Force Space Command in August 1992. The Air Force PARCS Radar in South Dakota operated at increased sensitivity for a seventy-two hour period, with three optical sites (the Maui and Diego Garcia GEODSS facilities and the MIT/LL facility near Socorro NM) observing at every

available twilight surrounding this period. Fourteen hours of Maui GEODSS auxiliary telescope observations were obtained for eight twilight periods over a six-day interval. Seventy-six objects were detected with observed brightnesses ranging from 0 to 11th stellar magnitudes. Of these detections, forty-six objects (sixty-one percent) correlated very closely with cataloged satellites, with an additional two objects correlating at lower levels of confidence. Thus, approximately thirty-seven percent of the detections did not correlate. The brightest of these uncorrelated targets has an optical cross-section of 10 square meters (assuming a specular sphere) or an effective diameter of 3.5-meters. Space Command is continuing to analyze the results of the observing campaign and will be attempting to correlate detections between sites as well as with the catalog.

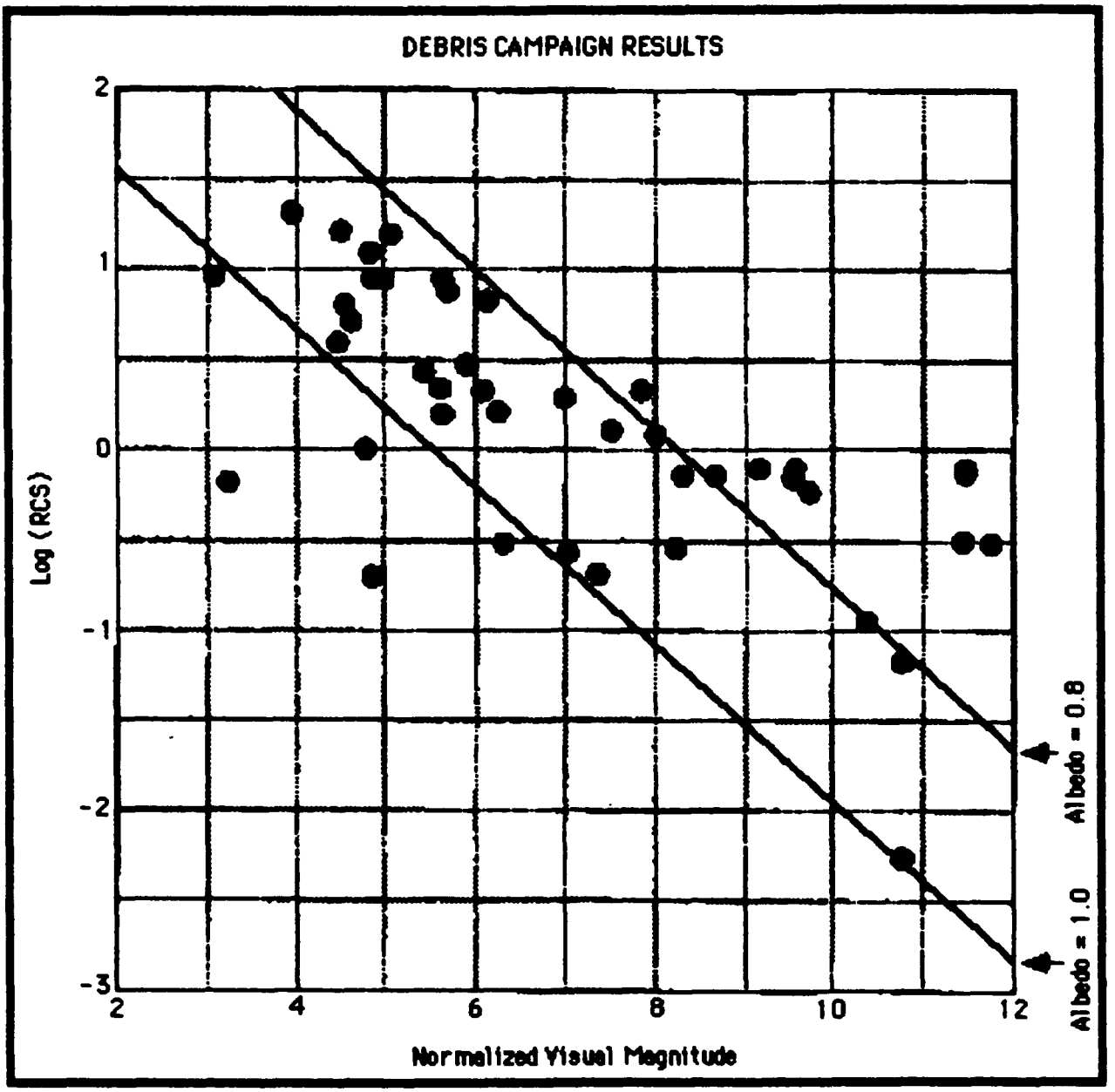

Figure 2

In Figure 2, radar cross section (RCS) is plotted against normalized visual magnitude (NVM) for those objects observed during the coordinated debris campaign which were also in the catalog. NVM is the magnitude of the object if it were at a slant range of 1000 km. Superimposed on this figure is a plot of RCS versus NVM for specular spheres of albedo 0.08 and 1.0. Within the constraints of this model, the line representing 1.0 albedo is a relatively conservative estimate of minimum object size. Using this line as a basis for size estimation of the uncorrelated objects from that same campaign, Figure 3 shows their apparent size as a function of altitude. Note that some of these objects, which do not correlate with anything in the SSC catalog, are quite large. It is apparent from this data that radar sites and optical sites are sensitive to different subsets of the entire orbiting population. There are some objects which are very bright visually, but which apparently have very small radar cross section. This is a subject of active interest, and is a high priority within the Air Force Debris Measurement Program. AMOS is in the process of establishing a database within the AMOS Analyst catalog that monitors those objects which are not seen by radar, but consistently seen by optical sites, as well as those objects which are routinely seen by radar, but rarely seen by optical sites.

The results from two observing campaigns are presented. the first campaign, may 1991, concentrated on finding objects associated with the breakup of the upper stage of a Delta rocket body. Results are also presented from the multi-site debris observing campaign organized by the air force space command in the fall of 1992.

Over a five night period within one week of a Delta rocket body breakup, approximately five hours of GEODSS data were obtained. The original rocket body had an inclination of 99.4 degrees with apogee and perigee at 1096 and 1028 km respectively. Figure 4 illustrates the altitude versus inclination distribution for all uncorrelated objects (or uncorrelated targets, UCTs) with an altitude less than 2,000 km. It is immediately obvious that the majority of these UCTs are probably associated with the original rocket body. It can also be seen that many of the other UCTs tend to cluster in the 60 to 80 degree inclination bands. These inclination bands correspond to Soviet satellite constellations. In particular, the 63 degree inclination band is used by Soviet Molniya and early warning satellites. Figure 5 presents the altitude versus inclination distribution for all UCTs having an altitude less than 20,000 km. Note the four UCTs having inclinations between 60 and 70 degrees and altitudes greater than 10,000 km. These may be uncatalogued Molniya-type objects, easily seen optically at ranges far beyond current radar capabilities.

For the multi-site debris observing campaign, fourteen hours of observations obtained over six nights are presented. Zenith stare observations were performed trying to determine relation between optical and radar observations. Figure 6 presents the altitude/inclination distribution for the UCTs having altitudes less than 20,000 km. Notice that about half of the objects are in the 90 to 110 degree inclination band, plus the Molniya-type object at 14,000 km at an inclination of about 63 degrees. Again, there is some evidence of clustering of UCTs in the 60 to 80 degree inclination bands.

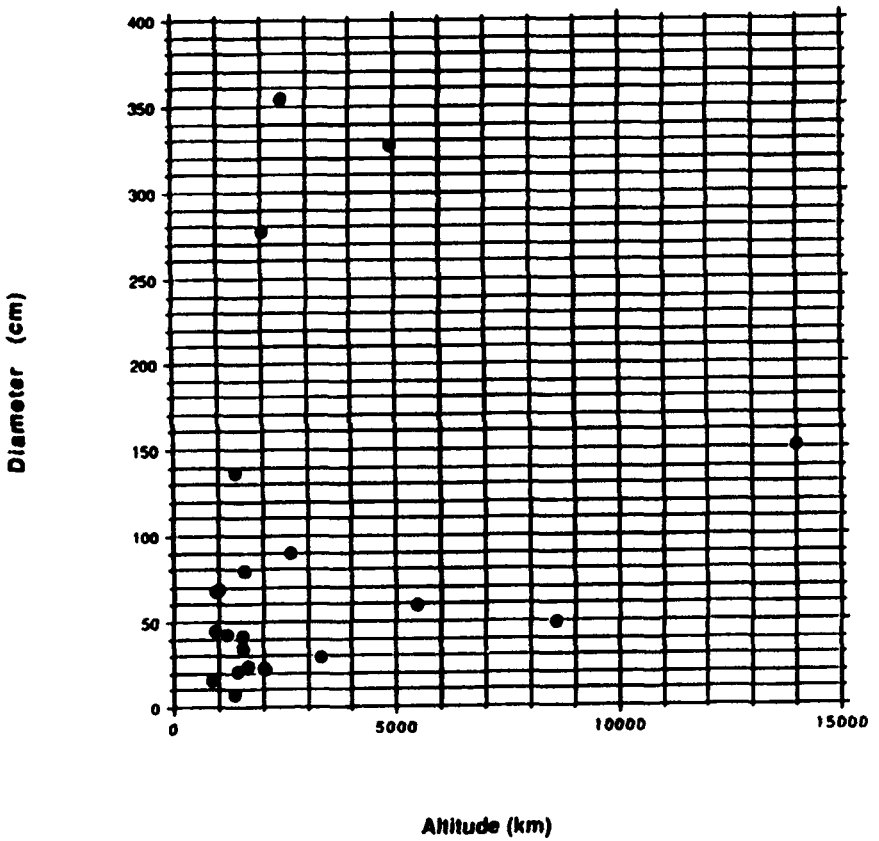

Figure 3

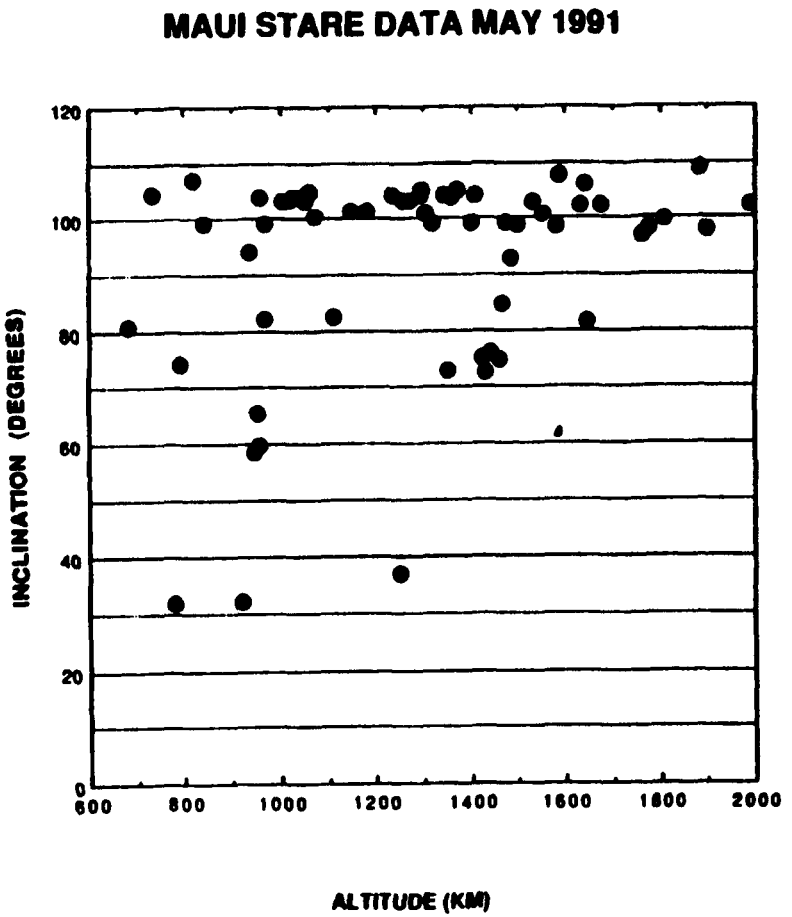

Figure 4

MAUI STARE DATA MAY 1991

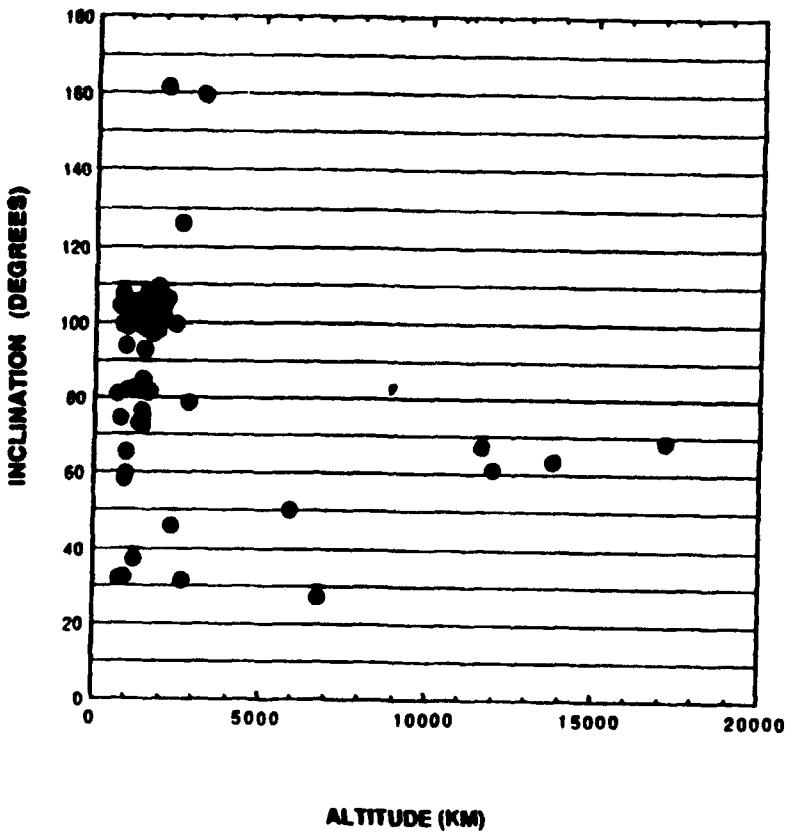

Figure 5

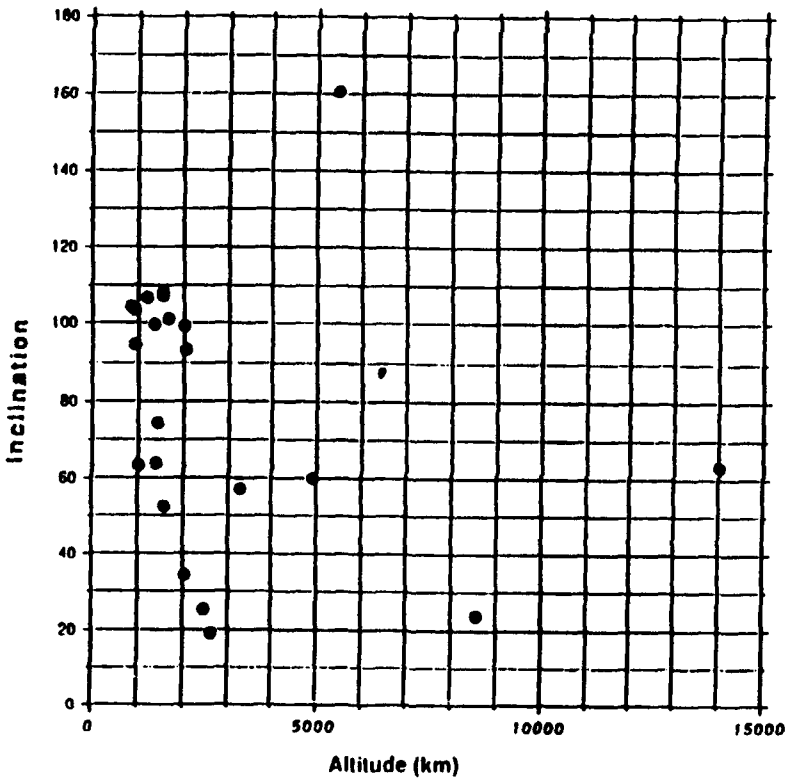

Figure 6

In conclusion, it appears that the optical sensors may be sampling a different debris environment than the radar sensors used to maintain the catalog. Some objects which have a large RCS have a low optical brightness, while some objects with small RCS have quite large brightness. Some of the debris objects we have seen that are not in the SSC catalog are quite large, possible meters in size. A database is being constructed of objects which radar sites see but optical sites do not, and vice versa. It is expected that as this database grows, our understanding of the properties of these objects will grow as well. Several hypotheses involving debris material and orbital properties are being investigated, including the possible materials and structures which would lead to these apparent disparities, and the orbits which are more often represented in each catalog.

CONCEPTUAL DESIGN OF A SENSOR NETWORK FOR COLLISION AVOIDANCE

Eugene G. Stansbery (NASA/Johnson Space Center)

INTRODUCTION

Currently the Space Station Freedom's (SSF) plan to deal with orbital debris calls for shielding against sizes up to 0.86-cm diameter and performing collision avoidance maneuvers against those objects tracked by the Space Surveillance Network (SSN). This leaves a gap in sizes to which the SSF is vulnerable, although the probabilities of collision are low. The NASA Administrator has requested that the feasibility of eliminating this gap be studied. Two teams were formed, a shielding team and a collision avoidance team. This paper will discuss the results of the feasibility study for a sensor network to provide collision avoidance between the SSF and debris down to 1-cm in diameter.

LIMITATIONS OF THE CURRENT SPACE SURVEILLANCE NETWORK

For randomly shaped debris objects, an adequate radar cross section (RCS) vs. physical size representation can be formed by using the Rayleigh scattering approximation up to its intersection with the optical approximation and following the optical approximation to large sizes. Figure 1 shows this representation for a number of standard radar frequencies. This figure illustrates the problem in attempting to use long wavelength radars to detect small objects. For example, the current FPS-85 radar at Eglin AFB operates at UHF band (~440 MHz/70-cm) and currently detects and tracks objects as small as about 10-cm diameter. The FPS-85 sees a 10-cm object as having an RCS of about -25 dBsm. It would see a 1-cm object as having an RCS of about -85 dBsm. It would take a 60 dB increase in sensitivity for Eglin to detect and track a 1-cm object with the same probability of detection and probability of false alarms. The majority of ground based radars that are currently operating in the Space Surveillance Network (SSN) are UHF radars with wavelengths near 70-cm. Those few radars which can currently detect 1-cm or which could possibly be upgraded to reach 1-cm are all located at high latitudes and could not detect objects in low earth orbits (LEO) with low or medium inclinations. For these reasons, upgrading the current SSN radars for the SSF collision avoidance task is not reasonable. New sensors are needed.

NETWORK TASKS

The tasks that a new collision avoidance network must perform are very similar to those tasks currently performed by the SSN to provide collision avoidance for the Space Shuttle. Figure 2 shows the various tasks that a SSF collision avoidance network must be able to accomplish. It first must be able to generate a catalog of all of the objects of interest. To generate a catalog, uncataloged objects must be initially detected. To accomplish this, a search volume must be established. The time needed to complete a catalog will be inversely proportional to the search volume. Therefore, it is desirable to have a large search volume. Once an object is detected, the network must be able to predict the orbit far enough ahead to be able to correlate an

observation with the object at the next track opportunity. Once several observations have been made, the orbital elements can be estimated accurately enough to maintain the object in the catalog.

In order to maintain a catalog, the object's orbital elements must be accurate enough to be able to correlate an observation with its respective object (and, conversely, to be able to identify new, uncataloged objects). Given the density of objects as small as 1-cm diameter in LEO, it is estimated that each element set must be updated on the order of once per day. Additional catalog maintenance tasks would include accurately estimating the size of an object by combining multiple observations and developing and maintaining the object's drag history.

Once an object is cataloged, its orbit must be predicted ahead to look for possible conjunction of its orbital position with the Space Station's predicted position. When a possible conjunction is identified, that object would then be intensively tracked in order to reduce the uncertainty in its position to a point where it is no longer a threat to the Space Station, or until it is determined that a maneuver by the Space Station is required.

CONJUNCTION UPDATE REQUIREMENTS

The process used to define the conjunction update requirements is shown in block diagram form in Figure 3. The Position Accuracy Requirements is the upper left hand block essentially defines the metric uncertainty of a debris object's position at the time of a predicted conjunction. The object's position uncertainty will be larger along the orbit (in-track) than orthogonal to the orbit (cross-track) thereby forming an ellipsoidal uncertainty volume. A conjunction is defined as the predicted intersection of the SSF's position uncertainty volume with the position uncertainty volume of a debris object or other satellite. The Position Accuracy Requirements are a function of the SSF's requirements (size, altitude, and number of allowed maneuvers) and the debris environment (the debris flux crossing the Space Station's orbit). The SSF's will fly a constant drag profile. This means that at times of low solar activity (i.e. low atmospheric drag) the altitude may drop as low as 325 KM while during times of high solar activity (high drag) the altitude may be as high as 500 km. The nominal design altitude is 400 KM. The conceptual collision avoidance network should track all objects that pass through this volume plus any objects that are about to enter the volume. Therefore, the altitude limits for maintaining the catalog is from 300-600 KM altitude.

One of the desires of the SSF is to provide experimenters with between four and six 30-day microgravity periods per year. In order to achieve this with a reasonable probability, the SSF would be limited to 10 or fewer collision avoidance maneuvers per year.

There are currently about 1120 satellites and debris objects passing through or resident in the 300-600 KM altitude region that are in the SSN catalog. NASA's measurement of the small debris environment using the Haystack radar indicate that there are about 20 times as many objects 1-cm and larger as there are SSN cataloged objects. Therefore, it is a reasonable estimate that there are about 25,000 objects 1-cm and larger that pass through the altitude band of interest. Of these objects, about 90% are in highly elliptical orbits. Since these orbits spend very little time in the 300-600 KM altitude

band, they actually represent only about 10% of the total collision probability. The other 3000 objects that are in near circular orbits represent 90% of the collision probability. Therefore, it is more critical to assure that all of the near circular objects are cataloged than it is to catalog all of the highly elliptical orbits.

The number of objects combined with the desired maneuver rate for SSF lead to the requirement that the position of the debris object at the predicted conjunction be known to within 80 M cross-track and 400 M in-track.

In the upper right hand block of Figure 3 is Position Accuracy Capability. In general, the Position Accuracy Capability depends on how accurately the position can be measured at the time of the measurement and on how rapidly the uncertainty grows over time after the measurement. The uncertainty in position at the time of measurement is a function of the metric accuracy of the sensor. However, a single track by a single radar is probably not sufficiently accurate to meet the 80x400x80 meter requirement. A more accurate estimate may be drawn by fitting the measurements from several different measurements from different parts of the orbit. It is estimated that using several tracks the likely achievable position accuracy is 1-2 meters in slant range from the radar and 30-50 meters in cross range. However, this uncertainty grows rapidly with time due in part to uncertainties introduced by the propagator used to predict the future position of the object and to uncertainties in drag caused by incomplete knowledge of the earth's thermosphere. Analytical propagators such as the programs PPT2 (used at NAVSPASUR) and SGP4 (used by USSPACECOM) have an inherent accuracy limit of about 1 KM. As this is larger than the position accuracy requirement, it will be necessary to use a special perturbations routine for collision avoidance. Perhaps the largest contributor to the position uncertainty is that caused by incomplete knowledge of the thermosphere. It has been suggested that since the SSF is flying through the same medium, its own orbit can be used to provide a better estimate of drag. Similarly, there will be 3000 small objects in low altitude, near circular orbits which will be tracked and which can be used to estimate drag. However, it is estimated that using current techniques, the 80x400x80 meter uncertainty requirement will be reached after about 2 orbits for small debris.

The Position Accuracy Requirements and the Position Accuracy Capability, therefore have indicated that ground based sensors should be placed such that a debris object in near circular orbit can not go more than two orbits without its position being updated by one of the sensors.

SENSORS

The following have been considered as possible radars to be included in a collision avoidance network.

The Ground Based Radar (GBR) is currently being developed for the Strategic Defense Initiative Organization (SDIO). The GBR-T radar is in the design phase and the is slated to be built at Kwajalein. Once the test program is completed at Kwajalein, the radar will become a range asset. Both the 3-cm wavelength and the low latitude location (8.7°) are appropriate for the collision avoidance network. The GBR-T will be a phased array radar on a mechanically steered mount. It is capable of time shared operations such as

simultaneous multiple tracks or tracking an object while maintaining a search volume. However, the search volume capability of GBR-T is limited and is not considered sufficient to meet all of the networks requirements.

The NAVSPASUR interferometer has a very large search volume ideal for initial detection and element set maintenance. Most unplanned breakups are reported by NAVSPASUR first. Unfortunately, the current NAVSPASUR system operates in the Very High Frequency (VHF) band near 217 MHz with about a 140-cm wavelength. A new design could be built for debris at either C-band or X-band using the interferometer concept proven by the current NAVSPASUR. We will designate this concept as the Debris Interferometer Fence Radar (DIFR). If the fence was built in the east-west direction and covered at least 22° in longitude, then each object in LEO would pass through the fence twice per day.

The Have Stare radar is another X-band design and is currently under construction at Vandenberg AFB in California. The Have Stare design has a mechanically steered dish. Being a simpler and less expensive radar than the GBR-T, multiple copies of the Have Stare could be built to provide the necessary coverage for conjunction updates.

NASA is also considering an on-board sensor to supplement a ground based network. The on-board sensor configuration has not yet been determined, but radar, passive optical, and LIDAR sensors are being evaluated. The sensor would have to be directed onto an object by the ground network because of power and other limitations involoved with flying on the Space Station. However, an on-board sensor would have very high metric accuracies and could be used to refine orbit estimates from the ground network. It could also supplement the network when one of the ground based radars was not operational because of maintenance or other reasons.

EXAMPLE SENSOR NETWORK

One possible arrangement of sensors is shown in Figure 4. This figure shows the area at 400 KM altitude covered by each sensor assuming a 10° minimum elevation. The site locations are:

DIFR	Co-located with NAVSPASUR.
GBR-T	Kwajalein Atoll
Have Stare	South Point, Hawaii
Have Stare	Vandenberg AFS, California
Have Stare	Kennedy Space Center, Florida
Have Stare	Kourou, French Guiana.

Co-locating DIFR with NAVSPASUR limits the orbits that it can detect to those with inclinations greater than about 33°. However, if the distribution of inclinations of 1-cm and larger debris follows the distribution of the current SSN catalog, then DIFR will see the large majority of the objects. The search capability of DIFR would be supplemented by the GBR-T radar at Kwajalein with a search volume optimized for low inclination orbits. Being a phased array radar, the GBR-T would be able to maintain this search volume and still be able to contribute tracks fot conjunction updates. The other sites would use the less expensive Have Stare radars to ensure the capability ot observe LEO orbits at least once every two orbits.

Although not an ideal network, this configuration has certain advantages. The majority of the sensors are located on United States soil. The only exceptions are the GBR-T in Kwajalein where the U.S. has had a major radar facility for many years and a Have Stare located in French Guiana. France, however, is a partner in the Space Station. This could mean special status for this site not involving transfer of funds.

CONCLUSIONS

NASA has completed a conceptual study which has determined that it is feasible to construct a network of ground based radars which can catalog LEO objects as small as 1-cm. in diameter for the purpose of collision avoidance by the Space Station or other high value LEO spacecraft. Obviously, further study is needed which will include potential uses of this type of network by other organizations such as the Department of Defense.

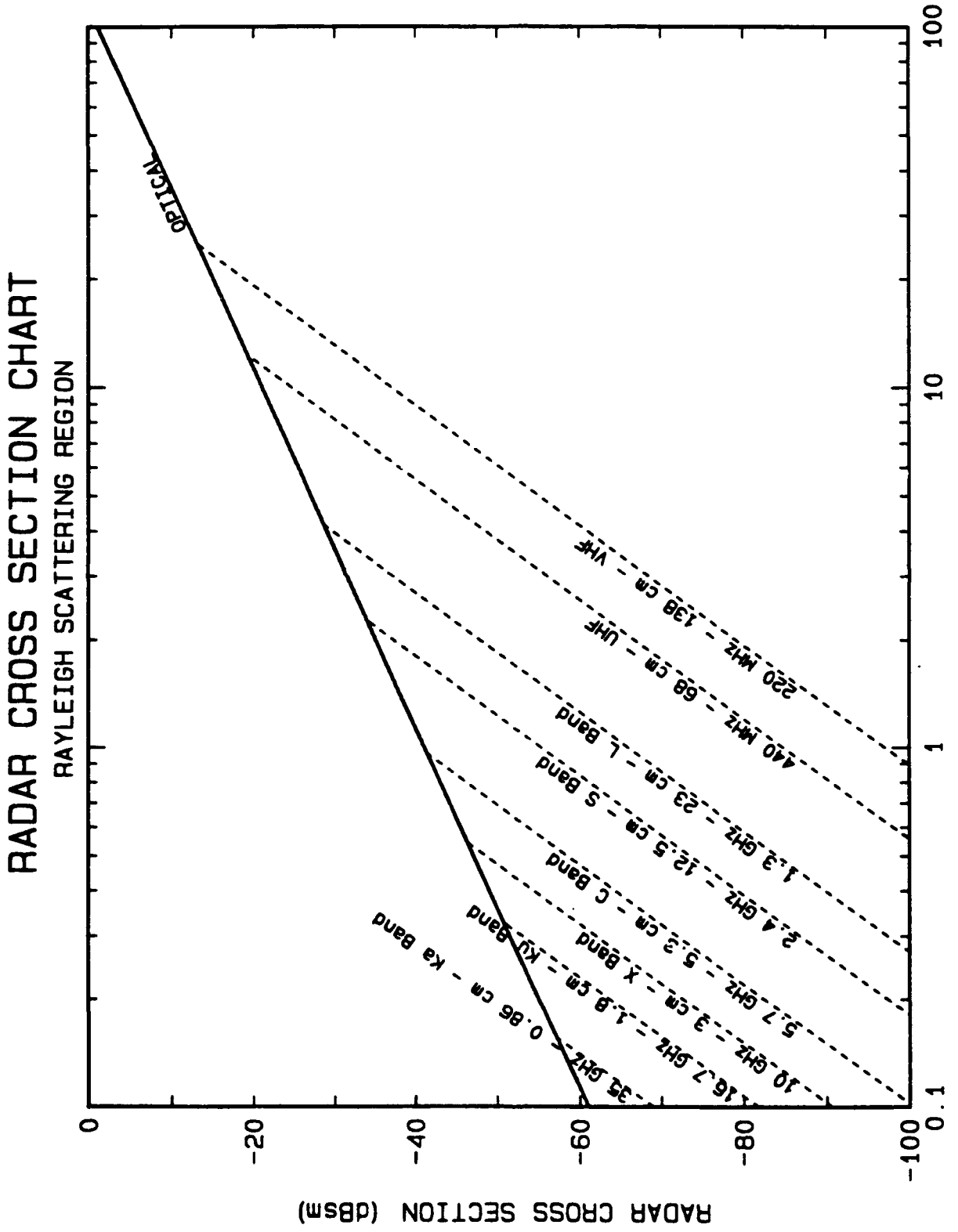

Figure 1. Plot showing the Rayleigh scattering curves for various radar bands.

NETWORK TASKS

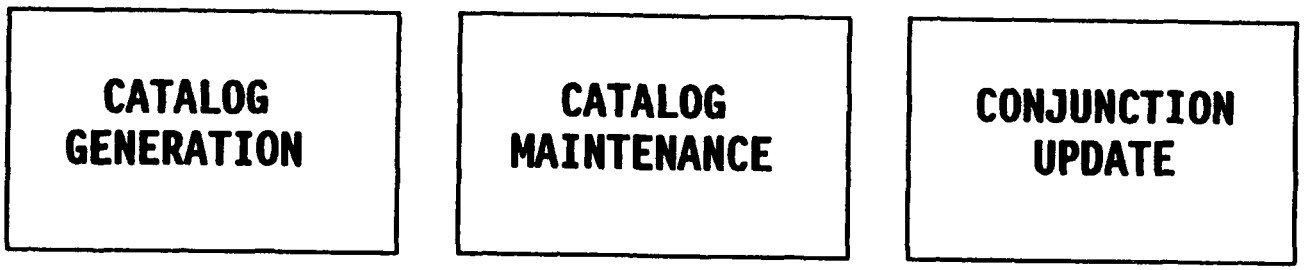

- INITIAL DETECTION
- CORRELATION
- INITIAL ORBIT DETERMINATION

- ELEMENT SET MAINTENANCE
- SIZE ESTIMATION
- DRAG HISTORY

- LOCATION UNCERTAINTY REDUCTION

Figure 2. Network tasks.

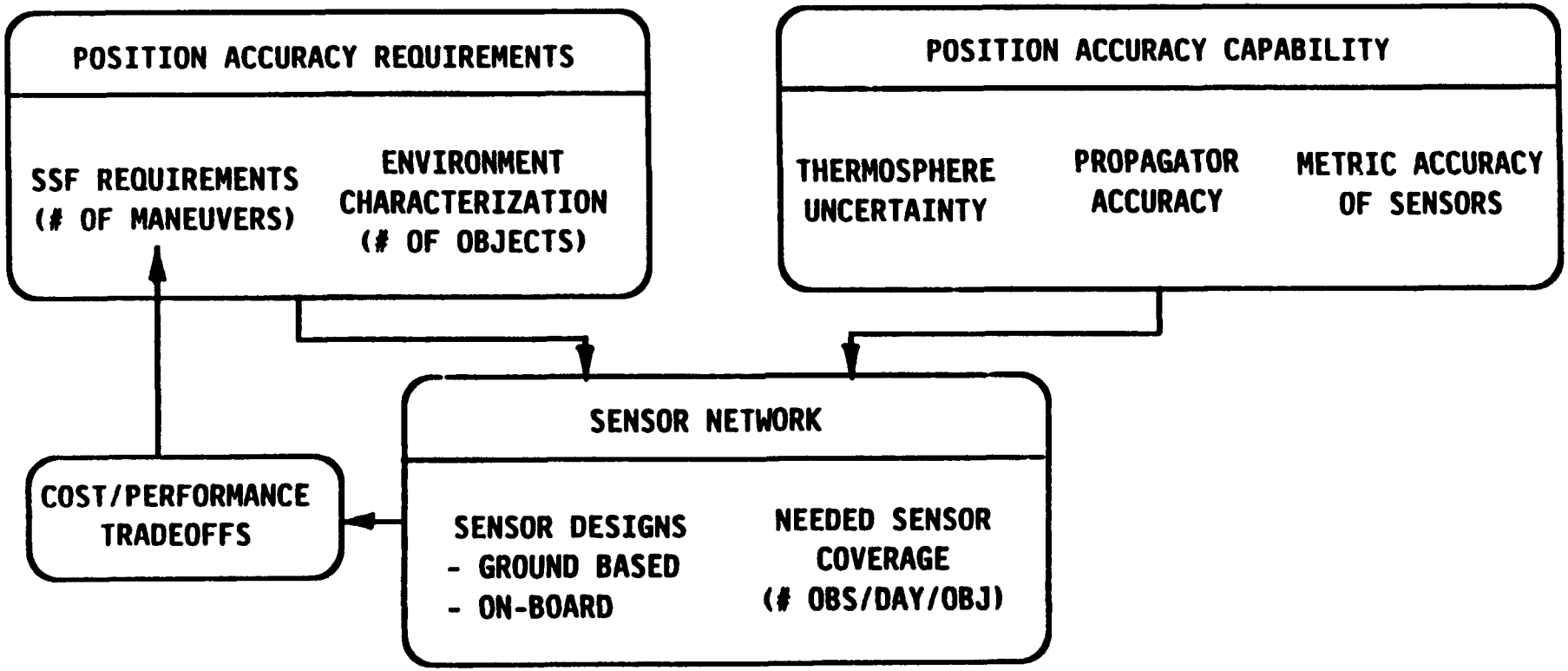

Figure 3. Block diagram developing the requirements on the network for conjunction updates.

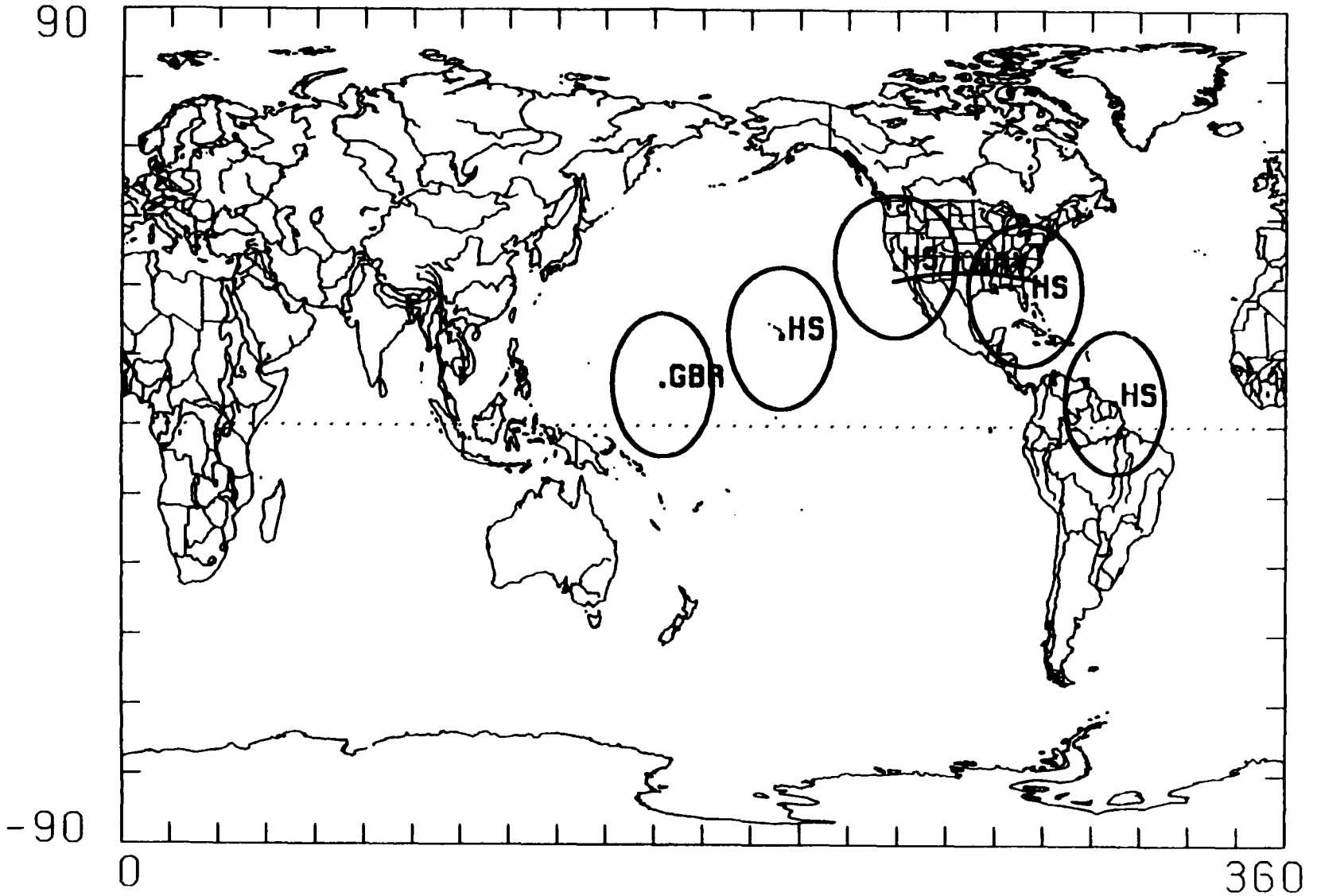

Figure 4. Example network.

REPORT DOCUMENTATION PAGE

Form Approved
OMB No. 0704-0188

1. AGENCY USE ONLY (*Leave blank*)	2. REPORT DATE	3. REPORT TYPE AND DATES COVERED
	1 April 1993	Project Report

4. TITLE AND SUBTITLE

Proceedings of the 1993 Space Surveillance Workshop

5. FUNDING NUMBERS

C — F19628-90-C-0002

6. AUTHOR(S)

R.W. Miller and R. Sridharan (Editors)

7. PERFORMING ORGANIZATION NAME(S) AND ADDRESS(ES)

Lincoln Laboratory, MIT
P.O. Box 73
Lexington, MA 02173-9108

8. PERFORMING ORGANIZATION REPORT NUMBER

STK-206 Volume II

9. SPONSORING/MONITORING AGENCY NAME(S) AND ADDRESS(ES)

ESC
Hanscom Air Force Base
Bedford, MA 01730

10. SPONSORING/MONITORING AGENCY REPORT NUMBER

ESC-TR-93-249

11. SUPPLEMENTARY NOTES

None

12a. DISTRIBUTION/AVAILABILITY STATEMENT

Approved for public release; distribution is unlimited.

12b. DISTRIBUTION CODE

13. ABSTRACT (*Maximum 200 words*)

The eleventh Annual Space Surveillance Workshop hosted by MIT Lincoln Laboratory was held 30–31 March and 1 April 1993. The purpose of this series of workshops is to provide a forum for the presentation and discussion of space surveillance issues.

This *Proceedings* documents most of the presentations from this workshop. The papers contained were reproduced directly from copies supplied by their authors (with minor mechanical changes where necessary). It is hoped that this publication will enhance the utility of the workshop.

14. SUBJECT TERMS	15. NUMBER OF PAGES
	138
	16. PRICE CODE

17. SECURITY CLASSIFICATION OF REPORT	18. SECURITY CLASSIFICATION OF THIS PAGE	19. SECURITY CLASSIFICATION OF ABSTRACT	20. LIMITATION OF ABSTRACT
Unclassified	Unclassified	Unclassified	Same as report